Le côté obscur de la relativité générale

Jean-Francois Coupechoux

N°d'ordre NNT : 2021LYSE1153

THÈSE de DOCTORAT DE L'UNIVERSITÉ DE LYON
opérée au sein de
l'Université Claude Bernard Lyon 1

École Doctorale ED52
de Physique et d'Astrophysique

Spécialité de doctorat : Physique Théorique
Discipline : Astroparticules & Cosmologie

Soutenue publiquement le 10/09/2021, par :
Jean-François Coupechoux

The Dark Side of General Relativity

Devant le jury composé de :

TSIMPIS Dimitrios, Professeur des Universités, Université Lyon 1, IP2I	Président
NOVAK Jérôme, Directeur de recherche CNRS, LUTH, Meudon	Rapporteur
RIOTTO Antonio, Professeur, Université de Genève, CAP	Rapporteur
CAPRINI Chiara, Directrice de recherche CNRS, APC, Paris	Examinatrice
MOHAYAEE Roya, Chargée de recherche CNRS, IAP, Paris	Examinatrice

ARBEY Alexandre, Maître de conférences, Université Lyon 1, IP2I Directeur de thèse

Résumé

Motivés par les récentes détections d'ondes gravitationnelles, nous considérons que les trous noirs primordiaux sont une alternative valable à une partie significative de la matière noire. Pour le moment, il n'y a pas de preuves expérimentales de l'existence d'un tel objet mais l'évènement appelé GW190814 a permis de détecter un objet compact de 2.6 $M_\odot$. Il s'agit donc soit de l'étoile à neutrons la plus massive, soit du trou noir le plus léger jamais détecté. Mais il pourrait également s'agir d'un trou noir primordial et nous allons considérer différents aspects des ondes gravitationnelles reliées aux trous noirs primordiaux. Tout d'abord, nous avons utilisé le code développé par la communauté d'Einstein Toolkit pour résoudre numériquement les équations d'Einstein et calculer des formes d'ondes gravitationnelles émises par la fusion de deux trous noirs. Ces formes d'ondes sont valables pour n'importe quelle masse du système considéré grâce aux relations de scaling pour des trous noirs décrits par la métrique de Kerr. On peut donc facilement avoir la forme d'onde pour des trous noirs allant d'une masse de l'ordre du gramme jusqu'à des millions de masses solaires. Ces relations de scaling sont également valables pour des trous noirs chargés mais il existe des trous noirs plus exotiques qui brisent les relations de rescaling. Nous étudierons les limites physiques de ces relations en considérant l'expansion de l'Univers et le rayonnement de Hawking qui peuvent devenir non négligeables pour des trous noirs primordiaux.

Lorsqu'un signal d'onde gravitationnelle est détecté par la collaboration LIGO/Virgo, les objets détectés sont classés en étoiles à neutrons si leur masse est inférieure à 2.2 $M_\odot$ et en trous noirs si leur masse est supérieure à 5 $M_\odot$. Mais si on ne veut pas utiliser cette distinction, il faut être capable de mesurer l'effet de la matière baryonique décrivant une étoile à neutrons grâce à la déformabilité de marée. Ainsi, nous étudierons les conditions nécessaires pour déterminer la nature des objets compacts en injectant des formes d'onde dans un bruit réaliste des détecteurs.

Par ailleurs, il existe de nombreux candidats pour décrire la matière noire et les trous noirs primordiaux n'en constituent qu'un parmi tant d'autres. Le modèle Fuzzy Dark Matter basé sur un champ scalaire en est un autre, et il est possible d'étendre un tel modèle pour qu'il imite également le comportement de l'énergie noire. Nous étudierons son potentiel pour en donner la forme la plus générale. A basse énergie, les deux ingrédients de base sont : un terme de masse de l'ordre de 10^{-22} eV et une constante V_0 dominant l'évolution

récente de l'Univers pour remplacer l'énergie noire. Cependant, la forme du potentiel reste une question ouverte car elle est très peu contrainte au cours de l'histoire de l'Univers. En revanche, il est possible de donner des limites sur la densité d'énergie d'un champ scalaire totalement générique au moment de la nucléosynthèse primordiale grâce à l'abondance des différents éléments primordiaux. Ces limites sont données pour un champ scalaire stable et pour un champ scalaire se désintégrant en radiation. Il existe de nombreux modèles utilisant des champs scalaires en cosmologie, pour essayer de réduire leur nombre, une solution est de les considérer comme non indépendant. Pour cela, nous introduirons un modèle de triple unification unifiant : l'inflation, la matière noire et l'énergie noire avec un seul et unique champ scalaire couplé de manière non minimale à la gravité.

Keywords: Matière noire, énergie noire, champs scalaires en cosmologie, nucléosynthèse primordiale, trous noirs primordiaux, étoiles à neutrons, ondes gravitationnelles.

Abstract

Motivated by the recent gravitational wave detections, we consider primordial black holes as a valid alternative to a significant fraction of dark matter. At the moment, there is no experimental evidence of such an object, but the event called GW190814 has detected a compact object of 2.6 $M_\odot$. It is therefore either the most massive neutron star or the lightest black hole ever detected. But it could also be a primordial black hole and we will consider different aspects of gravitational waves related to primordial black holes. First, we used the code developed by the Einstein Toolkit community to solve numerically the Einstein equations and calculate the gravitational wave-forms emitted by a binary black hole merger. These wave-forms are valid for any mass of the system thanks to the scaling relations for black holes described by the Kerr metric. We can thus easily have the wave-form for black holes having a mass of the order of a gram up to millions of solar masses. These scaling relations are also valid for charged black holes but there are more exotic black holes that break the scaling relations. We will also study the physical limits of these relations by considering the expansion of the Universe and Hawking radiation, which can become non-negligible for primordial black holes.

When a gravitational wave signal is detected by the LIGO/Virgo collaboration, the detected objects are classified as neutron stars if their mass is lower than 2.2 $M_\odot$ and as black holes if their mass is higher than 5 $M_\odot$. But if we do not want to use this distinction, we must be able to distinguish the effect of baryonic matter describing a neutron star through the tidal deformability. We will study the necessary conditions to determine the nature of compact objects by injecting wave-forms into a realistic detector noise.

There are many candidates to describe dark matter and primordial black holes are one of them. The Fuzzy Dark Matter model based on a scalar field is another one and it is possible to extend this model to also mimic the behavior of dark energy. We will study the potential of such a model to give the most general form. At low energy, the two basic ingredients are: a mass term of the order of 10^{-22} eV and a constant V_0 dominating the recent evolution of the Universe to replace dark energy. However, the shape of the potential remains an open issue because it is not very constrained in the primordial Universe. On the other hand, it is possible to give limits on the energy density of a generic scalar field during Big-Bang nucleosynthesis by the observed abundance of the elements. These limits

are given: for a stable scalar field and for a scalar field decaying into radiation. There are many models using scalar fields in cosmology, to reduce their number, a solution is to consider them as non-independent. For this, we will introduce a triple unification model unifying: inflation, dark matter and dark energy with a single scalar field with a non-minimal coupling to gravity.

Keywords: Dark matter, dark energy, cosmological scalar fields, Big-Bang nucleosynthesis, primordial black holes, neutron stars, gravitational waves

Acknowledgements

Tout d'abord, je tiens à remercier chaleureusement toute l'équipe du laboratoire de l'Institut de Physique des 2 Infinis de Lyon (IP2I) qui m'a accueilli pendant trois ans pour effectuer mon doctorat et en particulier le groupe Théorie. Un grand MERCI à mon directeur de thèse Alexandre Arbey pour sa gentillesse et les repas que l'on a pu partager ensemble. Il a toujours su être présent lors des moments importants de ma thèse. Je tiens également à remercier toutes les personnes du Journal Club "ondes gravitationnelles" et tous ceux avec qui j'ai pu travailler. En particulier merci à Jérôme pour m'avoir expliqué la physique nucléaire avec le méta-modèle, à Roberto et à Viola pour toutes leurs remarques très perspicaces, à Hubert pour tous les programmes que je t'ai fait installer sur le serveur et bien sûr merci à Rahul et à Guilherme.

Je tiens à remercier l'ensemble des membres du jury, qui m'ont fait l'honneur d'avoir accepté l'invitation et d'avoir pris le temps de juger ce travail. Merci pour vos questions constructives et vos remarques qui m'ont permis d'améliorer ce manuscrit. J'espère avoir la chance de vous revoir très vite à des conférences.

Mon doctorat en physique ne s'est pas uniquement résumé à faire de la physique. Une partie non négligeable de mon travail a consisté à programmer et à utiliser des codes. Je ne connais personne de plus compétente en C++ que mon collègue de bureau Grégoire. Il m'a expliqué un nombre incalculable de notions et m'a fait gagner beaucoup de temps en résolvant certains de mes problèmes en 5 minutes ;). Merci à lui et aussi au support du service informatique du laboratoire pour leur aide précieuse.

Une autre partie de mon travail a été l'enseignement à travers l'activité complémentaire d'enseignement. J'ai eu la chance d'enseigner le C/C++, l'électrostatique, la magnétostatique, l'optique, l'électricité et la radioactivité. J'ai beaucoup appris en enseignant et je tiens à remercier les responsables de ces unités d'enseignements pour leur gentillesse et leur organisation irréprochable.

Mon doctorat n'aurait vraiment pas eu la même saveur sans les autres doctorants qui sont devenus des amis. Merci à eux avec une dédicace particulière à mes co-bureaux Grégoire et Philippe pour l'ambiance générale : j'étais toujours heureux de me rendre au bureau. Je me souviendrai longtemps des parties de billard effectuées pendant les pauses et des sorties au bar. Nous avons eu la chance d'avoir un groupe de doctorants très soudé : un GRAND MERCI à eux !!!! Je ne peux pas tous vous citer mais merci aux M1 ;), à Antoine, Corentin, Lucas, Lysandra, Quentin ... Merci à mes partenaires de tennis (Léa & Florence & Émilie), de jogging (Amélie & Danaël & Will), de vélo (Léo & Shahram) et de musculation. Je suis certain d'avoir oublié quelqu'un dans cette liste mais je dois avoir tort.

Enfin, le doctorat est l'aboutissement de longues années d'études et je tiens à remercier tous ceux qui m'ont aidé dans ce but : ma famille, mes amis et mes professeurs; avec une dédicace particulière à ma sœur et à mes parents, qui m'ont toujours soutenu. J'ai sûrement oublié beaucoup de personnes : désolé et merci.

Contents

Introduction

Who, looking at the night sky filled with bright stars, is not amazed by the space and the size of the Universe? Throughout history, the notion of Universe has evolved according to philosophical principles. In ancient Greece, Aristotle considered the Earth as a fixed point at the center of everything (geocentric theory) and it was not until the Renaissance that Copernic' principle emerged with the idea that our planet is not the center of the Universe and that it should not have a privileged position. In the 17th century, thanks to Galileo's telescopes, the solar system could be observed with precision and in the 20th century, the questions of history, structure and evolution of the cosmos appeared with the concept of Big-Bang. The debate on the cosmological constant is a striking illustration of the evolution of knowledge in cosmology. Initially, Einstein had introduced it to impose a static Universe, which was challenged by Hubble's law and then removed. But, with the discovery of the accelerated expansion of the Universe, Einstein's constant was reintroduced with a different value.

Today, at the beginning of the 21st century, cosmology is opening a new period, sometimes called modern cosmology with a huge amount of data. To give some examples, the Center for Astrophysics recorded the position of 1100 galaxies in 1985 and now, with the Sloan Digital Sky Survey (SDSS) [1], the 3D position of four million galaxies and quasars is mapped which covers 90% of the visible Universe. In 1964, the cosmological background was discovered and only an approximation of its temperature was measured and today, the Planck collaboration measures its anisotropy with great precision and puts constraints on cosmological parameters [2].

Cosmology is a science distinct from others, because no experiment can be performed directly to test hypotheses without bias: no Universe can be created. With astronomical observations, a standard model called ΛCDM has emerged. This model is based on General Relativity and knowledge of fundamental physics to answer some of these questions: How did the elements form? How did galaxies form? Why is the Universe so flat? Why is the CMB so homogeneous even in non-causally connected regions? etc. According to the Big-Bang, the origin of the Universe dates back to 13.8 billion years ago. At that time, the Universe was hotter and denser. Its evolution described by the ΛCDM model, is based on four main observations: the abundance of elements predicted by the Big-Bang nucleosyn-

thesis, the expansion of the Universe by the Hubble diagram, the cosmological background and the large scale structure of the observable Universe with galaxy distribution.

Despite the great success of ΛCDM model, it introduces a cosmological constant Λ and cold dark matter whose natures are totally unknown and which constitute 95% of the total energy of the Universe. In other words, the Standard Model of particles can only describe 5% of the Universe. So, "What is dark matter?", "What is dark energy?". Remain the most important unresolved questions in cosmology. There are many theories that try to answer these questions. For cold dark matter, they can be classified into two groups. The first one considers that General Relativity must be modified and that the missing matter is only a gravitational effect and that no unknown cold dark matter is needed. Modified Newtonian dynamics (MOND) [3] is an example of such a theory. The second group considers that at galaxy scale, General Relativity is still valid and adds a new ingredient like weakly-interacting massive particles (WIMPs) to describe cold dark matter. But these particles have not yet been detected by direct experiment like Edelweiss [4] and no clue of new physics has been found in the Large Hadron Collider. It is also possible to mimic the behavior of cold dark matter with primordial black holes [5] or with ultra-light particles described by a scalar field [6]. Concerning the cosmological constant Λ, it has been introduced to take into account the acceleration of the expansion of the universe observed using supernovae of type Ia [7]. In the equations of General Relativity, the cosmological constant can appear on the left side of the equation as a space-time curvature term through the $\Lambda g_{\mu\nu}$ term or in the right side as a source term interpreted by a fluid with negative pressure called dark energy. What is strange is that throughout the evolution of the Universe, because of its, the cosmological constant only starts having an impact today. An accelerated universe expansion can also be easily described by a scalar field dominated by it potential as is the case for inflation.

Scalar fields are ubiquitous in cosmology: fuzzy dark matter, quintessence, dark fluid, inflation, dilatons, moduli, etc. are some examples. Quintessence models [8] aim to explain dark energy by a dynamical scalar field that could have had an impact at an earlier stage of the Universe like the freezing models or in the future like the thawing models. Fuzzy Dark Matter models based on an ultralight scalar field dominated by its mass term ($m \sim 10^{-22}$ eV) that interacts only gravitationally can reproduce the observed galaxy rotation curves [9] and explain cold dark matter [6]. It is questionable whether all these scalar fields are independent. The Dark Fluid model aims to unify Fuzzy Dark Matter and quintessence and a further step is to unify Dark Fluid with inflation.

As mentioned earlier, a scalar field is not the only possible solution to the cold dark matter problem. Recently, primordial black holes have reappeared as a potential solution to this problem. With the first detection of the gravitational waves from binary black hole merger: GW150914 [10], this opens up new opportunities completely independent of electromagnetic radiation to study the Universe and test General Relativity in strong field regime. After this first detection, many others followed and the population of black holes is being studied. The detection of a black hole with a mass close to one solar mass would be an important clue of the existence of a primordial black hole, because a stellar black hole is expected to have a mass higher than $4 - 5$ solar masses.

The work I will present here is composed of two large independent parts motivated by

cold dark matter.

In the first part, a cosmological scalar field dominated by its mass term $m \sim 10^{-22}$ eV is considered as a viable alternative to cold dark matter. Such a model is called Fuzzy Dark Matter. If its potential is fairly well constrained in the weak field regime by the Cosmic Microwave Background [11], for example, we will see, this is not the case in the strong field regime. In the case where the potential of a scalar field is dominated by a constant then, it can replace the dark energy component of the Universe. After reviewing these models, we consider the most general potential of the Dark Fluid model, which aims at unifying the two unknown components of the Universe compatible with observations. The main key ingredient is the domination of a mass term during the dark matter area that leads to a quickly oscillated scalar field around a minimum, but a non-zero minimum to create the new recent acceleration of the Universe. A further step will be done by considering that inflation could be created by Dark Fluid. Or rather, that inflation is a consequence of a non-minimal coupling between dark fluid scalar field and gravity. In the early Universe, scalar fields are weakly constrained but there are constraints due to the Big-Bang nucleosynthesis. The upper limits on the energy density of scalar fields will be calculated considering the observed primordial abundance of the following elements: helium-4, deuterium and helium-3. Unfortunately, the addition of a scalar field to the ΛCDM model does not solve the lithium problem.

In the second part, primordial black holes are considered as a viable alternative to cold dark matter. This requires specific masses around 10^{20}g or 10^{50}g to explain the whole dark matter component [5] but primordial black holes around 1 $M_\odot$ can still constitute a significant part of this unknown matter. The GW190814 event [12] with a compact object of 2.6 $M_\odot$ is unexpected because it appears too large to be a neutron star and too small to be a black hole. It is therefore important to determine the conditions under which a neutron star or a compact star can mimic a primordial black hole of the same mass in the light of gravitational wave-forms. This will obviously depend on the stiffness of the equation of state and the quality of the data. To give a quantitative answer, the odds number can be computed with Bayesian analysis to select between two competing models.

More precisely, chapter 1 is a short introduction to the ΛCDM model. For more details there are several good textbooks [13–15] and my favorite is Scott Dodelson's which explains modern cosmology. In chapter 2, the homogeneous evolution of scalar fields that mimic dark matter and/or dark energy is presented. The main result is the possible shape of the most general potential for Dark Fluid models. Chapter 3 presents a new model that aims to unify: dark matter, dark energy and inflation. This model has been published in [16]. The last chapter of the first part gives the limits of the energy density of stable and decaying scalar fields considering Big-Bang nucleosynthesis and the observed abundance of helium, helium-3 and deuterium. These limits have been published in [17].

The second part begins with chapter 5. It starts with the interest of studying primordial black holes and ends with a quick introduction to numerical relativity within the Einstein Toolkit framework [18] to produce gravitational wave-forms. More details on numerical relativity can be found in the following textbook [19] and a pedagogical explanation of the $3+1$ formalism in [20]. Chapter 6 is the article [21] which introduced the scaling relations in General Relativity that are used in numerical relativity. Their limits are explored by

considering Hawking radiation and cosmological expansion for primordial black holes. In addition, scaling relations for exotic black holes are being explored and the observation of a break in these scaling relations upon detection of gravitational waves would be an indication of physics beyond Einstein's standard relativity. Finally, Chapter 7 is motivated by the GW190814 event [12] with the detection of a 2.6 solar mass compact object of unknown nature and we explore how gravitational wave-forms produced by primordial black holes could mimic neutron stars [22].

The first appendix is the list of abbreviations and acronyms. Appendix B is a summary of my main results from Part I that was written for the ICHEP conference [23].

Part I

Cosmological Scalar Fields

1 The ΛCDM model

First, we review the standard cosmological model called ΛCDM based on the cosmological principle, which states that the Universe is isotropic (identical in all directions) and homogeneous (no privileged localization) on a sufficiently large scale. According to the ΛCDM model, more than 95% of the total energy of the Universe is unknown, and the natures of dark energy and dark matter remain two of the most important unresolved questions.

Contents

1.1 The expanding Universe

1.1.1 Scale factor

In 1929, Hubble discovered that the Universe is expanding. In other word, the distance between two galaxies is smaller in the early Universe than today. This can be understood by the metaphor of the balloon. The balloon corresponds to a 2 dimensional Universe and the points drawn on the balloon represent the positions of the galaxies. The comoving distance calculated from the coordinates between two points or two galaxies remains always

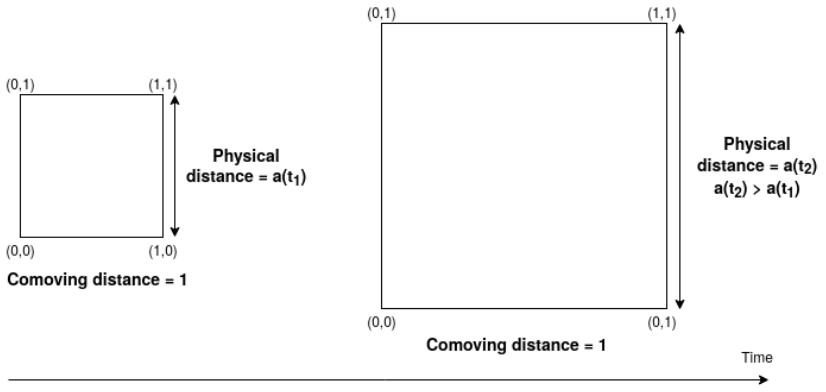

Figure 1.1 – Difference between the physical distance and the comoving distance in an expanded Universe.

constant. But, if the balloon inflates, the physical distance which is proportional to the scale factor a changes. Fig. 1.1 shows an expansion of the Universe where the comoving distance and the physical distance are represented.
Let us consider a comoving trajectory $\vec{x}(t)$ of a galaxy. Its physical trajectory is:

$$\vec{x}_{ph} = a(t)\vec{x}(t) \tag{1.1}$$

and its physical velocity is the derivative of Eq. (1.1) which leads to:

$$\vec{v}_{ph}(t) = \frac{d\vec{x}_{ph}}{dt} = \frac{da}{dt}\vec{x}_{ph} + a\frac{d\vec{x}}{dt} = H\vec{x}_{ph} + \vec{v}_{pe} \tag{1.2}$$

where $\vec{v}_{pe}$ is the peculiar velocity close to 400 km/s for a typical galaxy and H is the Hubble rate which characterizes the variation of the scale factor. The present Hubble rate of the Universe called the Hubble constant H_0 is measured by different methods. A first method is to determine the proportionality coefficient between the physical velocities and their distances which leads to [24]:

$$H_0 = 100h \text{ km/s/Mpc} \tag{1.3}$$

with $h = 0.72 \pm 0.08$. Another possibility is to measure the Hubble constant by the Cosmic Microwave Background (CMB), its value is given in Table 1.1.

1.1.2 Friedmann equations

A spacetime is defined by a manifold $\mathcal{M}$ with a metric $g_{\mu\nu}$. For a spatially homogeneous and spatially isotropic Universe, the spacetime $(\mathcal{M}, g_{\mu\nu})$ admits a foliation of hypersurfaces Σ_t parameterized by the continuous cosmological time t such that [25]:

$$g_{\mu\nu}dx^\mu dx^\nu = -c^2dt^2 + \gamma_{ij}dx^i dx^j \,, \tag{1.4}$$

Parameter	Definition	Observational value
$\omega_b = \Omega_b^0 h^2$	Baryon cosmological parameter	0.02237 ± 0.00015
$\omega_c = \Omega_c^0 h^2$	Cold dark matter cosmological parameter	0.1200 ± 0.0012
Ω_Λ	Cosmological constant parameter	0.6847 ± 0.0073
H_0	Hubble constant in km/s/Mpc	67.36 ± 0.54
z_{eq}	Redshift of matter-radiation equality	3402 ± 26

Table 1.1 – Data from Planck 2018 results [2]. Ω_X^0 is defined as the ratio of the current energy density of component X over the present critical density, and h is the reduced Hubble constant $h = H_0/(100$ km/s/Mpc).

where x^i and γ_{ij} are respectively the coordinates and the induced metric on Σ_t. In (1.4), there are no terms in $dtdx^i$; and (Σ_t,γ_{ij}) must be a maximally symmetrical space of 3 dimensions. Then [25]:

$$\gamma_{ij}dx^i dx^j = \begin{cases} a(t)^2\left[dr^2 + r^2(d\theta^2 + \sin^2\theta d\phi^2)\right] & \text{(Euclidean space } \mathbb{R}^3\text{)} \\ a(t)^2\left[d\chi^2 + \sin^2\chi(d\theta^2 + \sin^2\theta d\phi^2)\right] & \text{(hypersphere } \mathbb{S}^3\text{)} \\ a(t)^2\left[d\rho^2 + \sinh^2\rho(d\theta^2 + \sin^2\theta d\phi^2)\right] & \text{(hyperbolic space } \mathbb{H}^3\text{)} \end{cases} . \tag{1.5}$$

After coordinate transformations, the metric (1.4) can be rewritten as follows:

$$g_{\mu\nu}dx^\mu dx^\nu = -c^2dt^2 + a(t)^2\left[\frac{dr^2}{1-kr^2} + r^2(d\theta^2 + \sin^2\theta d\phi^2)\right] , \tag{1.6}$$

which is called the Friedmann Lemaître Robertson Walker (FLRW) metric with:

$$k = \begin{cases} 0 & \text{(Euclidean space } \mathbb{R}^3\text{)} \\ 1 & \text{(hypersphere } \mathbb{S}^3\text{)} \\ -1 & \text{(hyperbolic space } \mathbb{H}^3\text{)} \end{cases} . \tag{1.7}$$

A flat universe characterized by a zero curvature is Euclidean. A closed Universe is described by a hypersphere with positive curvature. In such a space, two particles moving freely and initially parallel will converge. An open Universe is described by a hyperbolic space with negative curvature.

With the metric (1.4), to solve the Einstein equations:

$$R_{\mu\nu} - \frac{1}{2}g_{\mu\nu}R + \Lambda g_{\mu\nu} = \frac{8\pi G}{c^4}T_{\mu\nu} , \tag{1.8}$$

it is necessary to determine the stress-energy tensor $T_{\mu\nu}$. For a perfect fluid, this tensor is defined by:

$$T_{\mu\nu} = \left(\rho c^2 + P\right)u_\mu u_\nu + P g_{\mu\nu} , \tag{1.9}$$

with ρc^2 the matter energy density of the fluid, P the pressure and $u^\alpha = (1,0,0,0)$ the 4-velocities. In General Relativity, the continuity equations are imposed by the vanishing

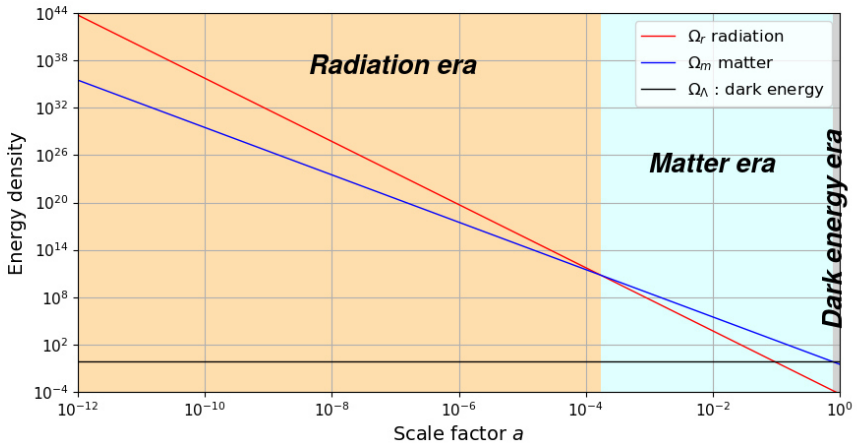

Figure 1.2 – Evolution of the energy density fractions of radiation, matter and dark energy as function of the scale factor. The shaded areas show the different epochs of the Universe.

of the covariant derivative of the stress-energy tensor. In the expanding Universe, the conservation law for a perfect fluid gives:

$$\frac{d\rho}{dt} + 3\frac{\dot{a}}{a}\left(\rho + \frac{P}{c^2}\right) = 0\,. \tag{1.10}$$

To solve this equation, it is necessary to know the equation of state $\omega = P/\rho c^2$. Two standard cases can be distinguished:

- $\omega = 0$ corresponding to a fluid with null pressure, dust or cold dark matter are some examples.
- $\omega = 1/3$ corresponding to radiation.

For a constant equation of state, the Eq. (1.10) can be easily solved and the energy density is proportional to a power of the scale factor a:

$$\rho = \rho_0 \left[\frac{a_0}{a}\right]^{3(1+\omega)}\,. \tag{1.11}$$

Finally, Einstein's equations in an isotropic and homogeneous Universe in the $x^\mu = (ct, r, \theta, \phi)$ coordinates give the following two equations:

$$\begin{aligned} \left(\frac{\dot{a}}{a}\right)^2 + \frac{c^2 k}{a^2} &= \frac{8\pi G}{3}\rho + \frac{c^2\Lambda}{3}\,, \\ \frac{\ddot{a}}{a} &= -\frac{4\pi G}{3}\left(\rho + 3\frac{P}{c^2}\right) + \frac{c^2\Lambda}{3}\,, \end{aligned} \tag{1.12}$$

called Friedmann equations. The first equation corresponds to the tt component and the second to the rr component. The others are trivial. These two differential equations describe the evolution of $a(t)$, $\rho(t)$ and $P(t)$. This system is closed by an equation of state. In the following, we use the natural unit system with $c = 1$.

1.1.3 Composition of the Universe

The ΛCDM model assumes the existence of a cold dark matter and a cosmological constant Λ whose natures are still an open issue. Currently, after 14 billion years of evolution, the abundance of the different species constituting the Universe, is represented by the diagram of Fig. 1.3. As we can see, more than 95% of the Universe is unknown. These proportions between the various species evolve with the Universe expansion. For example, during Big-Bang nucleosynthesis, radiation dominates the Universe, and dark energy is negligible. There are three main eras of domination: the radiation era, the matter era and the dark energy era. Fig. 1.2 shows the evolution of these quantities as a function of the scale factor a following:

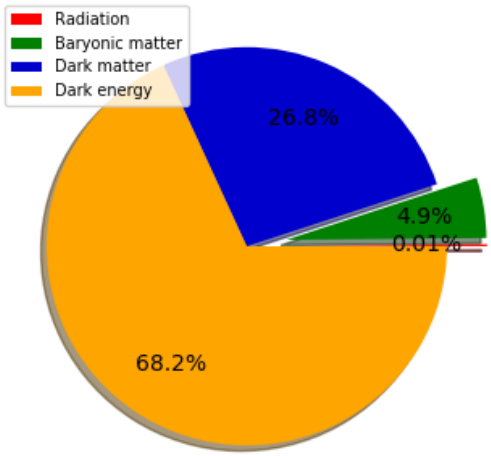

Figure 1.3 – In the ΛCDM model, the Universe is constituted of radiation, baryonic matter, cold dark matter and dark energy.

- **Radiation:** relativistic species whose rest mass energy is negligible compared to its kinetic energy: $E(p) = \sqrt{p^2 + m^2} \simeq p$. At equilibrium at temperature T, the energy density of such a species is:

$$\rho = g \int \frac{d^3p}{(2\pi)^3} \frac{1}{\mathrm{e}^{(E-\mu)/T} \pm 1} E \tag{1.13}$$

and the pressure is:

$$P = g \int \frac{d^3p}{(2\pi)^3} \frac{1}{\mathrm{e}^{(E-\mu)/T} \pm 1} \frac{p^2}{3E} \tag{1.14}$$

where the $+1$ is for a Fermi-Dirac distribution and -1 for a Bose-Einstein distribution. The constant g is the degeneracy of this species and μ is the chemical potential. As expected, for $E = p$, the energy density is proportional to the pressure with a factor $1/3$ which means that the equation of state is $\omega = 1/3$. Today, the radiation is composed of photons and neutrinos. Cosmic Microwave Background (CMB) photons have been detected at the temperature $T_0 = 2.725\mathrm{K}$ measured by the Planck collaboration. The CMB appears as a perfect black body radiation. The energy density of photons is given by Eq. (1.13) with $x = p/T$:

$$\rho_\gamma = 2 \times \frac{4\pi}{(2\pi)^3} \int_0^{+\infty} \frac{x^3 dx}{\mathrm{e}^x - 1} = \frac{\pi^2}{15} T^4 \tag{1.15}$$

where the factor 2 represents the two polarizations of photons and the chemical potential can be safely ignored [26]. Since the density evolves like a^{-4} for radiation, the

temperature T scales as a^{-1}. Unlike cosmological photons, cosmological neutrinos have not been observed. Neutrinos follow the Fermi-Dirac distribution, but today their interactions are too weak to remain in equilibrium with photons. Photons and neutrinos can therefore have different temperatures. In the early Universe, when the Universe is hotter and denser, photons and neutrinos are in equilibrium with the same temperature; but with the expansion of the Universe, neutrinos and photons are decoupled. In this hypothesis, the temperatures of photons and neutrinos are identical, but electrons and positrons will annihilate and reheat the photon temperature. Before this annihilation, radiation is composed of: photons (2 degrees of freedom), electrons e^- (2 spin states), positron e^+ (2 spin states), neutrinos (3 species with 1 spin state) and antineutrinos. Thus, the entropy density $s = (\rho + P)/T = 4\rho/3T$ scaling as a^{-3} is given by:

$$s_1 = \frac{2\pi^2}{45} T^3 \left(2 + \frac{7}{8}(2+2+3+3)\right) = \frac{43\pi^2}{90} T^3 \tag{1.16}$$

where the factor 7/8 comes from the difference between bosons and fermions. After the annihilation, the radiation is composed of photons (temperature T_γ) and neutrinos (temperature T_ν). Thus,

$$s_2 = \frac{2\pi^2}{45} \left(2T_\gamma^3 + \frac{21}{4} T_\nu^3\right) \tag{1.17}$$

Even during annihilation, temperature of neutrinos scales as a^{-1} and aT is constant for this species. Assuming that annihilation does not create entropy $s_1 a_1^3 = s_2 a_2^3$, we obtain:

$$\frac{T_\nu}{T_\gamma} = \left(\frac{4}{11}\right)^{1/3} \tag{1.18}$$

Today, the energy density of radiation is:

$$\rho_r = \rho_\gamma + \rho_\nu = \left(1 + 3\frac{7}{8}\left(\frac{4}{11}\right)^{4/3}\right) \frac{\pi^2}{15} T_0^4 \tag{1.19}$$

which represents about 0.01% of the total energy density of the Universe.

- **Matter:** baryonic matter in the Universe can be observed thanks to the electromagnetic radiation interacting with this matter. The observed clouds of matter are mainly composed of hydrogen and most of their atoms are ionized. But this density of matter constitutes only 16% of the total matter density. There is a matter that does not interact with light and for now, only its impact by gravitational effects has been detected. This matter is called cold dark matter. In the following, the matter is considered as the sum of the cold dark matter and the baryonic matter. This matter is modeled by zero pressure, which leads to a scaling of a^{-3}. The observational values given by the Planck collaboration are shown in Table 1.1.

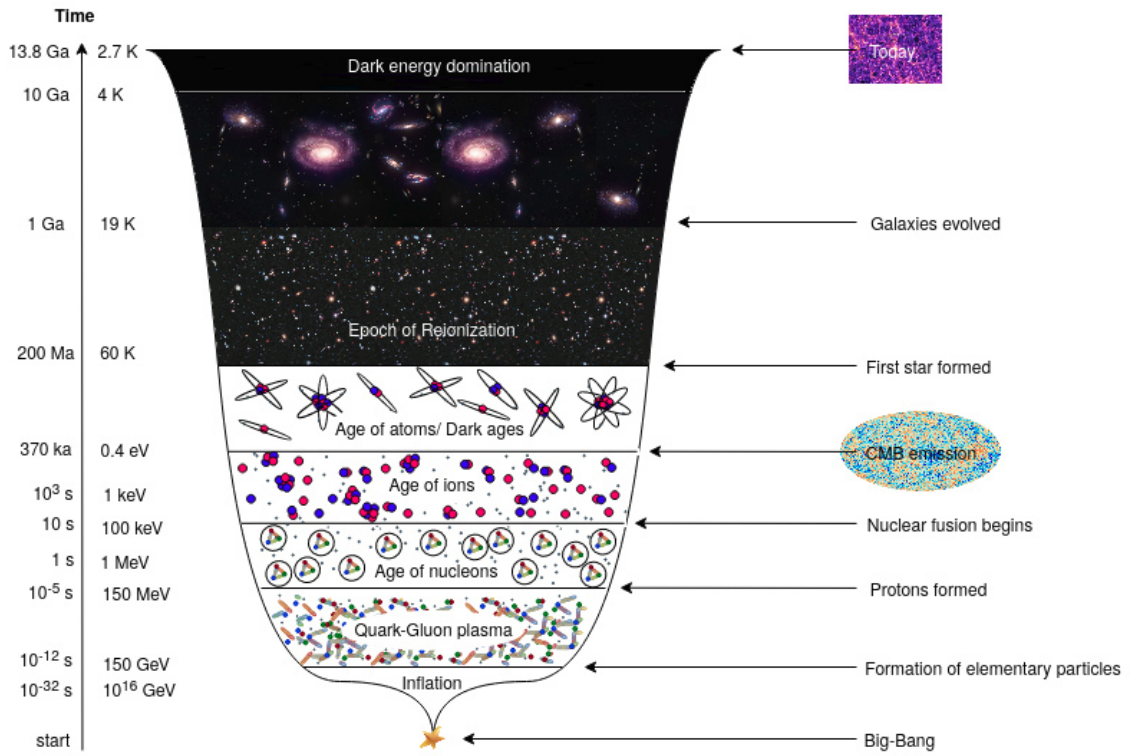

Figure 1.4 – Chronology of the Universe based on the Big-Bang model.

- **Dark energy:** is the reinterpretation of the cosmological constant Λ which appears in the Friedmann equations (1.12) as a negative pressure fluid: $P_\Lambda = -\rho_\Lambda$. Such fluid is introduced in the ΛCDM model to explain the recent acceleration of the Universe.

Table 1.1 gives the main cosmological parameters which will be used in the following.

1.2 A brief history of the Universe

The origin and evolution of the Universe are described by the cosmological model called *Big-Bang*. The age of the Universe is about 14 billion years, which corresponds to a temperature of $T_0 = 2.7$ K. Today, the scale factor $a = a_0$ is generally set to 1. In the past, the Universe was smaller $a < 1$ and hotter $T > 2.7$ K. In cosmology, the temperature often substitutes for time to describe the evolution of the Universe because it is a great indicator of the appearance of phase transitions (recombination, nuclear fusion, protons formed, electroweak transition, ...). Fig. 1.4 summarizes the chronology of the Universe since the Planck energy and the big steps are listed below.

The beginning of the physical Universe can be considered as the Planck scale and no theory can describe it correctly. The quantum effects of gravity dominate its evolution and it is possible that the four fundamental forces are unified.

After Big-Bang, the Universe grows extremely fast and this period is called inflation. Between $10^{-33} - 10^{-32}$ s the Universe expands by a factor of the order of 10^{26}. In other words, the number N of e-folds is greater than 50: $\log(a_{end}/a_{beg}) \geq 50$ where a_{beg} and a_{end} is respectively the scale factor at the beginning and the end of inflation. There is no direct experiment which demonstrates the existence of inflation, but it is the solution to solve the flatness and horizon problems. At the end of inflation, the inflaton must decay into particles that will give the Standard Model.

At 150 GeV, an energy a little higher than the Higgs mass, the temperature is not sufficient to keep electromagnetism and weak interaction into a single electroweak interaction. The $SU(2) \times U(1)_Y$ symmetry is broken into $U(1)_{EM}$. The vacuum expectation value of the Higgs field is no longer zero. The 3 bosons of the electroweak interaction become massive with a massless photon.

For a temperature between 150 GeV and 150 MeV, the Universe is a soup of quark known as the quark-gluon plasma. It is filled with quarks, leptons and their antiparticles. But, for a temperature below 150 MeV, baryons and mesons are produced. The majority of hadrons will be protons and neutrons.

At 1 MeV, the equilibrium between electrons, positrons, neutrinos and antineutrinos is broken. The rate Γ of the reaction:

$$e^+ + e^- \leftrightarrow \nu_e + \bar{\nu}_e \tag{1.20}$$

is given by $n\langle\sigma v\rangle \sim G_F^2 T^5$ where G_F is the Fermi constant. Neutrinos decouple when this rate is approximately equal to the Hubble parameter $H = \sqrt{8\pi/3G\rho} \sim \sqrt{GT^4}$ which leads to a decoupling temperature of:

$$T \sim \left(\frac{\sqrt{G}}{G_F^2}\right)^{1/3} \sim 1 \text{ MeV}\,. \tag{1.21}$$

Thus, for a temperature below 1 MeV, neutrinos are no longer in equilibrium with photons, electrons, positrons ... The Universe becomes transparent for neutrinos, which produced the emission of the cosmic neutrino background. This emission has not been detected yet.

Between 100 keV and 1 keV, protons and neutrons fuse to form nuclei. Hydrogen, helium-4, deuterium, helium-3, lithium-7 ... are produced during what is called primordial nucleosynthesis. The Universe is a plasma of nuclei, electrons and photons.

After 370000 years, the Universe had expanded and cooled enough ($T \sim 0.4$ eV), to allow the formation of atoms. Electrons and nuclei bind to form neutral atoms. The Universe becomes transparent: photons can travel freely without scattering with matter. These photons form the Cosmic Microwave Background (CMB) and were emitted during this epoch called recombination.

After recombination, the Universe enters in the dark ages. Photons are no longer emitted until the re-ionization. Hydrogen clouds form and collapse into stars and galaxies. The formation of the first starts and galaxies is still under debate, but it is approximately 300 mega years after the Big-Bang. Thereafter, galaxies coalesce into clusters and superclusters of galaxies.

It is only recently that the expansion of the Universe has begun to accelerate. The Λ-CDM model explain this acceleration with a negative pressure fluid.

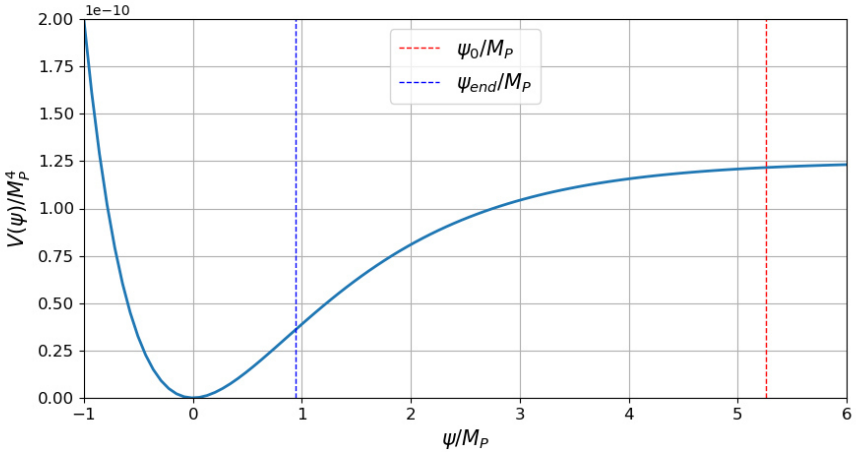

Figure 1.5 – Potential $U(\psi)$ defined in Eq. (1.28) as a function of ψ. Inflation starts at the dashed red line and ends at the dashed blue line.

1.2.1 Inflation

As mentioned earlier, inflation was introduced to solve the horizon problem. This problem appears with the homogeneity and anisotropy of the CMB. In all sky directions, the CMB has the same temperature even if the regions are not causally connected. Therefore, the last scattering of photons can not be in equilibrium. The comoving Hubble radius $(aH)^{-1}$ is a way to know if the particles are in causal contact. The scale $\lambda = 2\pi a/k$ is outside the horizon if the wave-number k is smaller than aH. During inflation, the comoving Hubble rate must decrease dramatically and therefore aH has to be increased:

$$\frac{d}{dt}(aH) \simeq \frac{d^2a}{dt^2} > 0\,. \tag{1.22}$$

Solving the horizon problem means having an accelerated expanding period called inflation. With the Friedmann equations (1.12), in order to have an accelerated expansion, it is necessary to have a negative pressure fluid such that $P < -\rho/3$. Such a behavior can be obtained with a scalar field dominated by its potential. The energy density and the pressure of a scalar field ϕ are given by:

$$\begin{aligned} \rho &= \frac{\dot{\phi}^2}{2} + U(\phi)\,, \\ P &= \frac{\dot{\phi}^2}{2} - U(\phi)\,, \end{aligned} \tag{1.23}$$

which leads to $P \simeq -\rho$ if the kinetic term $\dot{\phi}^2/2$ is negligible as compared to the potential term U and an expansion of 55 e-fold solves also the flatness problem.

The inflation model introduced by Starobinsky is based on gravity [28]. Assuming this R^2 model to describe inflation, the action is given by:

$$\mathcal{S} = \int d^4x\sqrt{-g}\left[\frac{1}{2\kappa^2}\left(R + \frac{1}{6M}R^2\right)\right]\,, \tag{1.24}$$

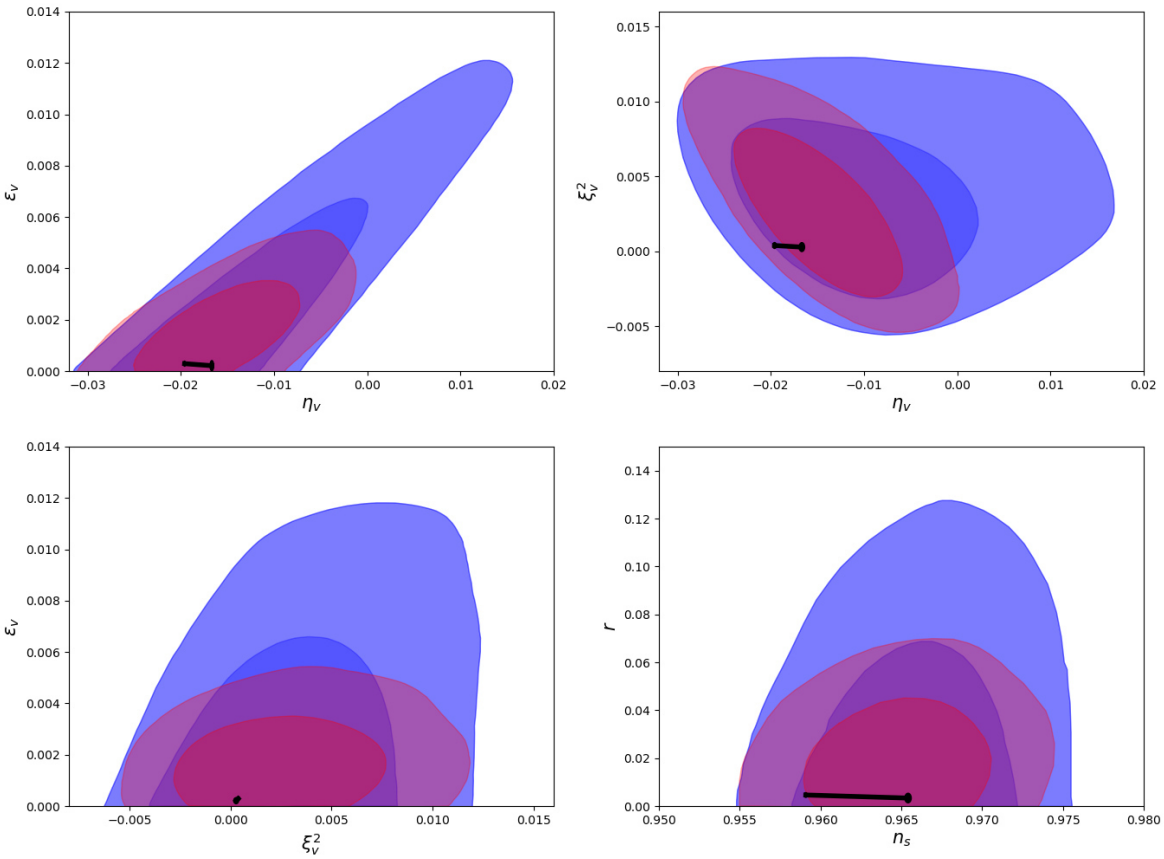

Figure 1.6 – Marginalized joint two-dimensional 68% and 95% C.L. regions for the slow-roll parameters $(\epsilon_v, \eta_v, \xi_v^2)$, and the tensor to scalar ratio r as a function of the scalar spectral index n_s. The two-dimensional constraints are obtained by the Planck collaboration [27] using TT,TE,EE+lowE+lensing data (blue contours) and TT,TE,EE+lowE+lensing+BK15 data (red contours). The black lines correspond to the values of the R^2-inflation model for $50 < N < 60$. The big black dot is calculated with $N = 60$ and the small one with $N = 50$.

where M is a constant, fixed by the amplitude of CMB power spectrum (see equation (1.34)). This action corresponds to the $f(R) = R + R^2/(6M^2)$ theory. Starobinsky inflation model is known to be a viable inflation scenario. Inflation occurs when $R \gg M^2$ and $H^2 \gg |\dot{H}|$, see [29].

We perform a conformal transformation to find the Einstein frame, with:

$$\Omega^2 = F(R)\,, \tag{1.25}$$

where $F(R)$ is the derivative of $f(R)$. By defining an effective field ψ as:

$$\frac{\psi}{M_P} = \sqrt{\frac{3}{2}} \log F\,, \tag{1.26}$$

the action becomes:

$$\mathcal{S} = \int d^4x\sqrt{-\tilde{g}}\left[\frac{1}{2\kappa^2}\tilde{R} - \frac{1}{2}\tilde{g}^{\mu\nu}\partial_\mu\psi\partial_\nu\psi - U(\psi)\right], \tag{1.27}$$

with

$$U(\psi) = \frac{M_P^2}{2}\frac{FR-f}{F^2} = \frac{3M^2M_P^2}{4}\left[1-\exp\left(-\sqrt{\frac{2}{3}}\frac{\psi}{M_P}\right)\right]^2. \tag{1.28}$$

The tilde in the action denotes quantities in the Einstein frame. Chaotic inflation occurs when the potential dominates the evolution and changes slowly.

The shape of the potential is shown in Fig. 1.5, where one can see that the potential is relatively constant in the region $\psi \gg M_P$. The slow-roll parameters of this potential, which have to be small during inflation, are given by:

$$\begin{aligned}
\epsilon_v &= \frac{M_P^2}{2}\left(\frac{U'}{U}\right)^2 = \frac{4}{3}\left[\exp\left(\frac{2\psi}{\sqrt{6}M_P}\right)-1\right]^{-2}, \\
\eta_v &= M_P^2\frac{U''}{U} = -\frac{4}{3}\frac{\exp\left(\frac{2\psi}{\sqrt{6}M_P}\right)-2}{\left[\exp\left(\frac{2\psi}{\sqrt{6}M_P}\right)-1\right]^2}, \\
\zeta_v^2 &= M_P^4\frac{U'''U'}{U^2} = \frac{16}{9}\frac{\exp\left(\frac{2\psi}{\sqrt{6}M_P}\right)-4}{\left[\exp\left(\frac{2\psi}{\sqrt{6}M_P}\right)-1\right]^3}.
\end{aligned} \tag{1.29}$$

The end of inflation is characterized by $\epsilon_v = 1$ so that

$$\frac{\psi_{end}}{M_P} = \sqrt{\frac{3}{2}}\ln\left(1+\frac{2}{\sqrt{3}}\right) \simeq 0.94. \tag{1.30}$$

The number of e-folds is given by:

$$\begin{aligned}
N = \frac{1}{M_P^2}\int_{\psi_{end}}^{\psi_{beg}}\frac{U}{U'}d\psi = \frac{3}{4}\Bigg[&\left(\exp\left(\sqrt{\frac{2}{3}}\frac{\psi_{beg}}{M_P}\right) - \sqrt{\frac{2}{3}}\frac{\psi_{beg}}{M_P}\right) \\
&- \left(\exp\left(\sqrt{\frac{2}{3}}\frac{\psi_{end}}{M_P}\right) - \sqrt{\frac{2}{3}}\frac{\psi_{end}}{M_P}\right)\Bigg],
\end{aligned} \tag{1.31}$$

and one obtains for $N = 55$

$$\frac{\psi_{beg}}{M_P} \simeq \sqrt{\frac{3}{2}}\ln\left(\frac{4}{3}N\right) \simeq 5.26. \tag{1.32}$$

The scalar spectral index [30] and the tensor to scalar ratio can also be obtained by $n_s = 1 - 6\epsilon_v + 2\eta_v$ and $r = 16\epsilon_v$, respectively. The CMB observations by Planck set constraints on slow-roll parameters [31], which are presented in Fig. 1.6. Therefore, the predictions are in agreement at the one sigma level with Planck observational data.

In order to obtain the value of αv^2, we will use the amplitude of the power spectrum which is connected to the potential by [32]:

$$\delta_H^2 = \frac{4}{25}\mathcal{P}_\mathcal{R} = \frac{1}{150\pi^2 M_P^4}\frac{V}{\epsilon_v}\,. \tag{1.33}$$

The evaluation of this expression at the end of inflation, which corresponds to $N \simeq 55$ and $\delta_H \simeq 2 \times 10^{-5}$, gives:

$$M \simeq 3 \times 10^{-6} m_P\,. \tag{1.34}$$

with $m_P = \sqrt{8\pi} M_P$. This equality fixes the free parameter of the R^2 model.

1.2.2 Big-Bang nucleosynthesis

The abundance of the elements in the Universe is related by primordial nucleosynthesis. The key ingredient is the synthesis of deuterium:

$$p + n \to D + \gamma\,. \tag{1.35}$$

For a temperature of 1 MeV, when the Universe is hotter and denser, the nuclei can not bind. If deuterium is formed, it will be immediately destroyed by high energy photons. At that time, the Universe is dominated by radiation and the ratio between protons and neutrons is close to one, but with the expansion of the Universe described by the Friedmann equations, the proton-neutron equilibrium given by the following relations:

$$\begin{aligned} n + e^+ &\leftrightarrow \bar{\nu}_e + p\,, \\ n + \nu_e &\leftrightarrow p + e^- \end{aligned} \tag{1.36}$$

is broken and there is a freeze out. At 0.1 MeV, which corresponds to 10^9 K, beta decay occurs and the deuterium starts to be synthesized with a n/p ratio close to 12%. The light elements are formed and the main reactions are given in the left panel of Fig. 1.7. The element most produced by the Big-Bang nucleosynthesis (BBN) is helium-4 with a mass fraction of 25%. Deuterium, helium-3, beryllium-7, lithium-7 are produced in small quantities. At 1 keV, the temperature is not high enough and the BBN stops. The predicted BBN abundances are shown in the right panel of Fig. 1.7. The thick lines represent theoretical predictions and the boxes and arrows observational measurements. The solid vertical band is the region that is compatible between theory and measurements, leading to a measurement of the baryon density (neutron and proton density) in Universe during the BBN.

1.2.3 Cosmic Microwave Background

After 370000 years of evolution, the Universe was cold enough to allow the formation of atoms. At that time, the Universe became transparent to photons because the light was no longer being scattered off free electrons. These photons follow the black body spectrum given by the Planck's law:

$$I(\nu, T) = \frac{2h\nu^3}{c^2}\frac{1}{\exp\left(h\nu/k_B T\right) - 1}\,, \tag{1.37}$$

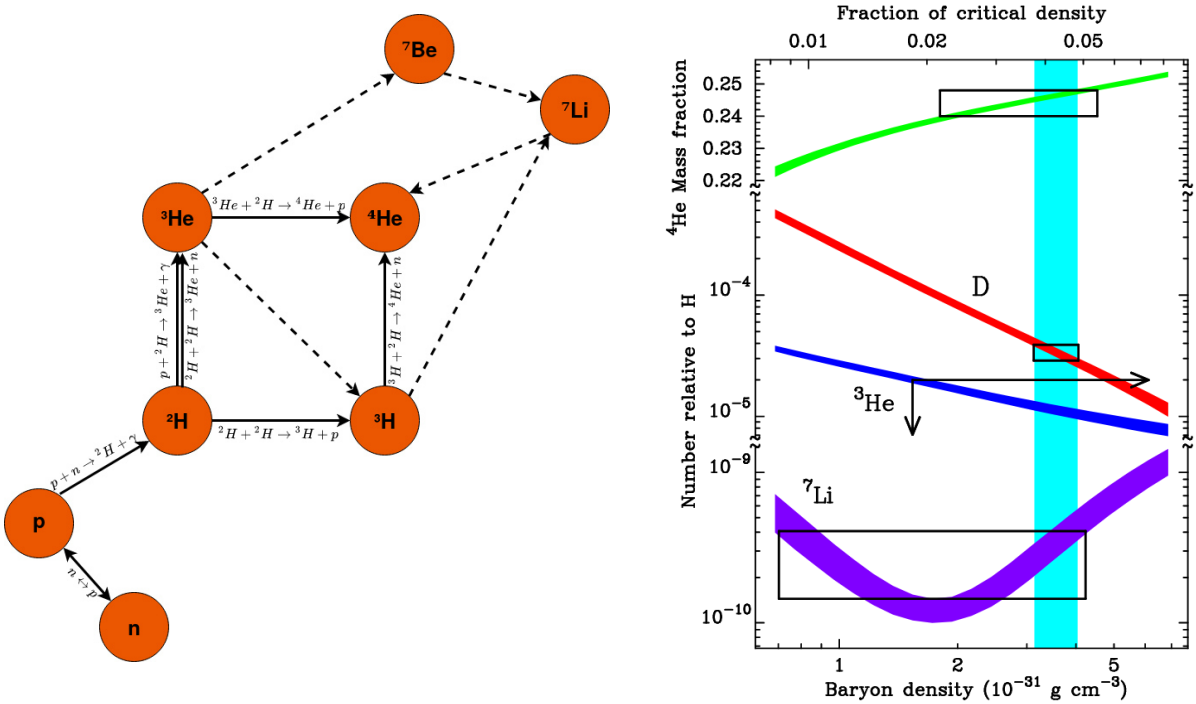

Figure 1.7 – Left panel: diagram of the Big-Bang nucleosynthesis with the main reactions. Right panel: predicted abundances of the light nuclei from the Big-Bang nucleosynthesis from [33].

where the temperature is measured at 2.7 K. The CMB measurements impose many constraints on the cosmological parameters. Some of them are given in Table 1.1. In addition, the Planck collaboration provides constraints on w_ϕ: the dark energy equation of state [2]. Depending on the parameterization of w_ϕ, the article [34] gives the following constraints:

- if w_ϕ is constant, measurements impose:

$$w_\phi = -1.028 \pm 0.032\,, \tag{1.38}$$

- if w_ϕ is described by a linear fit as a function of the scale parameter a such that $w_\phi(a) = \omega_0 + (1-a)\omega_a$ with ω_0 and ω_a constant, measurements impose:

$$\begin{aligned} \omega_0 &= -0.961 \pm 0.077\,, \\ \omega_a &= -0.28^{+0.31}_{-0.21}\,. \end{aligned} \tag{1.39}$$

In addition the Planck collaboration gives limits on the early dark energy (EDE) cosmological parameter $\Omega_{EDE}(z)$, which is the proportion of dark energy density to the total energy density at redshift z [35]. These constraints are [36]:

- $\Omega_{EDE} \leq 4\%$ (95% C.L.) at redshift $z = 10$,
- $\Omega_{EDE} \leq 2\%$ (95% C.L.) at redshift $z = 50$,
- $\Omega_{EDE} \leq 1.6\%$ (95% C.L.) at redshift $z = 200$,
- $\Omega_{EDE} \leq 1.3\%$ (95% C.L.) at redshift $z = 1000$.

1.3 Beyond the standard model

1.3.1 Galaxy rotation curves

In 1933, the astronomer Fritz Zwicky discovered the missing matter by studying the dynamical evolution of the Coma cluster. The theoretical study of the evolution of the observed luminosity mass does not correspond to the real dynamics. He then suggested the existence of invisible matter in galaxy cluster called dark matter. Moreover, with the development of radiotelescope, galaxy rotational curves can be measured. Far from the center of the galaxies, these curves are generally flat, whereas the theory predicts a decrease as $1/\sqrt{r}$ following the Keplerian dynamics where r is the distance to the galaxy center. Consequently, the galaxies seem to be surrounded by a dark matter halo.

As demonstrated in the papers [9, 37, 38], a simple complex scalar field with $U(1)$ symmetry based on the Lagrangian density:

$$\mathcal{L}_\phi = g^{\mu\nu}\partial_\mu\phi^\dagger\partial_\nu\phi + U(\phi)\,, \tag{1.40}$$

can reproduce the galaxy rotation curves of dwarf galaxies. The calculations assume an internal rotation for the scalar field $\phi = \sigma(r)\exp(i\omega t)$ associated to a quadratic potential with anharmonic corrections. A result for the dwarf spiral DDO 154 is shown in Fig. 1.8. In this figure, the visible matter called baryonic matter does not reproduce rotation curve but, by adding a dark halo described by a complex scalar field, the observed rotation curve is reproduced. Such a model based on a low mass scalar field is called Fuzzy Dark Matter and we will study it in more detail in the next chapter from a cosmological point of view.

1.3.2 Conclusion and dark sector

The nature of dark energy and dark matter is still an unresolved mystery in cosmology. Baryon asymmetry in the Universe, baryogenesis and inflation also necessitate new phenomena in the early Universe. Many cosmological models for such phenomena involve scalar fields, and with the discovery of a Standard Model Higgs boson [39, 40] the existence of fundamental scalar fields has been proven.

Cosmological observations can be explained by assuming the existence of cold dark matter (CDM) and of a cosmological constant Λ [2], forming the cosmological standard model ΛCDM. The cosmological constant represents about two-third of the present total energy density in the Universe, whereas CDM and baryons constitute the remaining energy density. CDM is a pressureless component, and the cosmological constant has a negative pressure and constant density. At the time of recombination and emission of the Cosmic Microwave Background (CMB), the dominating energy density was that of radiation, and the baryon and CDM densities were subdominant but left specific imprints on the CMB, and the cosmological constant was completely negligible. Before recombination, radiation is assumed to dominate, and in the very early Universe the expansion is expected to be exponential during the inflation period.

The cosmological constant can be replaced by a dark energy with a nearly constant density today [8, 41–46]. Contrary to the cosmological constant, dark energy is driven by a dynamical mechanism. Quintessence models, for example aim at explaining dark energy

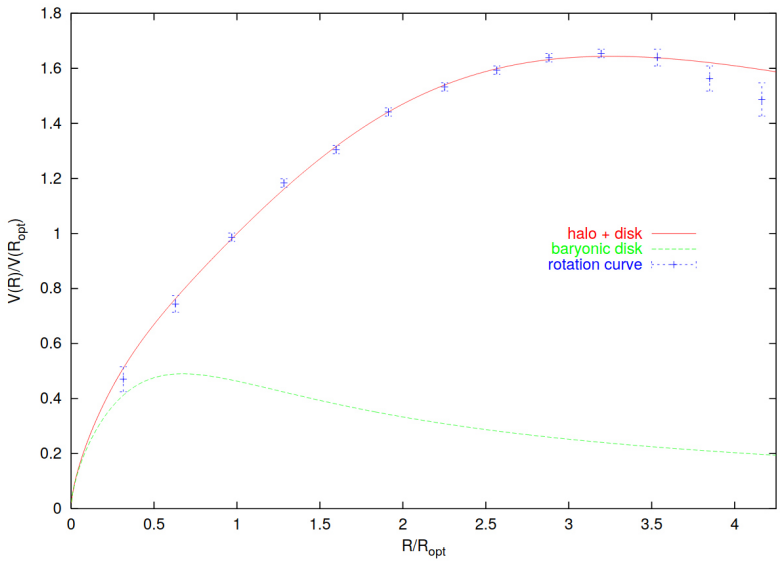

Figure 1.8 – Rotation curve of the dwarf spiral DDO 154 from [38]. The blue dots represent the direct measurement of the rotation curve and the green curve is the expected rotation curve with the visible matter. The red line is the rotation curve calculated by adding a scalar field.

with a cosmological field [41, 42]. The form of its potential is clearly unknown, and many different potentials have been studied and confronted with observations, and a large variety of models are still compatible with observational data.

Typical dark matter models involve weakly-interacting massive particles (WIMPs), which can be scalar particles still undiscovered at colliders and dark matter detection experiments. Models for dark matter can also be based on other kinds of scalar fields. This is for example the case of fuzzy dark matter [6] or spintessence [47], in which the scalar field oscillates quickly, acquiring in average a pressureless matter behaviour. At galactic scales, it can form a galactic halo through Bose-Einstein condensation, with a typical size given by the Compton wavelength of the scalar field. Such models need a quadratic term in the potential with a mass as low as 10^{-23} eV, and therefore the scalar field does not behave like particles. Such models have the advantage of not suffering from the so-called cuspy halo and missing satellite problems [48].

On the other hand, the dark fluid model [49–51] describes a cosmological component which behaves at galactic scales as dark matter and at large scales like dark energy, replacing both components by a single one. Such a model can rely on a scalar field with a specific potential [52–54].

2

Scalar fields in cosmology

In this chapter different models based on scalar fields will be presented. Fuzzy Dark Matter (FDM) models introduce a scalar field that behaves like dark matter, quintessence models can explain the recent acceleration of the expansion of the Universe, and dark fluid models aim at unifying dark energy and dark matter with the same and unique scalar field. The potential of these models is still an open question and we will focus on the evolution of cosmological scalar fields at the time of the Big-Bang nucleosynthesis, which may affect the formation of heavy nuclei.

Contents

2.1 Dark energy scalar fields

Cosmological scalar fields are often used to explain dark energy, and typical models include quintessence [8,55]. In this section, we consider such a scalar field, and the cosmological constant is set to zero in the equations and replaced by the real scalar field ϕ. Since

all cosmological observations are currently compatible with a simple cosmological constant, the main features of such scenarios are a scalar field density close to the dark energy value in the present Universe, an equation of state $w_\phi \approx -1$, and a negligible density at the recombination time. We will consider several cases of quintessence scalar fields [8]: scaling freezing model, tracking freezing model and thawing model. For each model, we choose the parameters and initial conditions so that the scalar field density equals the cosmological constant density today.

To solve the evolution equations, we follow [56] and define the reduced variables:

$$\begin{aligned} x &= \frac{\dot{\phi}}{\sqrt{6}M_P H}\,, & u_r &= \frac{\sqrt{\rho_r}}{\sqrt{3}M_P H}\,, \\ y &= \frac{\sqrt{U(\phi)}}{\sqrt{3}M_P H}\,, & u_m &= \frac{\sqrt{\rho_m}}{\sqrt{3}M_P H}\,, \\ & & u_\phi &= \frac{\sqrt{\rho_\phi}}{\sqrt{3}M_P H}\,, \end{aligned} \tag{2.1}$$

where ρ_r, ρ_m and ρ_ϕ refer to radiation, matter (baryonic matter and cold dark matter) and scalar field (dark energy) densities, respectively, and M_P is the Planck mass. With such definitions, the background evolution is given by:

$$\begin{aligned} x' &= \frac{3}{2}x\left(\Pi - 2x\right) + \sqrt{\frac{3}{2}}\lambda y^2\,, & u_m' &= \frac{3}{2}\left(\Pi - 1\right)u_m\,, \\ y' &= \frac{3}{2}\Pi y - \sqrt{\frac{3}{2}}\lambda y x\,, & u_r' &= \frac{3}{2}\left(\Pi - \frac{4}{3}\right)u_r\,, \\ & & u_\phi' &= \frac{3}{2}\Pi u_\phi\,, \end{aligned} \tag{2.2}$$

with the Friedmann constraint:

$$x^2 + y^2 + u_r^2 + u_m^2 + u_\phi^2 = 1\,, \tag{2.3}$$

where the prime denotes a derivative with respect to the logarithm of the scale factor $N = \ln a$, $\lambda = -M_P U'/U$ and Π is defined as:

$$\frac{3}{2}\Pi = \frac{3}{2}\left(2x^2 + u_m^2 + \frac{4}{3}u_r^2\right) = -\frac{\dot{H}}{H^2}\,. \tag{2.4}$$

This system of equations is particularly useful to obtain fixed point solutions in the evolution of the scalar field.

2.1.1 Scaling freezing models

We first consider the case of a single exponential potential [57]:

$$U(\phi) = V\exp\left(-\lambda\frac{\phi}{M_P}\right)\,, \tag{2.5}$$

where V and λ are constant parameters. The density evolution of the scalar field is given by the system of equations (2.2). The fixed point solutions for the scalar field respect

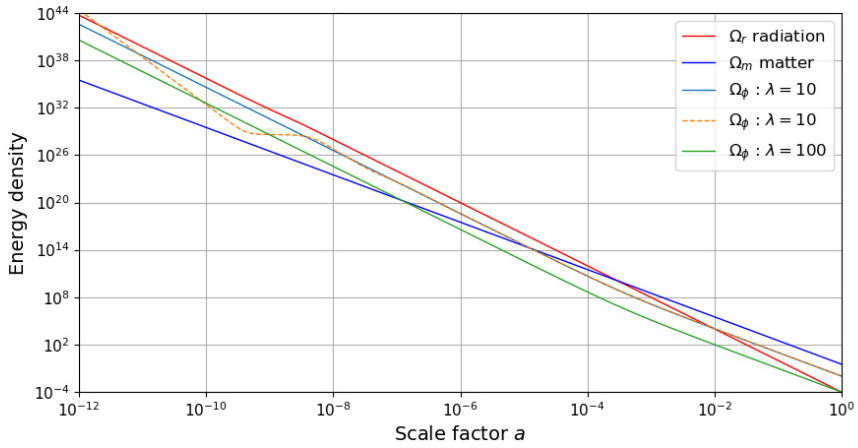

Figure 2.1 – Evolution of the scalar field density for a single exponential potential, as a function of the scale factor. The solid curves for the scalar field have been obtained for fixed point initial conditions and the dashed curve for arbitrary initial conditions. In the fixed point case, the evolution of the scalar field density follows the dominant energy density.

$x' = 0$ and $y' = 0$. In the case where the evolution of the Universe is dominated by a barotropic fluid with a pressure such as $P_f = (f-1)\rho_f$ where f is constant, we have:

$$\begin{aligned} x &= \frac{\dot{\phi}}{\sqrt{6}M_P H} = \sqrt{\frac{3}{2}}\frac{f}{\lambda}\,, \\ y &= \frac{\sqrt{U(\phi)}}{\sqrt{3}M_P H} = \left(\frac{3(2-f)f}{2\lambda^2}\right)^{1/2}\,, \end{aligned} \tag{2.6}$$

and the fixed point solutions are given by:

$$\frac{8\pi G}{3H^2}\left(\frac{\dot{\phi}^2}{2} + V\exp\left(-\lambda\frac{\phi}{M_P}\right)\right) = \frac{3f}{\lambda^2}\,. \tag{2.7}$$

These fixed point solutions are the only ones which are stable, as discussed in [57]. Therefore during the radiation-domination era we have:

$$\left(\frac{H}{H_0}\right)^2 \simeq \Omega_r^0 \quad \Longrightarrow \quad \Omega_\phi = \frac{\rho_\phi}{\rho^c} = \frac{4\Omega_r^0}{\lambda^2}a^{-4}\,, \tag{2.8}$$

and during the matter-domination era:

$$\frac{H^2}{H_0^2} \simeq \Omega_m^0 a^{-3} \quad \Longrightarrow \quad \Omega_\phi = \frac{\rho_\phi}{\rho^c} = \frac{3\Omega_m^0}{\lambda^2}a^{-3}\,, \tag{2.9}$$

where ρ^c is the critical density. Hence the evolution of the scalar field density will follow that of the dominating density. The evolution of the scalar field is shown as a function of

the scale factor in Figure 2.1. As expected, the scalar field density follows the evolution of the dominating density and is inversely proportional to λ^2 for fixed point solutions. For $\lambda = 10$, two curves are drawn, one with fixed point initial conditions and the other one for arbitrary initial conditions. In the latter case the scalar field is first dominated by its kinetic term and its density is proportional to a^{-6}, it then reaches a plateau whose height depends on the value of V and the initial values of ϕ and of $\dot{\phi}$. This kind of behaviour does not depend on the form of the potential and will be studied in more detail in the next section. Ultimately, the scalar field reaches the fixed point behaviour.

At the time of BBN ($a \sim 10^{-10}$), since the radiation is dominating, the scalar field density decreases with an exponent equal to $n_\phi = 4$ for fixed point solutions and $n_\phi = 6$ for other initial conditions.

The problem of the exponential potential however is that because of its tracking behaviour, it does not lead to a correct present-time behaviour with $w_\phi \approx -1$, and the single exponential potential is generally considered as excluded [58].

We therefore turn towards the more flexible double exponential potential [59], which is the prototypical scaling freezing model:

$$U(\phi) = V_1 \exp\left(-\lambda_1 \frac{\phi}{M_P}\right) + V_2 \exp\left(-\lambda_2 \frac{\phi}{M_P}\right), \tag{2.10}$$

where $V_{1,2}$ and $\lambda_{1,2}$ are constant parameters. Such a model can be motivated by compactifications in superstring models. The top panel of Figure 2.2 shows the evolution of the scalar field density for $\lambda_2 = 0$ and for different values of λ_1. The initial conditions have been chosen in order to obtain fixed point solutions. The bottom panel shows the evolution of the equation of state $w_\phi = P_\phi/\rho_\phi$. During the radiation-dominated era, we have $w_\phi = w_r = 1/3$. During the matter-dominated era we have $w_\phi = w_m = 0$. It is only recently that the second term in the potential (2.10) is dominating, leading to an equation of state $w_\phi \simeq -1$. In the $\lambda_2 = 0$ case, the observational constraint from Planck (1.39) at 95% C.L. translates into $\lambda_1 > 13$ at 95% C.L., and the observational constraint from early dark energy $\Omega_{EDE} \leq 1.3\%$ at $z = 1000$ translates into $\lambda_1 > 15$. Therefore a double exponential can explain the recent acceleration of the expansion of the Universe.

To summarize, within the model under consideration, at the epoch of BBN the scalar field has a radiation-like behaviour with $w_\phi = 1/3$ for fixed point solutions, whereas with generic initial conditions either the kinetic term dominates leading to $w_\phi = 1$, or the potential dominates leading to a plateau with $w_\phi = -1$.

2.1.2 Tracking freezing models

We now consider the inverse power-low potential [60]:

$$U(\phi) = M^4 \left(\frac{M_P}{\phi}\right)^p, \tag{2.11}$$

where M is a constant mass scale and p a positive exponent. Contrary to the exponential case, the potential is diverging when the scalar field becomes close to zero.

The top panel of Figure 2.3 shows the evolution of the scalar field density for two values of p and different initial conditions. In the early Universe, the scalar field is dominated

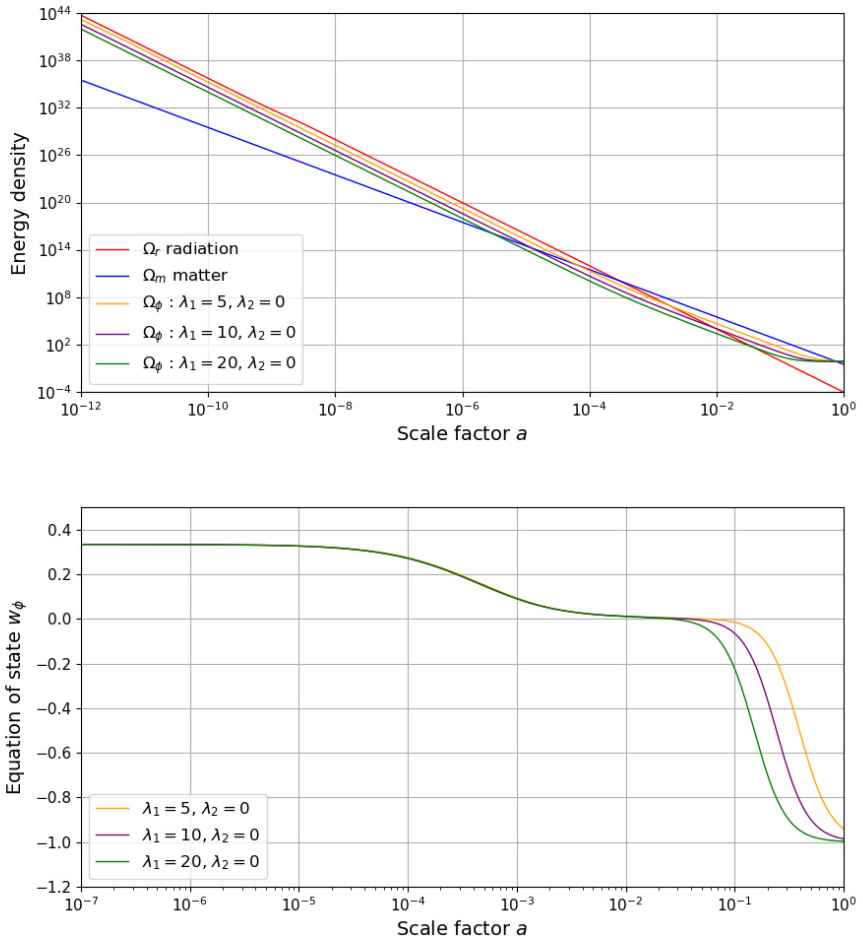

Figure 2.2 – Evolution of the scalar field in the scaling freezing model with a double exponential behaving like dark energy. V_1 and V_2 have been fixed to retrieve the cosmological constant value today. The top panel shows the evolution of its density, matter density and radiation density as functions of the scale factor. The bottom panel shows the evolution of the scalar field equation of state $w_\phi = P_\phi/\rho_\phi$ as a function of the scale factor. The curves have been drawn for different values of λ_1, and for $\lambda_2 = 0$.

by its kinetic energy and the equation of state is $w_\phi = 1$. After this period the scalar field density is constant with $w_\phi = -1$. As can be seen in the figure, the duration of the constant behaviour period strongly depends on initial values of the scalar field and can even extend to the present period, or stop and reach an intermediate equation of state with $\omega_\phi \sim -0.5$ with a negligible density. Finally the two curves (dashed and solid) for the same value of p are identical and determine the value of the dark energy density today and its equation of state. Following [41, 61], in the matter area we have $\omega_\phi = -2/(p+2)$. The Planck constraints (1.38) at 95% C.L. then translate into $p < 0.105$.

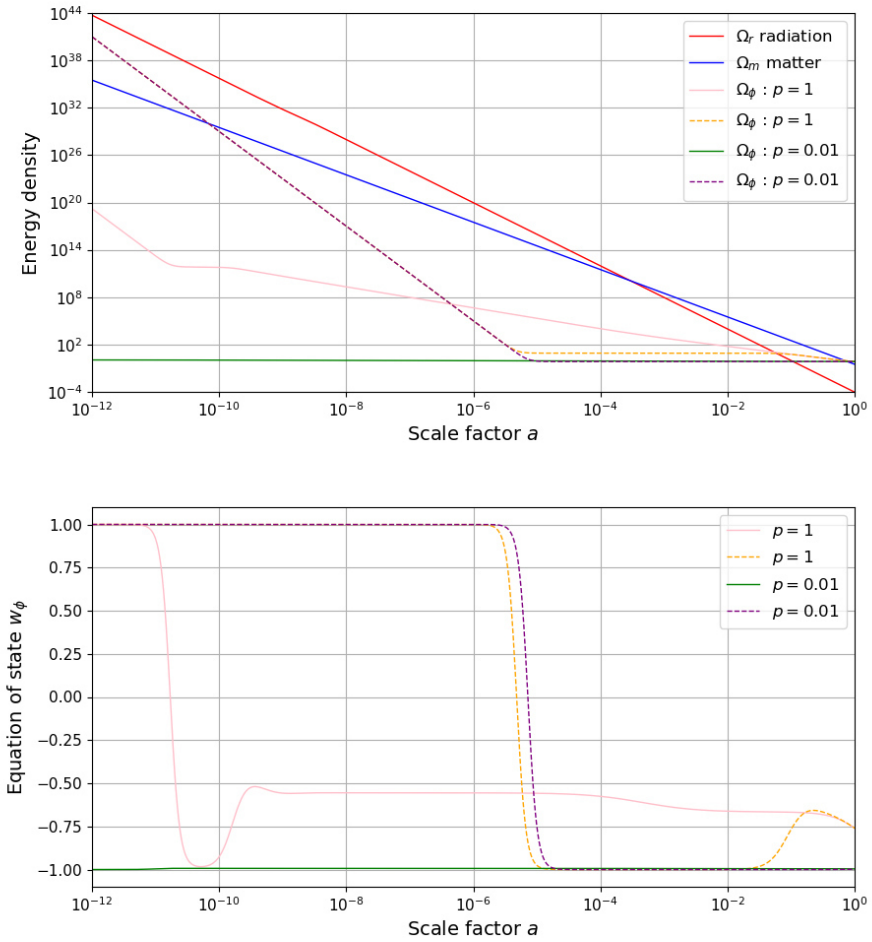

Figure 2.3 – Evolution of the scalar field in the tracking freezing model with inverse power-low potential behaving like dark energy. M has been fixed to retrieve the cosmological constant value today. The top panel shows the evolution of the scalar field, matter and radiation densities as functions of the scale factor. The bottom panel shows the evolution of the equation of state $w_\phi = P_\phi/\rho_\phi$ as a function of the scale factor. The curves are drawn for different values of the exponent p and for two different initial conditions.

To summarize, in this scenario we found that during BBN the scalar field can either be dominated by its kinetic term with $w_\phi = 1$, or have a negligible density.

2.1.3 Thawing models

We now consider the pseudo-Nambu-Goldstone potential [62]:

$$U(\phi) = \mu^4\Big(1 + \cos(\phi/f_a)\Big)\,, \tag{2.12}$$

where μ and f_a are constant parameters.

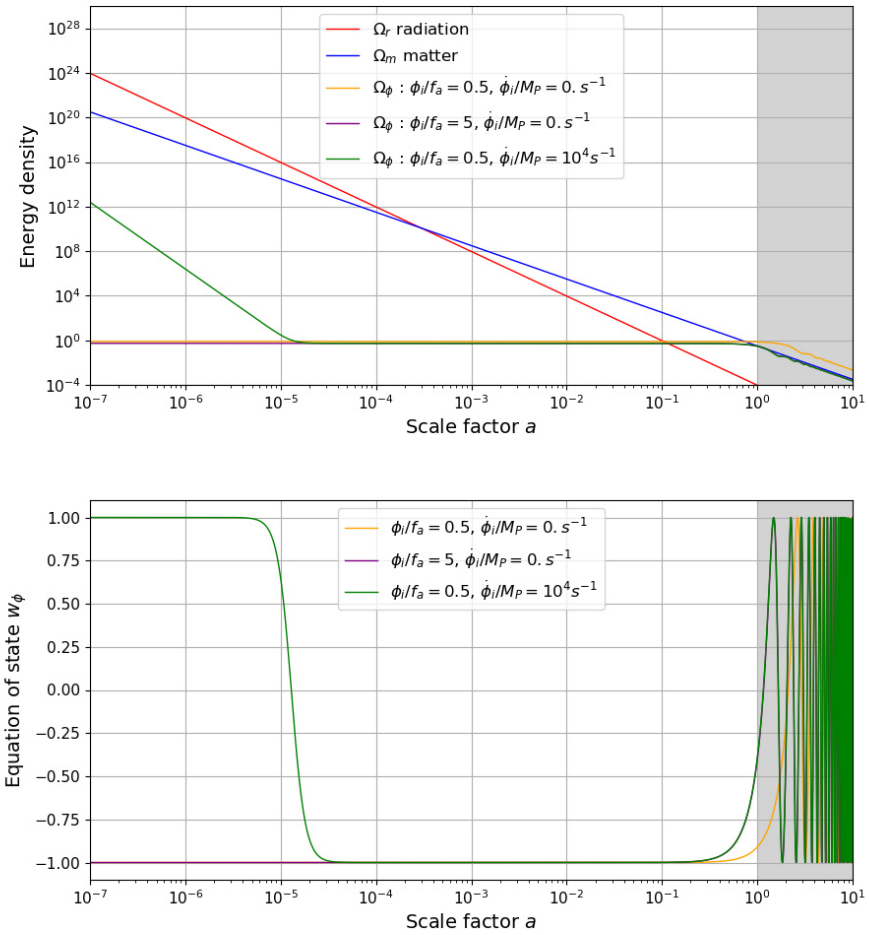

Figure 2.4 – Evolution of the scalar field in a thawing model with pseudo-Nambu-Goldstone potential behaving like dark energy, for different choices of initial conditions and parameters. μ has been fixed to retrieve the cosmological constant value today. The top panel shows the evolution of the scalar field, matter and radiation densities as functions of the scale factor. The bottom panel shows the evolution of the equation of state $w_\phi = P_\phi/\rho_\phi$ as a function of the scale factor. The curves are drawn up to $a = 10$ for different initial conditions. The shaded area corresponds to the future with $a > 1$.

Figure 2.4 shows the behaviour of the scalar field for different initial conditions and choices of μ and f_a, as a function of the scale factor. We explicitly plotted the evolution up to $a = 10$ in order to better visualize how the behaviour changes in the future when $a > 1$. If the initial value of $\dot{\phi}$ is non-zero, the scalar field is first dominated by its kinetic term. Then the scalar field becomes constant. At the present period, $a \approx 1$, the scalar field starts to evolve and w_ϕ increases and starts to oscillate. This behaviour is called "thawing" as opposed to the "freezing" behaviour of the previous models. For larger values of ϕ_i/M_P the field starts oscillating earlier. In the future for $a > 1$, which corresponds to

the shaded area in the figure, the averaged value of w_ϕ will stay close to 0, and the scalar field will therefore behave like matter. At the time of BBN, we observe that the scalar field is generally dominated by its kinetic term leading to $w_\phi = 1$, or has a constant but negligible density.

At the present epoch with $a \sim 1$ the equation of state departs from the cosmological constant behaviour. Using the Planck constraints from Eqs. (1.38) and (1.39), we obtain that $w_\phi < -0.95$ at 95% C.L. In Figure 2.4 this means that cases with $\dot{\phi} = 0$ (blue and green curves) are excluded.

To summarize, quintessence scalar fields at BBN time have generally three different behaviours:

- a dominating kinetic term leading to $w_\phi = 1$,
- a tracking radiation-like behaviour with $w_\phi = 1/3$,
- a constant behaviour with $w_\phi = -1$, which often corresponds to a negligible density.

Intermediate behaviours are still possible, but in our set-up they always correspond to negligible densities during BBN.

2.2 Dark matter scalar fields

In this section, we consider the case of a scalar field with a matter-like behaviour in the present Universe. We therefore have the cosmological constant density set to its observational value, and the cold dark matter density is replaced by the scalar field density. We thus expect the scalar field density to have the same density as the observed cold dark matter one in the period between recombination and today, and a matter-like behaviour corresponding to $w_\phi = 0$.

Two separate cases can occur. First, if the scalar field is associated to a large mass term, dark matter can then be composed of scalar particles. Second, if the mass is very small, the Compton wavelength is large, and the scalar field will have only large scale effects. We study only the latter case in the following.

Let us consider an oscillating scalar field, which has a behaviour similar to the one of a pseudo-Nambu-Goldstone potential in the future. If the timescale T of the studied phenomena is much longer than the oscillation period of typical frequency $\omega_{\rm eff}$, but much shorter than the conformal Hubble time $\mathcal{H}^{-1}$, *i.e.* $\mathcal{H}^{-1} \gg T \gg \omega_{\rm eff}$, the averaged equation of state reads [63]:

$$w_\phi = \frac{\langle P_\phi \rangle}{\langle \rho_\phi \rangle} = \frac{\langle \phi'^2/(2a^2) - U(\phi) \rangle}{\langle \phi'^2/(2a^2) + U(\phi) \rangle} = \frac{\langle U'(\phi)\phi - 2U(\phi) \rangle}{\langle U'(\phi)\phi + 2U(\phi) \rangle} + \mathcal{O}\left(\frac{\mathcal{H}}{\omega_{eff}}\right), \tag{2.13}$$

where the prime corresponds to the derivative with respect to the conformal time η, defined as $dt = a\, d\eta$, and $\langle ... \rangle$ the average over the time interval T. For example, if we take a power-law potential $U(\phi) = \lambda|\phi|^n/n$, we can show that $w_\phi \simeq (n-2)/(n+2)$. Then, the conservation of the stress-energy tensor $\rho'_\phi + 3(1+w_\phi)\mathcal{H}\rho_\phi = 0$ gives:

$$\langle \rho_\phi \rangle = \rho_0 a^{-3(1+w_\phi)} = \rho_0 a^{-6n/(n+2)}\,. \tag{2.14}$$

As a consequence, a quadratic term in the potential leads to a matter-like behaviour.

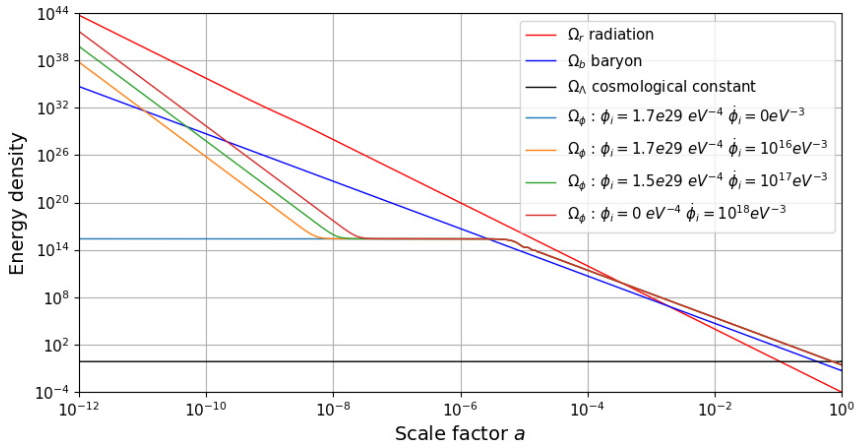

Figure 2.5 – Evolution of the fuzzy dark matter scalar field, associated to a quadratic potential with a mass $m = 10^{-24}$ eV, as a function of the scale factor. Baryon, radiation and cosmological constant densities follow the standard values of the ΛCDM model. The density of the scalar field has been calculated for different values of $\dot{\phi}$ at $a = 10^{-12}$. For each value of $\dot{\phi}$, we have chosen the initial value of ϕ in order to obtain a matter-like behaviour starting before the observed z_{eq} of Table 1.1 and a present scalar field density equal to the observed cold dark matter density.

2.2.1 Quadratic potential: fuzzy dark matter

Fuzzy dark matter [6] has recently attracted some attention [11] as a potential alternative to WIMP models. It features a quadratic potential such that:

$$U(\phi) = \frac{1}{2} m^2 \phi^2 \,. \tag{2.15}$$

As discussed before, such a potential can give to the scalar field a matter-like behaviour. Observations of galaxy rotation curves can be used to constrain the value of the mass m [37]. At galactic scales, the scalar field can be described as a Bose-Einstein condensate in gravitational interaction with baryonic matter, and a value of m compatible with the observations is of the order of $10^{-24} - 10^{-23}$ eV. The Klein-Gordon equation corresponding to the potential (2.15) in a homogeneous Universe reads [64]:

$$\ddot{\phi} + 3H\dot{\phi} + m^2\phi = 0 \,. \tag{2.16}$$

It is convenient to define the dimensionless time $\tilde{t} = mt$, the dimensionless Hubble constant $\tilde{H} = H/m$ and $u = a^{3/2}\phi$. With this change of variables, the Klein-Gordon equation takes the form:

$$\ddot{u} + \left(1 - \frac{3}{4}\frac{\dot{a}^2}{a^2} - \frac{3}{2}\frac{\ddot{a}}{a}\right) u = 0 \,. \tag{2.17}$$

Two cases can be considered:

- assuming $\tilde{H} \gg 1$, one can transform Eq. (2.17) into

$$v'' - \frac{a''}{a} v = 0\,, \tag{2.18}$$

with $' = d/d\eta$ the derivative with respect to the dimensionless conformal time η such as $d\eta = d\tilde{t}/a$, and $v = a^{-1/2}u = a\phi$. In the radiation-domination era, the Friedmann equation gives $a'' = 0$. We therefore find $d\eta \propto da$ and $v = \alpha_1 a + \beta_1$, where α_1 and β_1 are two constants of integration. The scalar field density reads:

$$\begin{aligned} \rho_\phi = \frac{\dot{\phi}^2}{2} + \frac{m^2\phi^2}{2} &= m^2 \left(\left(\frac{H_0\sqrt{\Omega_r^0}}{a} \frac{d}{da}\left(\frac{v}{a}\right) \right)^2 + \frac{1}{2}\left(\frac{v}{a}\right)^2 \right) \\ &= \frac{m^2 H_0^2 \Omega_r^0 \beta_1^2}{a^6} + \frac{m^2}{2}\left(\alpha_1 + \frac{\beta_1}{a}\right)^2 . \end{aligned} \tag{2.19}$$

- assuming $\tilde{H} \ll 1$ and $\dot{\tilde{H}} \ll 1$, the solution of Eq. (2.17) is much simpler. Indeed, the energy $E = \dot{u}^2/2 + u^2/2$ is conserved and we obtain

$$\rho_\phi = \frac{\dot{\phi}^2}{2} + \frac{m^2\phi^2}{2} = \frac{m^2 E}{a^3}\,. \tag{2.20}$$

Thus the background evolution of the scalar field gives a matter-like behaviour.

Figure 2.5 shows the evolution of the baryon, radiation, cosmological constant and scalar field densities for different initial conditions. In the early Universe the scalar field density is dominated by its kinetic energy and the potential is completely negligible. So $a^3 d\phi/dt$ is conserved and the scalar field density is proportional to a^{-6}. As $d\phi/dt$ decreases, at some point the field density becomes dominated by the potential and the field density is therefore constant as long as $H > m$. For $H < m$, the scalar field oscillates quickly and its energy density evolves like dark matter.

As discussed earlier, the end of the plateau corresponds to the equality $H^2 \simeq m^2$, or equivalently to $a \simeq (H_0^2\sqrt{\Omega_r^0}/m)^{1/4} \simeq 3.7 \times 10^{-6}$. The beginning of the plateau depends on the initial value of ϕ and is given by the solution of the equation:

$$\left(1 + \frac{H_0\sqrt{\Omega_r^0}\phi_i}{a_i^2\dot{\phi}_i}\right) a^3 - a_i a^2 - \frac{a_i H_0\sqrt{\Omega_r^0}}{m} = 0\,, \tag{2.21}$$

where the subscript i indicates the initial time. So the plateau begins before $a \simeq 2.4\times10^{-8}$, which corresponds to a negligible value of ϕ_i.

In conclusion, because of the plateau, the fuzzy dark matter scalar field density remains negligible during BBN.

2.2.2 Self-interaction coupling

We extend the previous analysis by adding a quartic term to the potential (2.15) [9,37]:

$$U(\phi) = \frac{1}{2}m^2\phi^2 + \frac{1}{4}\lambda\phi^4\,. \tag{2.22}$$

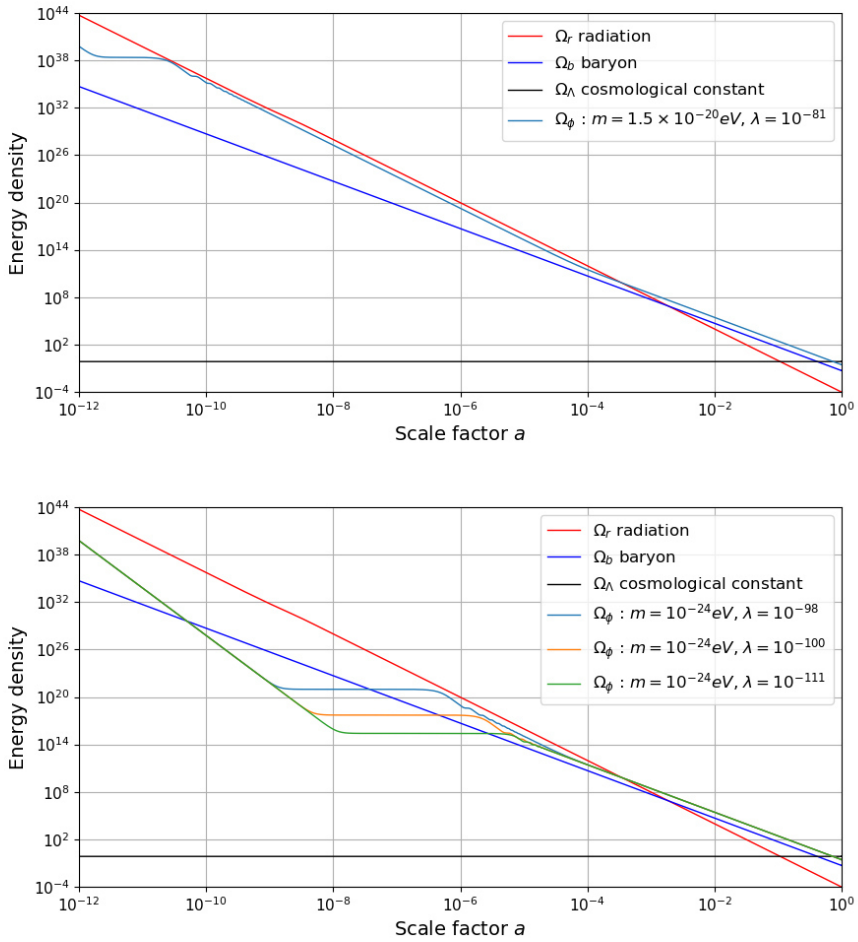

Figure 2.6 – Evolution of a scalar field with self-interaction coupling behaving like dark matter, as a function of the scale factor. Baryon, radiation and cosmological constant densities follow the standard values of the ΛCDM model. In the top panel the scalar field density is drawn with $m = 1.2 \times 10^{-20}$ eV, $\lambda = 10^{-81}$ and $\phi = 9.5 \times 10^{29}$ eV^{-4}, $\dot{\phi} = 1.3 \times 10^{17}$ eV^{-3} for $a = 10^{-12}$. In the bottom panel the scalar field density is drawn for different values of λ. For each value of $\dot{\phi}$, we have chosen the initial value of ϕ in order to obtain a matter-like behaviour starting before the observed z_{eq} of Table 1.1 and a present scalar field density equal to the observed cold dark matter density.

The dimensionless constant λ represents a self-interaction coupling. With the same notation as in the previous subsection, the Klein-Gordon equation becomes:

$$v'' + \left(a^2 - \frac{a''}{a} + \frac{\lambda}{m^2}v^2\right) v = 0\,. \tag{2.23}$$

Three different cases can be considered:

- assuming $\lambda\phi^2 \ll H^2$ and $\tilde{H} \gg 1$, the Klein-Gordon equation is the same as Eq. (2.18) and we obtain similar results.

- assuming $\lambda\phi^2 \gg H^2$ and $\lambda\phi^2 \gg m^2$, during the radiation-domination era, the Klein-Gordon equation becomes:
$$v'' + \frac{\lambda}{m^2} v^3 = 0\,. \tag{2.24}$$
In this case the quadratic part of potential does not contribute to the evolution of field density. The energy $E = v'^2/2 + \lambda v^4/(m^2)$ is conserved and we obtain:
$$\rho_\phi = \frac{\dot{\phi}^2}{2} + \frac{\lambda\phi^4}{4} = \frac{m^2 E}{a^4} + \frac{m^2 u}{2a^4}\left(\frac{H_0^2\Omega_r^0}{a^2} v - \frac{2H_0\sqrt{\Omega_r^0}}{a} v'\right)\,. \tag{2.25}$$
Therefore the background behaviour of the scalar field is radiation-like.
- assuming $\lambda\phi^2 \ll m^2$ and $\tilde{H} \ll 1$, $\dot{\tilde{H}} \ll 1$, the Klein-Gordon equation is the same as in Eq. (2.17) and we obtain similar results.

Figure 2.6 shows the evolution of the baryon, radiation, cosmological constant and scalar field densities. As expected the difference with the results of the previous subsection is a radiation-like behaviour of the scalar field. In the top panel, we have chosen a mass $m = 1.2 \times 10^{-20}$ eV, and we see that the scalar field density is not negligible during BBN and its evolution is dominated by the self-interaction coupling. Such a mass is however disfavoured by the CMB and large-scale structure data, which impose [11]:

$$\begin{aligned} &10^{-26} < m/\text{eV} < 10^{-23.3}\,, \\ &10^{-111} < \lambda < 10^{-98}\,. \end{aligned} \tag{2.26}$$

In the bottom panel of Figure 2.6, we have chosen parameter values compatible with these constraints, and we see that the scalar field density is negligible during BBN. More generally, scanning over the parameters and imposing the constraints (2.26), we have verified that the scalar field density is always negligible at the BBN epoch.

2.2.3 Polynomial potential

The previous results can be extended to the case of an arbitrary polynomial potential. The BBN constraints then depend on which term of the potential is dominating at BBN time. Following Eq. (2.42), if the dominating term is ϕ^n, the scalar field density evolves as $\rho_\phi \propto a^{-6n/(n+2)}$, meaning that the exponent is within the range $[-6, 0]$. For example, if the dominating term is ϕ^6, Eq. (2.42) gives $\rho_\phi \propto a^{-4.5}$. However, since the matter-like behaviour should hold at recombination time, it can be expected that the scalar field density is also negligible at BBN time.

2.2.4 Exponential potential

We now consider the following potential:

$$U(\phi) = \alpha\rho^c \left[\exp\left(\frac{\beta\phi^2}{m^2}\right) - 1\right]\,, \tag{2.27}$$

where ρ^c is the critical density, and α and β are two dimensionless constants. This potential is built in order to have a minimum at zero in absence of scalar field. Similarly to

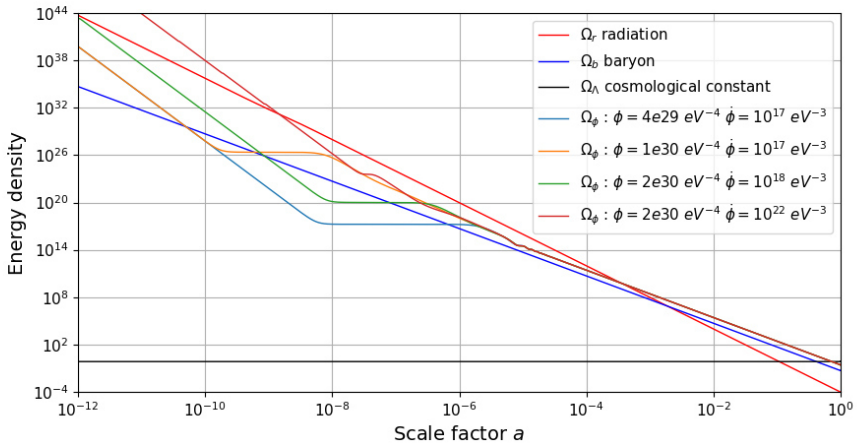

Figure 2.7 – Evolution of a scalar field with an exponential potential behaving like dark matter, as a function of the scale factor. Baryon, radiation and cosmological constant densities follow the standard values of the ΛCDM model. The scalar field density has been calculated for different initial values. For each value of $\dot{\phi}$, we have chosen α in order to obtain a matter-like behaviour starting before the observed z_{eq} of Table 1.1 and a present scalar field density equal to the observed cold dark matter density.

the previous cases, the scalar field is required to start behaving like dark matter before recombination in order to agree with the CMB data. In the late Universe, the scalar field is expected to have a small value, so that the potential becomes via a Taylor expansion:

$$U(\phi) = \rho^c \left(\frac{\alpha\beta}{m^2}\phi^2 + \frac{1}{2}\frac{\alpha\beta^2}{m^4}\phi^4 + ... \right) , \tag{2.28}$$

where the dominant term is quadratic. We therefore recover the fuzzy dark matter potential with possibly a non-negligible quartic term. Constraints on fuzzy dark matter impose the mass of the scalar field to be around 10^{-24} eV. In consequence we choose $2\alpha\beta = m^4/\rho^c$. With this relation there is only one free parameter for this potential. Figure 2.7 shows the scalar field density evolution for different initial conditions. For each initial scalar field value we have chosen α to obtain the same value of the radiation-matter equality as in the ΛCDM scenario, so that $\alpha \simeq 5 \times 10^{15}$. We found that with an exponential potential, only two behaviours are possible during BBN: either a kinetic term domination with $w_\phi = 1$, or a potential term domination leading to a constant density with $w_\phi = -1$.

2.2.5 Complex scalar field: Spintessence

Until now we have only considered the case of a real scalar field. In this subsection we study a complex scalar field with a $U(1)$-symmetric potential [47]. The potential will be given by $U(\phi^\dagger\phi)$. For a complex scalar field:

$$\phi(t) = \frac{\sigma(t)}{\sqrt{2}} \exp(i\theta(t)) , \tag{2.29}$$

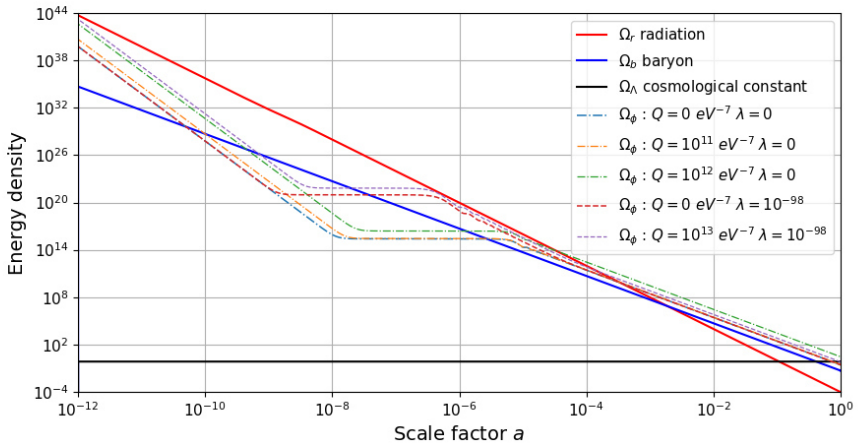

Figure 2.8 – Evolution of a spintessence complex scalar field with a mass term behaving like dark matter, as a function of the scale factor. Baryon, radiation and cosmological constant densities follow the standard values of the ΛCDM model. We have chosen $\dot{\phi} = 1.3 \times 10^{17}$ eV^{-3} for $a = 10^{-12}$, and we set the initial value of ϕ in order to obtain a matter-like behaviour starting before the observed z_{eq} of Table 1.1 and a present scalar field density equal to the observed cold dark matter density.

where $\sigma(t)$ is the amplitude and $\theta(t)$ the phase, Friedmann and Klein-Gordon equations give the following system:

$$\begin{aligned} &\frac{d^2\sigma}{dt^2} + 3H\frac{d\sigma}{dt} + U'\left(\frac{\sigma^2}{2}\right)\sigma - \omega^2\sigma = 0\,, \\ &\frac{d\omega}{dt}\sigma + 3H\omega\sigma + 2\omega\frac{d\sigma}{dt} = 0\,, \\ &H^2 = H_0^2\left(\Omega_b^0 a^{-3} + \Omega_r^0 a^{-4} + \frac{\rho_\phi}{\rho^c}\right)\,, \end{aligned} \tag{2.30}$$

with $\omega(t) = d\theta/dt$ and

$$\rho_\phi = \frac{\dot{\sigma}^2}{2} + \frac{\omega^2\sigma^2}{2} + U\left(\frac{\sigma^2}{2}\right)\,. \tag{2.31}$$

The first two terms of the density constitute the kinetic part. The second line of Eq. (2.30) is the imaginary part of the Klein-Gordon equation and implies the conservation of the U(1)–charge per comoving volume $Q = \omega\sigma^2 a^3$. We can rewrite the first equation and the scalar field density as:

$$\begin{aligned} &\frac{d^2\sigma}{dt^2} + 3H\frac{d\sigma}{dt} + U'\left(\frac{\sigma^2}{2}\right)\sigma - \frac{Q^2}{\sigma^3 a^6} = 0\,, \\ &\rho_\phi = \frac{\dot{\sigma}^2}{2} + \frac{Q^2}{2\sigma^2 a^6} + U\left(\frac{\sigma^2}{2}\right)\,. \end{aligned} \tag{2.32}$$

We consider now the evolution of the scalar field density for a polynomial potential of order 4:

$$U(\phi^\dagger\phi) = U_0 + m^2\phi^\dagger\phi + \lambda(\phi^\dagger\phi)^2 = \frac{1}{2}m^2\sigma^2 + \frac{1}{4}\lambda\sigma^4\,. \tag{2.33}$$

Figure 2.8 shows the evolution of the scalar field density for different values of the charge per comoving volume Q as a function of the scale factor. We consider first the case where the self-coupling λ is zero. When Q is zero we recover exactly the results of a real scalar field. In the early Universe, when Q increases the Klein-Gordon equation gives the conservation of $a^3 d\sigma/dt$. At this time, the kinetic terms which depend on the values of $\dot{\sigma}^2$ and Q^2 dominates, giving an equation of state $w_\phi = 1$. The behaviour then changes and the density becomes constant. We can see that the height of the plateau increases with the charge per comoving volume. The transition between the plateau and the dark matter behaviour, which is given by $H \simeq m$ for $Q = 0$, will also increase. In conclusion, the second term in Eq. (2.31) acts as an extra mass term and the evolution of the complex scalar field density has the same behaviour as a real scalar field. Similar conclusions are obtained for a non-zero self-coupling, and the scalar field has a negligible density at the time of BBN.

To summarize, the density of dark matter scalar fields is generally dominated by the kinetic part at the epoch of BBN, leading to an equation of state $w_\phi = 1$ and an evolution such that $\rho_\phi \propto a^{-6}$. However, the density of the scalar field is generally negligible at this time. We also saw that non-standard potentials such as polynomials can lead to other behaviours. It is however important to keep in mind that a scalar field with a heavy mass term can behave like dark matter even during the BBN epoch, having an average equation of state $w_\phi = 0$ and an evolution such that $\rho_\phi \propto a^{-3}$.

2.3 Dark fluid model

A scalar field which interacts only gravitationally with baryonic matter associated to a dominating quadratic mass term in the potential can behave as collisionless matter and be a dark matter candidate. One the other hand a scalar field with a mostly constant potential can explain the current acceleration of the expansion of the Universe. As discussed in Refs. [49–51] it is possible to explain the dark energy and dark matter behaviours with a unique dark fluid. We study the properties of such a scalar field in view of the observational constraints.

2.3.1 Dark fluid model and observational constraints

Galactic scale: Fuzzy Dark Matter

Most of the dark matter models involve particles which interact only very weakly with Standard Model particles. Such weakly-interacting massive particles (WIMPs) are still undiscovered at colliders and in dark matter detection experiments. An alternative possibility based on scalar fields, namely fuzzy dark matter [6], has recently re-attracted some attention [48]. At galactic scale such models can reproduce the flatness of galaxy rotation curves [37]. The scalar field, associated to a quadratic potential with a mass m, can

form a Bose-Einstein condensate in gravitational interactions with baryonic matter. The condensate constitutes a galactic halo with a typical size given by the Compton wavelength:

$$l_{\text{compton}} = \frac{h}{mc}\,. \tag{2.34}$$

For a typical halo of 10 kpc, the mass m is estimated to be $m \sim 10^{-23}$ eV [52]. Having such a small mass is an advantage for fuzzy dark matter since it does not suffer from the so-called cuspy halo and missing satellite problems [65]. Furthermore a scalar field with in addition to a mass term a quartic term of coupling constant λ, can also condensate within a radius L, which can be of the order of the typical size of a cluster. The relation between L and λ is given by:

$$\lambda = \frac{8\pi G m^4 L^2}{c^2}\,. \tag{2.35}$$

For a typical cluster size $L \sim 1$ Mpc, the value of the quartic term coupling is $\lambda \sim 10^{-89}$ [52].

The fuzzy dark matter model has been studied in the context of galactic halos, in particular in Refs. [6,65]. The evolution of an ultralight scalar field ϕ is given by the Klein-Gordon equation. In a static galaxy gravitational interaction can be globally described in the Newtonian limit with the Poisson equation. In addition, a nonrelativistic dispersion relation can be safely assumed for the wave equation. The wavefunction of the scalar field can be written under the form $\psi = A\exp(i\alpha)$, where A is the probability amplitude and α the phase, so that $\phi = A\cos(mt-\alpha)$ [6]. The evolution equation reads:

$$i\left(\partial_t + \frac{3}{2}\frac{\dot{a}}{a}\right)\psi = \left(-\frac{1}{2m}\nabla^2 + m\Psi\right)\psi\,, \tag{2.36}$$

and the Poisson equation:

$$\nabla^2\Psi = 4\pi G\delta\rho_\phi\,, \tag{2.37}$$

where Ψ is the Newtonian potential, $\dot{a}/a$ is the Hubble parameter and $\delta\rho_\phi = m^2\delta|\psi|^2/2$ is the energy density of the scalar field. Equation (2.36) is the Schrödinger equation for a self-gravitating particle in a Newtonian potential in an expanding Universe. In Ref. [6] it is shown that ultralight particles with a mass $m \sim 10^{-22}$ eV lead to smooth and minimum-sized halos, and therefore provide a solution to the cuspy halo and galaxy satellite problems of standard cold dark matter scenarios.

The Schrödinger-Poisson equation system (2.36-2.37) also describes a solitonic behaviour during a head-on collision between two galaxies with Bose-Einstein condensate halos [66], that is compatible with the observations of the Bullet Cluster [67].

Galaxy rotation curves in agreement with the observations can also be obtained with an ultralight complex scalar field, when a stationary and regular configuration is assumed, with the harmonic ansatz:

$$\phi(r,t) = \phi_0(r)\exp(i\omega t)\,, \tag{2.38}$$

similar to the one of boson stars. A comprehensive study in general relativity has been presented in [37], finding a best fit to the galaxy rotation curves with a mass in the range 10^{-24}–10^{-23} eV. This result is similar to the one obtained in the Newtonian approximation.

Cosmological behaviour

Let us now consider the cosmological behaviour of the dark fluid scalar field. We assume a homogeneous Universe filled only with radiation, baryonic matter and dark fluid scalar field. Using the Friedmann-Lemaître-Robertson-Walker (FLRW) metric, the Einstein and Klein-Gordon equations become:

$$\begin{aligned} H^2 &= \frac{8\pi G}{3}\left(\rho_\phi + \rho_r + \rho_b\right) , \\ 2\dot{H} + 3H^2 &= -8\pi G\left(P_\phi + P_r + P_b\right) , \\ \ddot{\phi} + 3H\dot{\phi} + \frac{dV}{d\phi} &= 0 , \end{aligned} \tag{2.39}$$

where the energy density and pressure of the scalar field are given by:

$$\begin{aligned} \rho_\phi &= \frac{1}{2}\left(\frac{d\phi}{dt}\right)^2 + V(\phi) , \\ P_\phi &= \frac{1}{2}\left(\frac{d\phi}{dt}\right)^2 - V(\phi) . \end{aligned} \tag{2.40}$$

If we consider the cosmological evolution of a rapidly oscillating scalar field with a frequency $f_{\rm eff}$. The oscillations need to be faster than the Universe evolution, which is characterized by the conformal Hubble time $\mathcal{H}^{-1}$. For example for the power-law potential $V(\phi) = \lambda|\phi|^n/n$, the average equation of state is given by:

$$w_\phi = \frac{\langle P_\phi \rangle}{\langle \rho_\phi \rangle} = \frac{n-2}{n+2} , \tag{2.41}$$

where $\langle ... \rangle$ denotes the average value over a time T such that $\mathcal{H}^{-1} \gg T \gg f_{\rm eff}^{-1}$. When the potential governs the energy density evolution, the conservation of the stress energy tensor gives:

$$\langle \rho_\phi \rangle = \rho_{\phi,0}\left(\frac{a}{a_0}\right)^{-3(1+w_\phi)} = \rho_{\phi,0}\left(\frac{a}{a_0}\right)^{-6n/(n+2)} . \tag{2.42}$$

For $n = 2$, this energy density evolves like cold dark matter.

During the period when radiation is dominating the expansion, we can derive constraints from primordial nucleosynthesis (BBN). At this epoch the evolution of the scalar field density is governed by its kinetic term and BBN constraints exclude large scalar field densities such as [17]:

$$\rho_\phi(1\text{ MeV}) \geq 1.40\rho_\gamma(1\text{ MeV}) . \tag{2.43}$$

The CMB and large scale structure observations provide additional constraints. Considering a scalar field with anharmonic corrections and a potential with a quadratic term with a mass m and a quartic term with a small coupling constant λ, the main constraints provided by the Planck and WiggleZ data are [11]:

$$\log_{10}(\lambda) < -91.86 + 4\log_{10}\left(\frac{m}{10^{-22}\text{ eV}}\right) \tag{2.44}$$

for masses heavier than 10^{-24} eV.

The acceleration of the expansion of the recent Universe can be in agreement with a simple cosmological constant. On the other hand quintessence models describe dark energy with a scalar field ϕ which has a constant density today and was negligible during the matter and radiation domination periods.To have a dark energy behaviour, the dark fluid scalar field therefore needs to have in the recent Universe a rather constant density, corresponding to a nearly constant value of ϕ.

Simple dark fluid potential

The dark fluid potential is an open question. In the recent Universe, when the energy densities are low, the values of the scalar field are small, and one can consider a series expansion of the potential, assuming a Z_2 symmetry. Limiting ourselves to the second order, the simplest potential mimicking dark matter and dark energy appears as a second order polynomial, *i.e.* the sum of constant, having the role of cosmological constant, and a quadratic term equivalent to the fuzzy dark matter potential. Anharmonic corrections can also occur with one extra order in the polynomial expansion, and the expanded effective potential then reads

$$V(\phi) = V_0 + \frac{1}{2}m^2\phi^2 + \frac{1}{4}\lambda\phi^4\,. \tag{2.45}$$

The constant V_0 can lead to a dark energy behaviour provided:

$$V_0 = \frac{\Lambda c^4}{8\pi G} \approx 2.5 \times 10^{-11}\ \mathrm{eV}^4\,, \tag{2.46}$$

where Λ is the cosmological constant. The mass term behaves as a cold and fuzzy dark matter if m is in the range:

$$m \approx 10^{-22} - 10^{-21}\ \mathrm{eV}\,, \tag{2.47}$$

and the quartic term λ must verified the inequality (2.44).

Figure 2.9 shows the evolution of the scalar field energy density fraction $\Omega_\phi = \rho_\phi/\rho^0_{cr}$ with $\rho^0_{cr} = 3H_0^2/(8\pi G)$ the critical density as a function of the scale factor a in a homogeneous Universe described by the system of equations (2.39). More precisely the Universe is considered flat and composed of:

- radiation which evolves according to a^{-4},
- baryonic matter which evolves according to a^{-3},
- dark fluid which evolves like matter as a^{-3} when the mass term governs the scalar field evolution and like dark energy when the constant term dominates.

In the early Universe, the scalar field evolution is dominated by the kinetic term $\dot{\phi}^2/2$ and its density evolves according to a^{-6}. After this period the potential can start dominating, resulting in a constant density. Then an equilibrium between the kinetic and the potential is reached, leading to a density described by the equation (2.42). When $m^2 \ll \lambda\phi^2$ and $V_0 \ll \lambda\phi^4$, its density evolves like radiation. When $\lambda\phi^2 \ll m^2$ and $V_0 \ll m^2\phi^2$, its density evolves like matter and when $\lambda\phi^4 \ll V_0$ and $m^2\phi^2 \ll V_0$, its density evolves like cosmological constant. Essentially the value of the constant density plateau depends on on the mass m, that we fix to 10^{-22} eV, the initial value of ϕ and the quartic term. The dependence on λ is also shown in Figure 2.9 for a quadratic potential with anharmonic

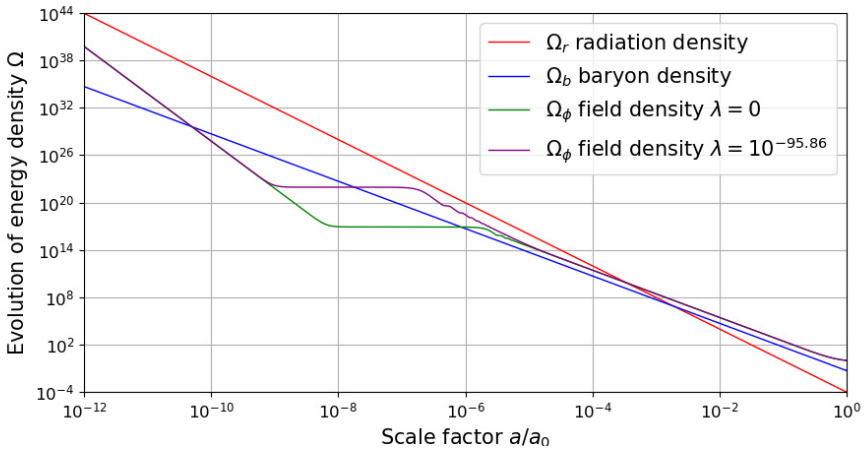

Figure 2.9 – Evolution of dark fluid scalar field density fraction as a function of the scale factor a in the case of a potential with constant term, quadratic term with mass $m = 10^{-22}$ eV, and quartic term with coupling constant λ. Baryon and radiation densities follow those of the ΛCDM model.

corrections, where the initial conditions have been chosen in order to have the same scalar field in the recent Universe.

Within this setup, the dark fluid can replace simultaneously dark matter and dark energy. It is however important to keep in mind that the potential (2.45) may be a series expansion of a more complicated potential. In such a case, the primordial properties of the scalar may be affected by the real form of the potential.

2.3.2 General potential for the dark fluid model

A possibility to improve the dark fluid model is to replace the constant part of the potential by a dynamical term. Practically it has to be negligible during the matter domination era in order not to affect the dark matter behaviour. One can for example add to the quadratic term a quintessence potential [8, 55], replace the quadratic term [52], consider quantum corrections [53], etc. We will see in the following which potentials can explain simultaneously dark energy and dark matter.

Extended dark matter term

Let us consider the case of an exponential potential. By construction:

$$V(\phi) = V_0 \exp\left(\frac{m^2}{2V_0}\phi^2\right) \underset{\phi\to 0}{\simeq} V_0 + \frac{1}{2}m^2\phi^2 + \frac{m^4}{4V_0}\phi^4\,, \tag{2.48}$$

where the second equality is the series expansion, which is valid for small ϕ values. V_0 is fixed to the cosmological constant value $V_0 = 2.5 \times 10^{-11}$ eV, and $m \sim 10^{-22}$ eV as

explained in the previous section, so that the effective quartic term coupling is

$$\lambda = \frac{m^4}{V_0} \simeq 10^{-78} \,. \tag{2.49}$$

Unfortunately this value is too large and is not compatible with the CMB constraints given in Eq. (2.44).

A second possibility is the following potential:

$$V(\phi) = V_0 + \frac{m^4}{\lambda}\left[\exp\left(\frac{\lambda\phi^2}{2m^2}\right) - 1\right] \underset{\phi\to 0}{\simeq} V_0 + \frac{1}{2}m^2\phi^2 + \frac{1}{4}\lambda\phi^4 \,, \tag{2.50}$$

which has the same behaviour as the polynomial dark fluid model presented in the previous section.

Another possibility is a potential with a hyperbolic sine:

$$V(\phi) = V_0 + \frac{m^4}{\beta}\sinh\left(\frac{\beta\phi^2}{2m^2}\right) \underset{\phi\to 0}{\simeq} V_0 + \frac{1}{2}m^2\phi^2 + \frac{1}{4!}\frac{\beta^2}{m^2}\phi^6 \,. \tag{2.51}$$

When ϕ is small, there is no quartic term and the ϕ^6 term will have a negligible effect, so that this potential reduces to a constant and a quadratic term.

These models have similar behaviours, which correspond to the one of a polynomial potential. In practice the main difference between them is the position of the constant density plateau, as explained in [17]. After the plateau, the scalar field behaves as dark matter and/or as dark energy, and these models are indistinguishable.

Extended dark energy term

We consider the case in which a quintessence term is added to the dark fluid potential. There exist two main classes of quintessence models [55]: freezing models in which the field follows a tracker potential down to its minimum, and thawing models in which the field continues evolving after reaching the dark energy behaviour.

To have a dark fluid model it is necessary for the quintessence term not to modify the dark matter behaviour. For example the tracking freezing potential [60]

$$V(\phi) = M^4\left(\frac{M_P}{\phi}\right)^p \tag{2.52}$$

is incompatible with the mass term. Indeed if the scalar field oscillates with a density evolving as a^{-3}, the field ϕ will sooner or later reach a negligible value and the tracking freezing potential diverges.

We now consider the expansion of an exponential potential:

$$V(\phi) = \frac{1}{2}m^2\phi^2 + \alpha\exp\left(-\frac{\beta}{2}\phi^2\right) \underset{\phi\to 0}{\simeq} \alpha + \frac{1}{2}(m^2 - \alpha\beta)\phi^2 + \frac{\alpha\beta^2}{4}\phi^4 \,, \tag{2.53}$$

where α is determined by the dark energy density, and m and β by the galactic and cluster scales, respectively. The exponential term can therefore explain simultaneously the

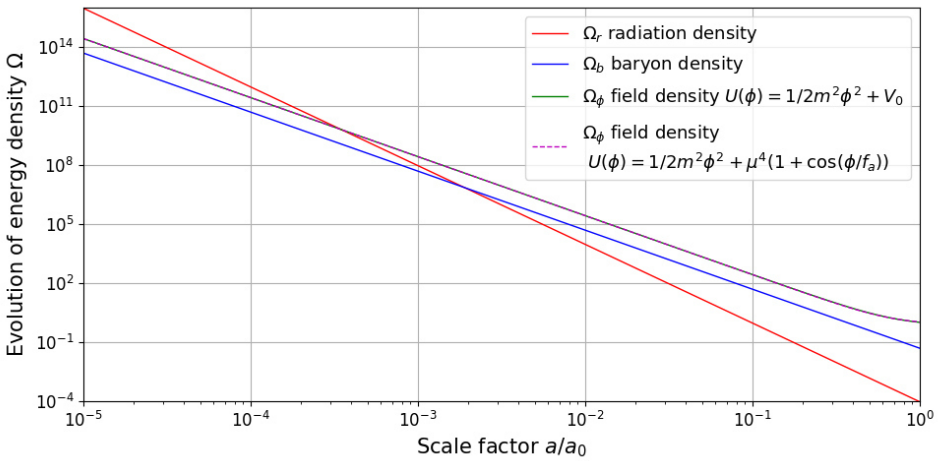

Figure 2.10 – Evolution of the dark fluid density for the simple dark fluid potential (solid green line) and for the pseudo-Nambu-Goldstone potential (dashed purple line) with mass $m = 10^{-22}$ eV. Both curves are superimposed with negligible differences. The evolutions of the baryon density and radiation density are the same as in the ΛCDM model, and are shown in red and blue, respectively.

acceleration of the expansion, galaxy rotation curves and galaxy cluster scale. Numerically, the modification of the mass term by the $\alpha\beta$ term is tiny.

Another possibility is the addition of a pseudo-Nambu-Goldstone potential [62]:

$$V(\phi) = \frac{1}{2}m^2\phi^2 + \mu^4\left(1 + \cos(\phi/f_a)\right) , \tag{2.54}$$

where m, μ and f_a are constant parameters. In this thawing model the dark energy behaviour which presently dominates the evolution of the Universe will end in the future and a new period of dark matter domination will happen in the far future. In Figure 2.10, the density evolution of the scalar field governed with the pseudo-Nambu-Goldstone potential with mass term is the same as with the simple dark fluid potential defined in Eq. (2.45).

The dark fluid model can also be generalized to a complex scalar field with a $U(1)$ symmetric potential. The dark matter behaviour is based on the spintessence model [47]. The symmetry implies the conservation of a charge per comoving volume: $Q = R^2\dot{\theta}a^3$ where R and θ are the amplitude and phase of the complex scalar field such as $\phi = R\exp(i\theta)$. However, similarly to all the dark fluid models that we presented, the choice of the potential remains arbitrary. The crucial point for a successful model seems to be that the dark fluid needs to have a fuzzy dark matter behaviour, or in other words its potential should contain a mass term with $m \sim 10^{-22}$ eV.

3

Triple unification

In this chapter, we show that it is possible for a scalar field to simultaneously replace dark matter, dark energy and inflation by assuming the existence of a non-minimal coupling to gravity, a Mexican hat potential, and a spontaneous symmetry breaking before inflation. After inflation, the scalar field behaves like a dark fluid, mimicking dark energy and dark matter, and has a dark matter behavior similar to fuzzy dark matter.

Contents

3.1 Introduction

The scalar fields are ubiquitous in cosmology, even if only one exists in the Standard Model of particle physics. One possibility to reduce the number of cosmological scalar fields is to unify dark energy and fuzzy dark matter using a single scalar field. This so-called dark fluid scalar field has already been considered in Refs. [50, 51] and is a possible solution to both dark energy and dark matter questions. However, such a model is not unique and the choice of the scalar field potential [52, 54] remains unclear. Nevertheless most of the potentials that have been considered in the literature can be approximated by the sum of a quadratic mass term leading to a matter behaviour and an approximately

constant term giving a dark energy behaviour. A second possibility is to unify inflation and dark energy [68]. In this case the simplest model is based on a potential composed of a mass term and a constant term which leads to two stages of accelerated expansion: The first accelerated expansion occurs in the early Universe and the second one at the present epoch. A third possibility is to unify inflation and dark matter. In such a case the chaotic inflation scalar field does not decay completely during reheating, and the density surviving the incomplete decay can behave as dark matter [69].

A step further would consist in a triple unification to explain simultaneously dark matter, dark energy and inflation with a unique scalar field. Such a scenario was for example studied in Refs. [70, 71] where the standard chaotic inflation scalar field with a mass $m \sim 10^{-6} M_P$ survives after an incomplete decay. The key feature of this scenario is that the scalar field density remains negligible during the radiation-domination era and oscillate around a non zero-minimum after radiation domination. Another model studied in Ref. [72] relies on a non-canonical kinetic term.

In the following we present a more natural triple unification scenario based on a cosmological scalar field undergoing a symmetry breaking before inflation. The inflationary period will be similar to Starobinsky inflation [28], and the resulting scalar perturbations in the new vacuum will behave as a dark fluid, unifying dark matter and dark energy. We restrict our study to cases where the dark fluid potential is a polynomial of order 4.

3.2 Model with a non-minimal coupling $\phi^2 R^2$

As mentioned in Appendix 3.6.1, a scenario with a polynomial potential without a non-minimal coupling between the scalar field and the gravity is incompatible with the CMB data and the fuzzy dark matter constraints derived in the previous section. A possible scenario to combine inflation and dark fluid using a scalar field ϕ is to add a non-minimal gravitational coupling to gravity. It is demonstrated in Appendix 3.6.2 that a $\phi^2 R$ term cannot be produced a correct inflationary period with a dark fluid potential. Assuming a Z_2 symmetry for the scalar field which will be spontaneous broken and considering a second order coupling in R, we consider the following action:

$$\mathcal{S} = \int d^4x\sqrt{-g}\left[\frac{1}{2\tilde{\kappa}^2}\left(R + \alpha\phi^2 R + \beta\phi^2 R^2\right) - \frac{1}{2}g^{\mu\nu}\partial_\mu\phi\partial_\nu\phi - V(\phi)\right], \tag{3.1}$$

where V is the dark fluid potential and $\tilde{\kappa}$ is a modified Einstein's gravitational constant which will give the usual κ constant after the symmetry breaking, and α, β two constants. In this model inflation will occur when the $\beta\phi^2 R^2$ term drives the expansion. Our goal is to retrieve the Starobinsky inflation model [28]. Before discussing the properties of the action (3.1), we briefly review the Starobinsky model, which is a specific case of $f(R)$ theories [73], in which the geometrical action reads

$$\mathcal{S} = \int d^4x\sqrt{-g}\frac{1}{2\kappa^2}f(R)\,, \tag{3.2}$$

with

$$f(R) = R + \frac{R^2}{6M^2}\,, \tag{3.3}$$

where M is a mass parameter. In the FLRW metric the Einstein equations lead to:

$$\begin{aligned} &\ddot{H} - \frac{\dot{H}^2}{2H} + \frac{1}{2}M^2 H + 3H\dot{H} = 0\,, \\ &\ddot{R} + 3H\dot{R} + M^2 R = 0\,. \end{aligned} \tag{3.4}$$

Assuming that inflation occurs when $R \gg M$ and $\dot{H} \gg H^2$ one can show that [29, 74]:

$$\begin{aligned} H(t) &= H_i - \frac{M^2}{6}(t - t_i)\,, \\ R(t) &= 12H^2 - M^2\,, \\ a(t) &= a_i \exp\left(H_i(t - t_i) - \frac{M^2}{12}(t - t_i)^2\right)\,, \end{aligned} \tag{3.5}$$

so that the Universe experiences an exponential inflationary expansion.

In order to find a similar behaviour with the action (3.1), $\beta\phi^2$ needs to be constant and equal to $1/6M^2$. However the scalar field is dynamical and follows the Klein-Gordon equation, which reads in the FLRW metric:

$$\ddot{\phi} + 3H\dot{\phi} + V_{,\phi} - \frac{\alpha\phi R + \beta\phi R^2}{\tilde{\kappa}^2} = 0\,, \tag{3.6}$$

and for which the only solution with constant ϕ corresponds to $\phi = 0$ with the minimal dark fluid potential.

To obtain a non-zero and constant ϕ, a possibility is to consider a potential with a non-standard minimum which does not sit at $\phi = 0$. We will study in the following the potential:

$$V(\phi) = V_0 + \frac{m^2}{8v^2}\left(\phi^2 - v^2\right)^2\,, \tag{3.7}$$

which has two minima corresponding to $\phi^2 = v^2$. With this potential $\phi = \pm v$ is a constant solution to the Klein-Gordon equation, and the action (3.1) can lead to inflation, dark matter and dark energy behaviours.

3.3 Inflation

3.3.1 Z_2 spontaneous symmetry breaking

The action (3.1) with the potential defined in Eq. (3.7) is invariant under a Z_2 symmetry ($\phi(x) \to -\phi(x)$). At $\phi = 0$ the potential has a local maximum and the theory is unstable around this value. The two minima correspond to $\phi = \pm v$. When the scalar field goes to one of these minima, the Z_2 symmetry is spontaneously broken. The scalar field ϕ can oscillate around one of the minima so that:

$$\phi = \xi \pm v\,, \tag{3.8}$$

where v is a Vacuum Expectation Value (VEV) and ξ is the variation of scalar field around the minimum. The action (3.1) thus becomes:

$$\mathcal{S} = \int d^4x\sqrt{-g}\Big[\frac{1}{2\tilde{\kappa}^2}\Big(R+\alpha v^2\left(1\pm\frac{2}{v}\xi+\frac{1}{v^2}\xi^2\right)R+\beta v^2\left(1\pm\frac{2}{v}\xi+\frac{1}{v^2}\xi^2\right)R^2\Big) - \frac{1}{2}g^{\mu\nu}\partial_\mu\xi\partial_\nu\xi - V(\xi)\Big], \tag{3.9}$$

with:

$$V(\xi) = V_0 + \frac{m^2}{2}\xi^2 \pm \frac{m^2}{2v}\xi^3 + \frac{m^2}{8v^2}\xi^4\,. \tag{3.10}$$

Also after the spontaneous symmetry breaking and in the limit $|\xi| \ll v$, two terms appear in the action as a result of the dynamical evolution of the scalar field: a term $\alpha v^2 R$ and a term $\beta v^2 R^2$. The first term modifies gravity and can be reabsorbed in the definition of the gravitational constant κ. The second term and will induce an inflation period silimarly to the one in the Starobinsky model. After symmetry breaking, the scalar field variation ξ will behave as a dark fluid.

Usually, as for example in the Higgs-inflation model, the symmetry breaking occurs after inflation but in our case it is the opposite. After symmetry breaking, in the limit $|\xi| \ll v$, one can define the effective gravitational constant κ as:

$$\kappa = \frac{\tilde{\kappa}}{\sqrt{1+\alpha v^2\left(1\pm 2\xi/v+\xi^2/v^2\right)}} \simeq \frac{\tilde{\kappa}}{\sqrt{1+\alpha v^2}}\,. \tag{3.11}$$

If the constant α is positive, the gravitational constant κ in the very early Universe is greater than its value today. It is the opposite way if α is negative. Replacing $\tilde{\kappa}$ by κ, the action (3.9) becomes:

$$\mathcal{S} = \int d^4x\sqrt{-g}\left[\frac{1}{2\kappa^2}\left(R+\frac{\beta v^2}{\alpha v^2+1/\left(1\pm 2\xi/v+\xi^2/v^2\right)}R^2\right)-\frac{1}{2}g^{\mu\nu}\partial_\mu\xi\partial_\nu\xi-V(\xi)\right], \tag{3.12}$$

the standard Einstein's field equations are recovered with in addition a scalar field ξ and a R^2 term which will generate inflation the Universe. Neglecting the effect of ξ during inflation the action (3.12) becomes:

$$\mathcal{S} \simeq \int d^4x\sqrt{-g}\left[\frac{1}{2\kappa^2}\left(R+\frac{\beta v^2}{(1+\alpha v^2)M_P^2}R^2\right)\right]. \tag{3.13}$$

This action corresponds to an $f(R) = R+R^2/(6M^2)$ theory with $6M^2 = (1+\alpha v^2)M_P^2/(\beta v^2)$. Starobinsky inflation model is known to be a viable inflation scenario. Inflation occurs when $R \gg M^2$ and $H^2 \gg |\dot{H}|$, and the typical value of M is $3\times10^{-6}m_P$ with $m_P = \sqrt{8\pi}M_P$ [29]. Therefore a value for $\beta v^2/(1+\alpha v^2)$ is given by:

$$\frac{\beta v^2}{1+\alpha v^2} \simeq 10^9\,, \tag{3.14}$$

but α, β and v are not constrained independently. We however made the assumption that the symmetry breaking occurs before inflation. This assumption imposes only $|\xi| \ll v$ and it is for this reason that we neglected all the terms in front of R^2 in Eq. (3.12) except the constant term.

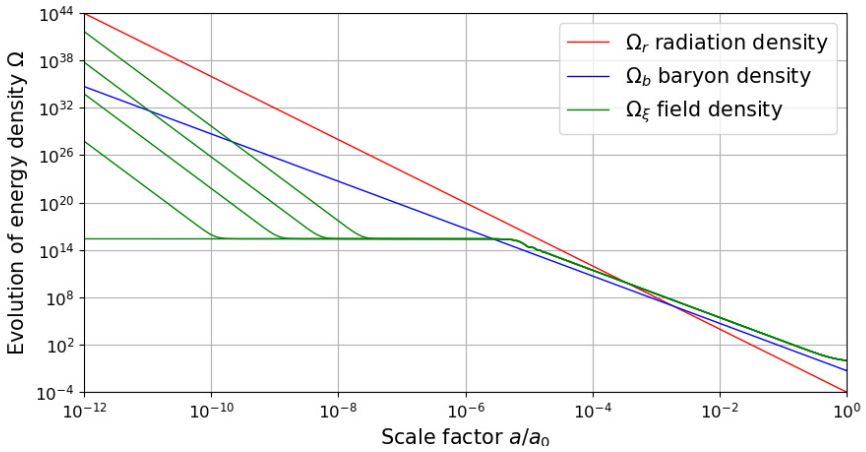

Figure 3.1 – Possible evolutions of the dark fluid density ρ_ξ (green) depending on its initial density. The evolutions of the baryon density (blue) and radiation density (red) are the same as in the ΛCDM model.

3.3.2 Reheating

In this section, we study the production of particles, which can be created via the Unruh effect [75] for which an observer in an accelerated frame can observe the emission of particles off the vacuum. Let us consider the usual reheating scenario after R^2 inflation [27, 29]. As long as the created particles do not modify the evolution of the Universe, the action which describes the model is still:

$$\mathcal{S} = \int d^4x\sqrt{-g}\left[\frac{1}{2\kappa^2}\left(R + \frac{R^2}{6M^2}\right)\right] , \tag{3.15}$$

but the solutions (3.5) are no longer valid. After inflation the Hubble parameter and scalar curvature are in a fast oscillating regime with $M(t - t_{os}) \gg 1$, where t_{os} corresponds to the beginning of the oscillations. The solutions of the Einstein equations are then:

$$\begin{aligned} R &\simeq -\frac{4M}{t - t_{os}} \sin\left(M(t - t_{os})\right) , \\ H &\simeq \frac{4}{3(t - t_{os})} \cos^2\left(\frac{M}{2}(t - t_{os})\right) , \\ \frac{a}{a_0} &\simeq (t - t_{os})^{2/3} . \end{aligned} \tag{3.16}$$

During this oscillating phase, radiation will be produced via the Unruh effect and the total radiation energy density is given by [29, 74]:

$$\rho_r = \frac{\tilde{g}_*}{a^4}\int_{t_{os}}^{t} \frac{Ma^4R^2}{1152\pi} dt , \tag{3.17}$$

where $\tilde{g}_*$ is the number of relativistic degrees of freedom of non-conformally invariant fields. In the Standard Model, $\tilde{g}_*$ is equal to 1 because only the Higgs field can be produced

gravitationally. The articles [76–78] detail some models of reheating in R^2 inflation. At this period the radiation density encompasses (at least) all the Standard Model particles. The evolution of the radiation density is given by:

$$\frac{d\rho_r}{dt} + 4H\rho_r = \frac{g_* M a^4 R^2}{1152\pi}\,, \tag{3.18}$$

where g_* is now the number of relativistic degrees of freedom by supposing a thermalization of the radiation. The second term corresponds to a backreaction due to the expansion of the Universe. At a later stage, when R becomes negligible and the right-hand side term in the previous equation vanishes, the total energy density evolves as $\rho_r \propto a^{-4}$. The integration of Eq. (3.17) is performed by considering the solution of Einstein equations given in (3.16). Without considering the backreaction of radiation, we obtain:

$$\rho_r \simeq \frac{g_* M^3}{240\pi}\frac{1}{t - t_{os}}\,. \tag{3.19}$$

This density evolves slowly as compared to H^2. The radiation domination era begins at $t \simeq t_{os} + 10^3 M_P^2/(g_* M^3)$ and the reheating temperature can be approximated by [27, 29]:

$$T_r \leq 3 \times 10^{16} g_*^{1/4} \left(\frac{M}{M_P}\right)^{3/2} \text{GeV}\,, \tag{3.20}$$

where the T_r is defined implicitly as the temperature at which $\rho_r = g_* \pi^2 T_r^4/30$.

As mentioned in the previous section the field ξ exists before inflation but its density is suppressed by the expansion of the Universe and is negligibly small at the end of inflation. The reheating mechanism of the field ξ is similar to the case of radiation. The energy density of ξ is given by:

$$\rho_\xi \simeq \frac{a_{os}^2}{a^6}\int_{t_{os}}^{t} \frac{M a^4 R^2}{1152\pi} dt\,. \tag{3.21}$$

This density production is negligible compared to the radiation density since the latter is proportional to the large number of relativistic degrees of freedom. The evolution of the density of ξ is shown in Figure 3.1 for different initial densities. One can notice that the scalar field density has no influence on the evolution of the Universe until it starts behaving like dark matter. One can therefore expect the same behavour at late time whatever the scalar field amplitude at the end of inflation.

3.4 Dark fluid behaviour

After inflation the scalar curvature is small and the R^2 term can be safely neglected. The action (3.12) therefore becomes:

$$\mathcal{S} = \int d^4x\sqrt{-g}\left[\frac{1}{2\kappa^2}R - \frac{1}{2}g^{\mu\nu}\partial_\mu\xi\partial_\nu\xi - V(\xi)\right]\,, \tag{3.22}$$

with the potential given in Eq. (3.10).

As we have seen in the previous section the scalar field ξ is expected to behave like a dark fluid: The scalar field ξ can mimick dark energy if:

$$V_0 = \frac{\Lambda}{\kappa} = 2.5 \times 10^{-11}\ \mathrm{eV}^4\,, \tag{3.23}$$

and dark matter if:

$$m \sim 10^{-22}\ \mathrm{eV}\,. \tag{3.24}$$

In addition to the constant term and the mass term the potential contains a $\pm m^2/(2v)\xi^3$ term and a quartic term $m^2/(8v^2)\xi^4$. The effect of the quartic term has already been discussed in Section 2.3.1, and we have seen that $\lambda = m^2/2v^2$ has to be smaller than 10^{-98}, which implies:

$$v \gtrsim 7 \times 10^{26}\ \mathrm{eV}\,. \tag{3.25}$$

The tiny values of the couplings ensure the stability of the potential against quantum corrections [53, 79]. With such a large value of v, which is one order of magnitude below the Planck energy, the symmetry breaking will occur well before inflation, and the term in R^2 can be safely neglected as we had assumed. Provided the minimum value of v the phase transition may be related to the Planck era.

Let us study the impact of the extra ξ^3 and ξ^4 terms of the potential. The scalar field ξ can emulate dark matter if it oscillates quickly around its minimum. In such a case, neglecting the extra terms, the energy density of the dark fluid is:

$$\rho_\xi \simeq \frac{\dot{\xi}^2}{2} + \frac{m^2}{2}\xi^2 + V_0 = m^2\langle\xi^2\rangle + V_0\,, \tag{3.26}$$

where m is fixed to 10^{-22} eV and $v = 7 \times 10^{26}$ eV. In Figure 3.2 the contributions to the scalar field energy density from the different terms of the potential are shown as functions of the scalar field value ξ. The cosmological constant density as well as the average dark matter energy densities in the recent Universe, at the time of matter-radiation equality, and at cluster and galaxy scales are also shown for comparison. As can be seen in the figure, in the present Universe the cubic and quartic terms have negligible contributions as compared to the mass term of the potential at any time and scale in the matter domination period. For example the average dark matter density in galaxies can be obtained by the equation (3.26) which gives $\xi \sim 3 \times 10^{20}$ eV. With this value we have:

$$\begin{aligned} \frac{m^2\xi^3}{2v} \Big/ \frac{m^2\xi^2}{2} &\simeq 5 \times 10^{-7}\,, \\ \frac{m^2\xi^4}{8v^2} \Big/ \frac{m^2\xi^2}{2} &\simeq 5 \times 10^{-14}\,. \end{aligned} \tag{3.27}$$

The contributions of the cubic and quartic terms are even smaller at larger scales. Therefore, they do not affect the dark matter behaviour of the scalar field in galaxies and clusters, and the dark fluid behaves as fuzzy dark matter.

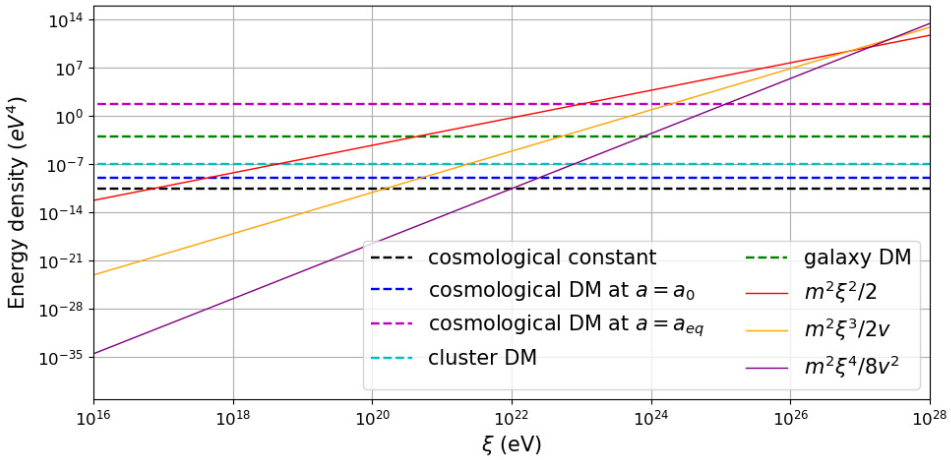

Figure 3.2 – Contributions to the scalar field energy density of the terms $m^2\xi^2/2$ (red), $m^2\xi^3/2v$ (yellow) and $m^2\xi^4/8v^2$ (violet) in the potential (3.10), as a function of the value of the scalar field ξ. The horizontal lines indicate the current observation order of magnitude of the dark matter energy densities at different scales and the potential constant term V_0 corresponding to the cosmological constant.

3.5 Conclusions

We have studied a triple unification model, relying on a single scalar field with a non-minimal gravitational coupling to the squared scalar curvature. The potential of this scalar field has been chosen to be a one-dimensional Mexican hat with two displaced minima plus a constant term. The constant term may also be replaced by a quintessence potential. After a discrete symmetry breaking similar to the one of the Higgs mechanism, a constant term appears in front of the squared scalar curvature, which can generate a R^2-inflation. At the end of inflation, the Standard Model particles will be produced via a reheating mechanism and the massive scalar field resulting from the symmetry breaking will also be reheated. This scalar field has the dark fluid properties and can simultaneously replace dark matter and dark energy. This scenario, in addition to replacing inflation, dark matter and dark energy with a single scalar field, leads to a dark matter behaviour similar to the one of fuzzy dark matter, which alleviates the cuspy halo and missing satellite problems.

3.6 Appendix: alternative action

This appendix motivates the choice of the action (3.1) for the triple unification scenario by introducing two other models which do not match with the CMB data and the constraints on dark fluid model.

3.6.1 Chaotic inflation

Inflationary models have been introduced to explain the flatness and horizon problems. Successful models are based on scalar fields with a slow-roll evolution during a sufficiently long time in order to provide a very large expansion rate in the early Universe, such that $N = \log(a_{end}/a_{beg}) \gtrsim 50$ [27], where N is the number of e-folds. The so-called chaotic inflation model [80], in which a scalar field with quadratic potential is in slow-roll during inflation, can fulfil this constraint. Also in Ref. [68], it is shown that chaotic inflation can be obtained together with dark energy using a scalar field associated to the potential

$$V(\phi) = \frac{m^2}{2}\phi^2 + V_0\,. \tag{3.28}$$

The main problem to unify chaotic inflation and dark energy is that the observation of the CMB anisotropies imposes $m \simeq 3 \times 10^{-6} M_P$ [2], which is not in agreement with the mass needed for a dark fluid model. Using instead a quartic potential which becomes dominant during the inflation:

$$V(\phi) \simeq \frac{\lambda}{4!}\phi^4\,, \tag{3.29}$$

λ has to be of the order of 10^{-14} to be compatible with CMB data [2], which is incompatible with the dark fluid setup. Therefore the dark fluid potentials derived in the previous section cannot lead to a chaotic inflation in agreement with the observational data.

3.6.2 Non-minimal coupling $\phi^2 R$

A first solution to unify inflation and dark fluid model would be to consider a non-minimal coupling between the dark fluid scalar field and the scalar curvature. Such couplings have been studied in the context of the Higgs-inflation scenario [81]. Let us consider the following action:

$$\mathcal{S} = \int d^4x\sqrt{-g}\left[\frac{1}{2\kappa^2}\left(1 + \frac{\alpha^2}{M_P^2}\phi^2\right)R - \frac{1}{2}g^{\mu\nu}\partial_\mu\phi\partial_\nu\phi - V(\phi)\right]\,, \tag{3.30}$$

with $\kappa^2 = M_P^{-2}$ and

$$V(\phi) = V_0 + \frac{m^2}{2}\phi^2 + \frac{\lambda}{4}\phi^4\,. \tag{3.31}$$

The α^2 coupling is chosen to be positive in order to ensure that the coupling to gravity always remains positive. The parameters V_0, m and λ are fixed by the dark fluid model requirements, and the only free parameter is therefore α. This action is assumed to be written in the Jordan frame in which the scalar field is non-minimally coupled to the Ricci scalar R. To confront this model with the CMB data, it is necessary to rewrite the action

in the Einstein frame by making a conformal transformation. In the Einstein frame, where the quantities are represented by a tilde, the metric is:

$$\tilde{g}_{\mu\nu} = \Omega^2 g_{\mu\nu}\,, \tag{3.32}$$

where Ω^2 is the conformal factor such that

$$\Omega^2 = 1 + \alpha^2 \frac{\phi^2}{M_P^2}\,. \tag{3.33}$$

Following Ref. [82], one defines the effective scalar field ψ and potential U such that

$$\begin{aligned} \frac{d\psi}{d\phi} &= \sqrt{\frac{\Omega^2 + 6\alpha^4\phi^2/M_P^2}{\Omega^4}}\,, \\ U(\psi) &= \Omega^{-4} V(\phi)\,, \end{aligned} \tag{3.34}$$

and the action (3.30) takes the form of the usual Einstein-Hilbert action:

$$\mathcal{S} = \int d^4x\sqrt{-\tilde{g}}\left[\frac{1}{2\kappa^2}\tilde{R} - \frac{1}{2}\tilde{g}^{\mu\nu}\partial_\mu\psi\partial_\nu\psi - U(\psi)\right]. \tag{3.35}$$

The observational constraints on the spectral index n_s implies $\alpha^2 > 4\times 10^{-3}$ [27].

On the other hand the parameter α can be constrained by the observational power spectrum which is related to the potential by [32]:

$$\delta_H^2 = \frac{4}{25}\mathcal{P}_\mathcal{R} = \frac{1}{150\pi^2 M_P^4}\frac{U}{\epsilon_v}\,, \tag{3.36}$$

where

$$\epsilon_v = \frac{M_P^2}{2}\left(\frac{U'(\phi)}{U(\phi)}\right)^2 = \frac{M_P^2}{\phi^2}\frac{8}{1+(1+6\alpha^2)\alpha^2\phi^2/M_P^2} \tag{3.37}$$

is the slow-roll parameter [82]. The power spectrum has to be calculated at the time of the end of inflation t_{end}, which is related to the number of e-folds N:

$$N = \int_{\phi_{beg}}^{\phi_{end}} \frac{\phi}{M_P}\frac{1+(1+6\alpha^2)\alpha^2\phi^2/M_P^2}{4\left(1+\alpha^2\phi^2/M_P^2\right)}d\phi\,, \tag{3.38}$$

where ϕ_{end} corresponds to $\epsilon_v = 1$. Unfortunately, the system:

$$\begin{aligned} &\frac{M_P^2}{\phi_{end}^2}\frac{8}{1+(1+6\alpha^2)\alpha^2\phi_{end}^2/M_P^2} = 1\,, \\ &8N = (1+6\alpha^2)\left(\frac{\phi_{beg}^2}{M_P^2} - \frac{\phi_{end}^2}{M_P^2}\right) + 6\ln\left(\frac{1+\alpha^2\phi_{beg}^2/M_P^2}{1+\alpha^2\phi_{end}^2/M_P^2}\right)\,, \\ &\mathcal{P}_\mathcal{R}^* = \frac{\lambda}{192\pi^2}\frac{\phi_{beg}^6}{M_P^6}\left(1+(1+6\alpha^2)\alpha^2\frac{\phi_{beg}^2}{M_P^2}\right)\,, \end{aligned} \tag{3.39}$$

has no valid solution for $\lambda \sim 10^{-100}$. For example assuming $\alpha^2 \geq 1$ the first equation leads to $\alpha^2\phi_{end}^2 \sim 1.2M_P^2$, the second one gives $\alpha^2\phi_{beg}^2 \sim 75M_P^2$ for $N \simeq 55$, and the third

one imposes $\alpha^2 \sim 10^{-42}$, which contradicts the other requirements. Therefore, it is not possible to unify inflation and dark fluid with a coupling $\phi^2 R$. This result is different from the ones obtained in the context of Higgs-inflation model, in which the quartic coupling λ is much larger. In our case the parameter λ is too small to reproduce the amplitude of the anisotropies.

4 Big-Bang nucleosynthesis

Scalar fields are widely used in cosmology, in particular to emulate dark energy in quintessence models, or to explain dark matter in scenarios such as the fuzzy dark matter model. In addition, many scenarios involving primordial scalar fields which may have driven inflation or baryogenesis are currently under scrutiny. In this chapter, we investigate the impact of such scalar fields on Big-Bang nucleosynthesis and derive constraints on their energy density using the observed abundance of the elements.

Contents

4.1 Master equations

In the cosmological standard model, before the beginning of BBN the expansion of the Universe is dominated by radiation. The dominating species are photons γ, electrons and positrons $e^{\mp}$, baryons b, neutrinos ν and antineutrinos $\bar{\nu}$, and dark matter χ. In presence of a scalar field, the total energy density and pressure of the primordial plasma can be written as

$$\begin{aligned} \rho_{\rm tot} &= \rho_\gamma + \rho_{\nu,\bar{\nu}} + \rho_{\rm b} + \rho_{e^\mp} + \rho_\chi + \rho_\phi \,, \\ P_{\rm tot} &= P_\gamma + P_{\nu,\bar{\nu}} + P_{e^\mp} + P_\phi \,, \end{aligned} \tag{4.1}$$

where the baryon and dark matter densities are considered as pressureless.

The link between temperature and time is given by the conservation of the total radiation entropy, namely:

$$\frac{ds_{\rm rad}}{dt} = -3Hs_{\rm rad}\,. \tag{4.2}$$

The different chemical elements are in interaction through nuclear reactions of the type

$$N_i\ {}^{A_i}Z_i + N_j\ {}^{A_j}Z_j + N_k\ {}^{A_k}Z_k \leftrightarrow N_l\ {}^{A_l}Z_l + N_m\ {}^{A_m}Z_m + N_n\ {}^{A_n}Z_n\,, \tag{4.3}$$

where the N_i are the number of nuclei Z_i which enter the reaction and A_i their atomic numbers. The evolution of the number of each of the elements is driven by the Boltzmann equations:

$$\frac{dY_i}{dt} = N_i \sum_{j,k,l,m,n} \left(-\frac{Y_i^{N_i} Y_j^{N_j} Y_k^{N_k}}{N_i! N_j! N_k!}\Gamma_{ijk\to lmn} + \frac{Y_l^{N_l} Y_m^{N_m} Y_n^{N_n}}{N_l! N_m! N_n!}\Gamma_{lmn\to ijk} \right)\,, \tag{4.4}$$

where $\Gamma_{ijk\to lmn}$ and $\Gamma_{lmn\to ijk}$ are the forward and reverse reaction rates of Eq. (4.3).

BBN occurs for a scale factor of about $a_{\rm BBN} \sim 10^{-10}$ and a temperature scale of $T_{\rm BBN} \sim 1$ MeV, and the abundance of the elements after BBN can be obtained by integrating simultaneously Eqs. (4.1)–(4.4) with Friedmann equations.

4.2 Observational constraints

We compute the abundance of the elements using the public code AlterBBN [83, 84], which has been modified to incorporate different kinds of scalar fields. We will compare the abundances to the following set of observational measurements [85]:

$$\begin{aligned} &Y_p = 0.245 \pm \times 0.003\,,\\ &{}^2H/H = (2.569 \pm 0.027) \times 10^{-5}\,,\\ &{}^3He/H = (1.1 \pm 0.2) \times 10^{-5}\,. \end{aligned} \tag{4.5}$$

The exclusion is obtained via a χ^2 analysis at 95% C.L.

In addition, the observations of the lithium-7 abundance give [85]:

$$^7Li/H = (1.6 \pm 0.3) \times 10^{-10}\,. \tag{4.6}$$

Whereas the observations of the previous abundances are compatible with the predictions in the cosmological standard model, the ^7Li abundance shows a discrepancy of more than 3σ between the observation and the prediction, which is too large by a factor three. We will check in the following analysis whether the presence of a scalar field can explain this discrepancy.

4.3 Decaying scalar fields

In the early Universe, cosmological scalars such as inflatons [81, 86], dilatons [87, 88] or moduli [89–92] could give birth to specific phenomena such as inflation or leptogenesis.

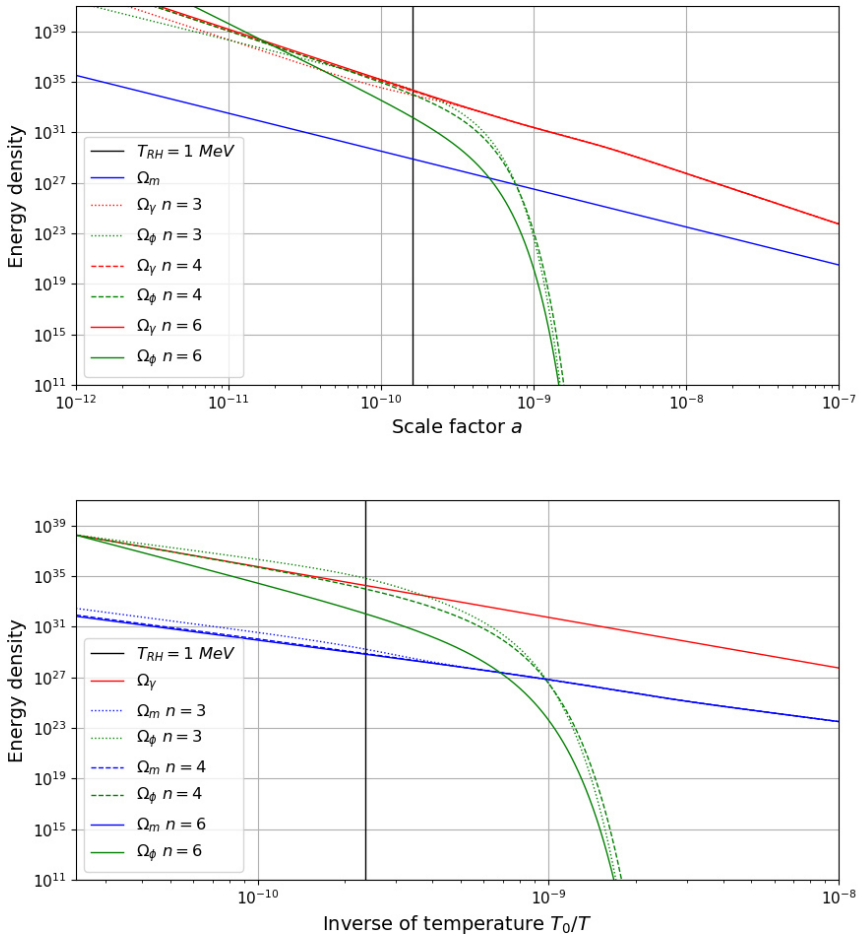

Figure 4.1 – Evolution of the decaying scalar field density, matter density and radiation density as functions of the scale factor (top) and of the temperature (bottom), for a reheating temperature of 1 MeV displayed by the vertical black lines. In absence of decay, the scalar field density evolves as a^{-n}. The initial densities of the scalar field are chosen so that $\rho_\phi = \rho_\gamma$ at $T = 10$ MeV for different values of n.

Their common features is that they did not survive, at least in non-negligible proportions. We can therefore assume that these scalar fields decayed at a period prior to recombination, so that they did not leave imprint in the CMB.

Contrary to the cases studied in the previous sections, decaying scalar fields are not constrained by observations of the present Universe, and generally neither by observations of the CMB. The form of the potential and its behaviour remains therefore arbitrary. If such scalar fields decay much before BBN, they will have no effect either on BBN or recombination. If they decay after BBN, either their densities are negligible and they have no effect on the cosmological history, or their densities are large enough to impact BBN by modifying the expansion rate and the decay has to occur soon enough in order to escape

constraints from CMB. In the latter case, the scalar fields can be considered as stable during BBN, with a constant equation of state $w_\phi \in [-1, 1]$, leading to a density scaling as $\rho_\phi \propto a^{-n}$, with $n \in [0, 6]$.

We consider now the case of a scalar field decaying at the BBN epoch. To simplify the analysis, we assume an instantaneous thermalization with the thermal bath, and a dominant decay into radiation.

The Klein-Gordon equation becomes:

$$\ddot{\phi} + 3H\dot{\phi} + \frac{dU}{d\phi} = -\Gamma_\phi \rho_\phi \,, \tag{4.7}$$

and the total radiation entropy receives an injection such that:

$$\frac{\partial s_{\rm rad}}{\partial t} = -3H s_{\rm rad} + \frac{\Gamma_\phi \rho_\phi}{T} \,, \tag{4.8}$$

where Γ_ϕ is the decay width of the scalar field.

We assume here that the scalar field potential is a power law, so that during BBN and in absence of decay it evolves as

$$\rho_\phi = \rho_\phi^0 a^{-n} \,, \tag{4.9}$$

where n is a constant parameter between 0 and 6. Thus the Klein-Gordon equation can be rewritten as:

$$\frac{d\rho_\phi}{dt} = -nH\rho_\phi - \Gamma_\phi \rho_\phi \,. \tag{4.10}$$

Following [93, 94] we define the reheating temperature $T_{\rm RH}$ of the scalar field as:

$$\Gamma_\phi = \sqrt{\frac{4\pi^3 g_{\rm eff}(T_{\rm RH})}{45}} \frac{T_{\rm RH}^2}{M_P} \,, \tag{4.11}$$

where $g_{\rm eff}$ is the number of effective energy degrees of freedom of radiation. The model is therefore defined by three parameters: the exponent n, the reheating temperature $T_{\rm RH}$ and the initial scalar field density.

Figure 4.1 shows the evolution of the scalar field as a function of the scale factor or the temperature, for a reheating temperature of 1 MeV. The scalar field density at the initial temperature $T_i = 10$ MeV has been chosen so that $\rho_\phi = \rho_\gamma$ for $n = 3, 4, 6$. Since the decay of the scalar field induces a reheating by increasing the radiation density, the initial value of the matter density has been adjusted in order to obtain the observed baryon-to-photon ratio from the CMB. This effect can be seen in the top panel of the figure, where the evolution of the densities is shown as a function of the scale factor: the radiation density increases at a scale factor corresponding to the reheating temperature. This is the reason why the photon density is different for each choice of n. In the bottom panel where the evolution is shown as a function of the temperature, this effect translates into a decrease of the matter density, which is equivalent to lowering the baryon over radiation ratio to obtain the value derived from the CMB observations. This is also the reason why the matter density appears as different for each choice of n.

We see that after reheating, the decrease of the scalar field accelerates and its density drops very quickly, increasing simultaneously the radiation density. It can therefore be expected that a decaying scalar field can modify BBN for $T_{\rm RH} \in [1, 10]$ MeV.

4.4 BBN constraints on cosmological scalar fields

In the previous sections, we have analysed the cosmological behaviours of a broad range of scalar fields. In this section, we study the constraints from BBN on scalar field models, considering separately the cases of the stable and decaying scalar fields.

4.4.1 Stable scalar fields

Stable scalar fields have in general a constant equation of state during BBN, with w_ϕ ranging from -1 to $+1$ corresponding to a density varying as a^{-n} with $n \in [0, 6]$. The most standard values are 1 (kinetic term domination) and 1/3 (radiation-like behaviour), corresponding to densities scaling as the inverse of the scale factor with an exponent 6 and 4, respectively.

In the cases when $w_\phi < 0$, since the scalar field density decreases more slowly than radiation, if the scalar field density is not completely negligible, it will start dominating the expansion of the Universe during or after BBN, and can even affect the CMB.

In presence of a scalar field, the expansion rate given by the Friedmann equation will be modified during BBN. Two extreme cases can be considered. The first one corresponds to a scalar field density negligible with respect to the photon density at $T \sim 1$ MeV. We will obtain in this case the same results as in the standard cosmological model. The opposite case is the domination of the scalar field density at BBN time, which will modify the abundance of the elements via Hubble rate modification.

Figure 4.2 shows Y_p and the abundances of ^2H, ^3He and ^7Li for different values of the exponent n and the scalar field density at $T \sim 1$ MeV. The dashed lines correspond to exclusions by the individual constraints for each element at 95% C.L. Using the χ^2 approach we obtain at 95% C.L.:

- for $n_\phi = 0$ (constant density, potential domination), BBN constraints exclude:

$$\rho_\phi(1\text{ MeV}) \gtrsim 2 \times 10^{-7}\, \rho_\gamma(1\text{ MeV})\,. \tag{4.12}$$

- for $n_\phi = 3$ (matter-like behaviour), BBN constraints exclude:

$$\rho_\phi(1\text{ MeV}) \gtrsim 0.005\, \rho_\gamma(1\text{ MeV})\,. \tag{4.13}$$

- for $n_\phi = 4$ (radiation-like behaviour), BBN constraints exclude:

$$\rho_\phi(1\text{ MeV}) \gtrsim 0.11\, \rho_\gamma(1\text{ MeV})\,. \tag{4.14}$$

- for $n_\phi = 6$ (kinetic term domination), BBN constraints exclude:

$$\rho_\phi(1\text{ MeV}) \gtrsim 1.40\, \rho_\gamma(1\text{ MeV})\,. \tag{4.15}$$

In addition, the ^7Li abundance can be modified by the scalar field, but as we can see from Figure 4.2, there is no region where the predictions for Y_p, ^2H, ^3He and ^7Li can be simultaneously in agreement with their observational values.

In terms of physical models, scalar fields behaving like matter (fuzzy dark matter, ...) do not affect BBN and no constraint can be found. For quintessence or dark field models on the other hand, Eq. (4.14) applies for tracking scenarios with fixed points solutions, or Eq. (4.15) in more general scenarios with generic initial conditions. For more exotic scenarios, BBN constraints can be obtained from Figure 4.2.

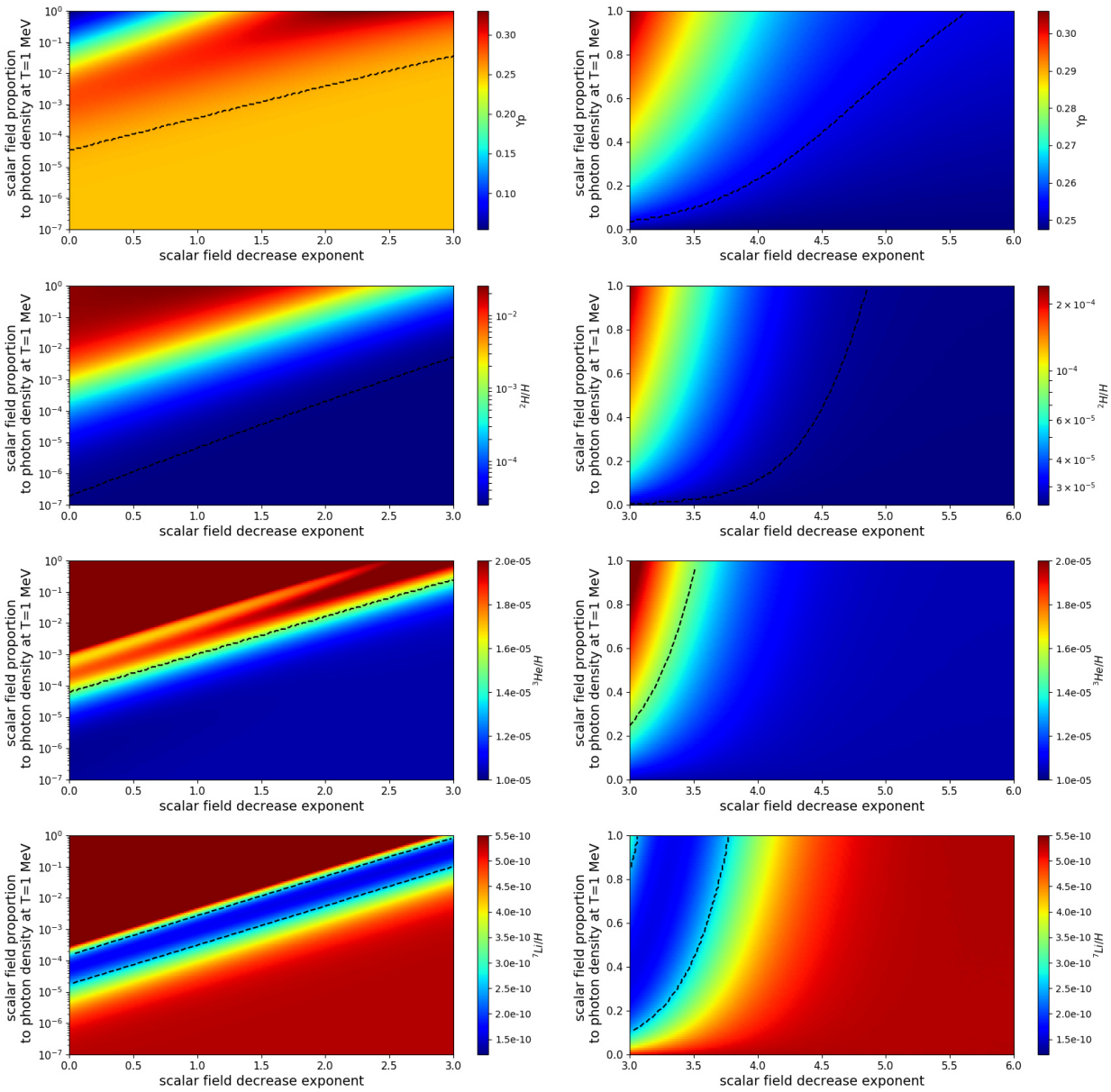

Figure 4.2 – From top to bottom, values of Y_p, $^2H/H$, $^3He/H$ and $^7Li/H$, as a function of the decrease exponent n and the initial scalar field density (normalized to photon density) at $T = 1$ MeV, (left) with a logarithm scale on the y-axis and for $n \leq 3$, and (right) with a linear scale on the y-axis and for $n \geq 3$. The dashed lines represent the individual BBN constraints at 95% C.L. Except for ^7Li, the excluded region is above the lines.

4.4.2 Decaying scalar fields

We now turn to the case of decaying scalar fields. As discussed before, if the scalar field decays after BBN, the constraints that we just obtained remain valid. On the other hand, if the decay is terminated when BBN starts, the scalar field will have a negligible density which will have no effect on BBN.

We now turn to the case of decaying scalar fields with reheating temperatures below 10 MeV. We consider scalar fields which evolve as $\rho_\phi \propto a^{-n}$ in absence of decay, for $n = 0, 3, 4, 6$.

In Figure 4.3, we present the abundance of the elements for $n = 0, 3$ as functions of the reheating temperature $T_{\rm RH}$ and the ratio of the scalar field density to the photon density at $T = 10$ MeV.[1] The same plots are obtained with $n = 4, 6$ in Figure 4.4. The dashed lines correspond to exclusions by the individual constraints for each element at 95% C.L. Using the χ^2 approach at 95% C.L. we obtain the following results:

- for $n = 0$, the compatible parameter region corresponds to large reheating temperatures and small densities. Indeed, before the decay, the density of the scalar field is constant, meaning that it will dominate and accelerate the expansion over the radiation density, which decreases as T^4. This model is therefore strongly constrained, so that only a small fraction of constant scalar field can be allowed.
- for $n = 3$, since the scalar field has a matter-like behaviour, if the scalar field density dominates the expansion, the expansion rate is smaller before its decay. We see that such a scenario is excluded if

$$\rho_\phi(10\text{ MeV}) \gtrsim 0.01 \left(\frac{T_{\rm RH}}{1\text{ MeV}}\right) \rho_\gamma(10\text{ MeV})\,. \tag{4.16}$$

  There is therefore a compensation between the modification of the expansion rate and the injection of radiation.
- for $n = 4$, we obtain a limit

$$\rho_\phi(10\text{ MeV}) \gtrsim 0.1\,\rho_\gamma(10\text{ MeV})\,, \tag{4.17}$$

  which is equivalent to the limit obtained for a stable scalar field. This could be expected since the scalar field had originally a radiation-like behaviour and decays into radiation.
- for $n = 6$, BBN is unaffected for $\rho_\phi(10\text{ MeV}) \lesssim 0.5\,\rho_\gamma(10\text{ MeV})$ independently of the reheating temperature, or when the reheating temperature is below 4 MeV and $\rho_\phi(10\text{ MeV}) \lesssim \rho_\gamma(10\text{ MeV})$. For large reheating temperatures, the scalar field decays earlier, increases the radiation density, decelerates the expansion, and modifies the abundance of the elements even for small values of the initial density. For lower reheating temperatures, the expansion rate is increased but slowed down before the decay, and less constraining limits are thus obtained.

1. It is important to note that the initial densities of the decaying scalar fields are fixed at $T = 10$ MeV, contrary to the case of stable scalar fields where the initial temperature was $T = 1$ MeV.

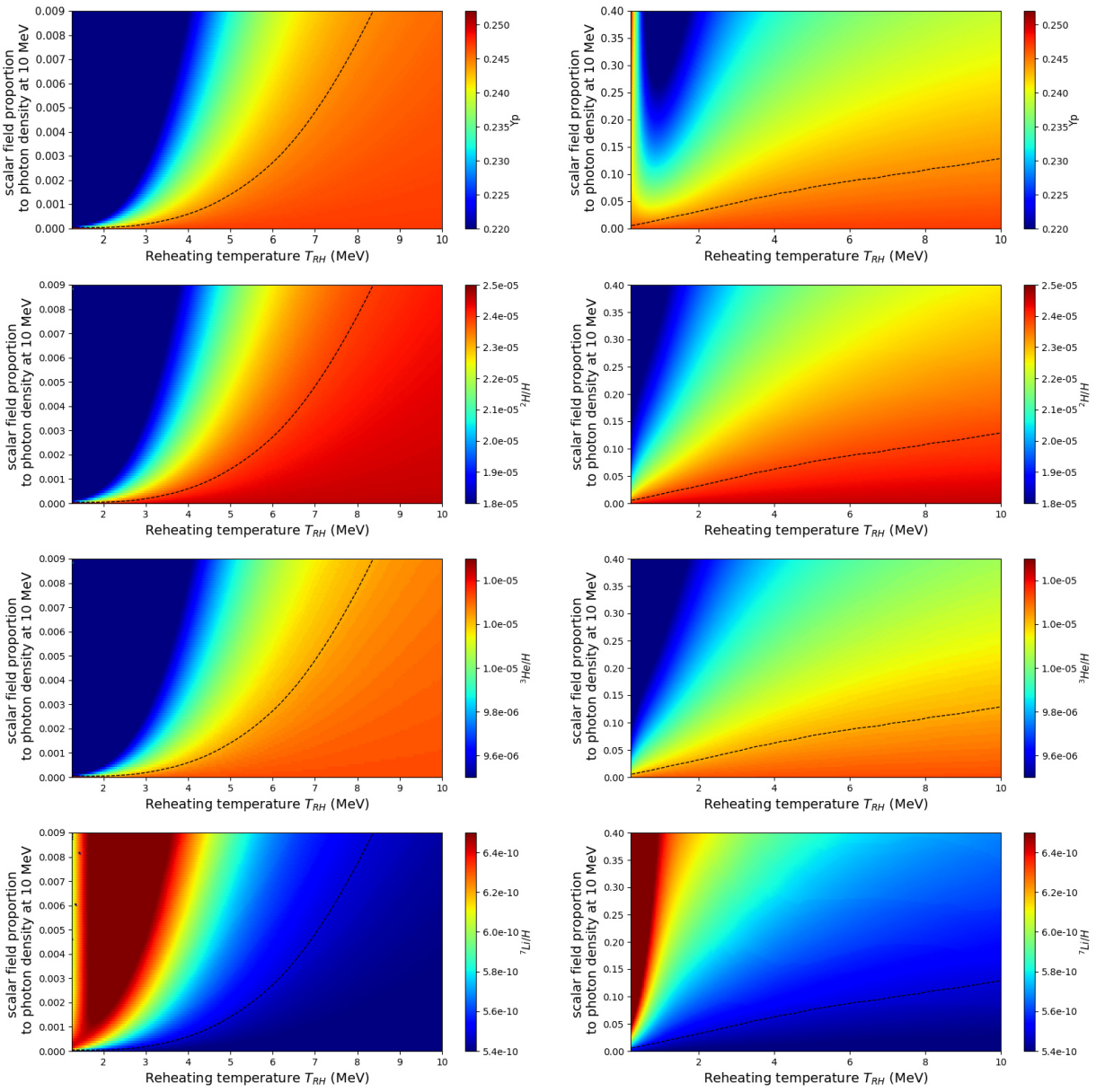

Figure 4.3 – From top to bottom, values of Y_p, $^2H/H$, $^3He/H$ and $^7Li/H$, as functions of the reheating temperature T_{RH} and the initial scalar field density (normalized to photon density) at $T = 10$ MeV, for (left) a constant density $n = 0$, and (right) a matter-like behaviour $n = 3$. The dashed lines represent the individual BBN constraints at 95% C.L. Except for ^7Li, the excluded regions are above the lines.

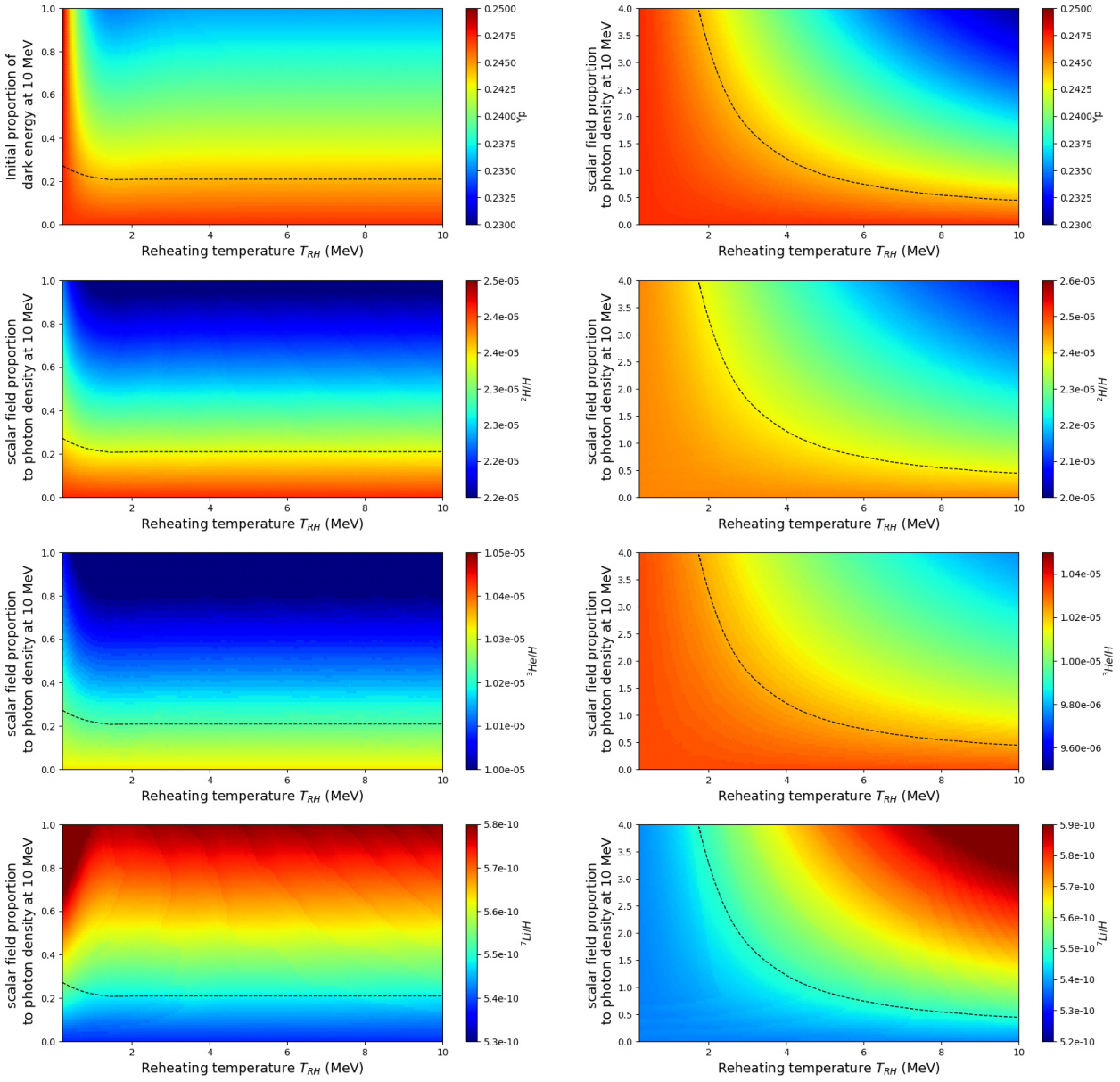

Figure 4.4 – From top to bottom, values of Y_p, $^2H/H$, $^3He/H$ and $^7Li/H$, as functions of the reheating temperature $T_{\rm RH}$ and the initial scalar field density (normalized to photon density) at $T = 10$ MeV, for (left) a radiation-like behaviour $n = 4$, and (right) a dominating kinetic term $n = 6$. The dashed lines represent the individual BBN constraints at 95% C.L. Except for ^7Li, the excluded regions are above the lines.

Similarly to the case of stable scalar fields, there is no possibility to simultaneously explain the abundance of ^7Li and be consistent with the constraints on the ^4He, ^2H and ^3He abundances.

To summarize, in the very early Universe the primordial scalar fields are likely to have a constant density or a dominating kinetic term. For the constant behaviour, it is mandatory for the scalar field to have a subleading density at BBN time, independently of the reheating temperature. On the contrary, for a kinetic term dominated scalar field, the initial density can be rather large, and even dominant for low reheating temperature, meaning that a late reheating is favoured in such cases.

4.5 Summary

In this part, we have studied the cosmological evolution of scalar fields and studied their impact on Big-Bang nucleosynthesis. We have shown that the scalar fields can have non-negligible densities ρ_ϕ at the time of BBN and equations of state $w_\phi = P_\phi/\rho_\phi$ between -1 and $+1$.

Scalar fields can replace a cosmological constant, for example in quintessence models, and we show that the most usual dark energy scenarios lead to $w_\phi = 0$, $w_\phi = 1/3$ or $w_\phi = 1$ at BBN time, which can affect BBN if the scalar field density is non-negligible at this epoch.

Scalar fields can also act as dark matter, with $w_\phi = 0$ today, as it is the case in fuzzy dark matter scenarios. In the early Universe, the kinetic term generally dominates, giving an equation of state $w_\phi = 1$ at BBN time. However, because of the constraints from studies of the CMB, the density of such scalar fields is negligible at the time of BBN, and no constraint can be obtained from BBN.

Similarly, dark fluid models with scalar fields replacing simultaneously dark matter and dark energy are extremely constrained both by dark matter constraints at local and large scales and by dark energy constraints at cosmological scales, and we showed that in the most simple models, no constraints can be obtained from BBN since the scalar field density at BBN epoch is negligible. Only more complex models incorporating specific dark energy potentials are likely to have effects on BBN, and the constraints are expected to be similar to the ones obtained on quintessence scenarios.

Primordial scalar fields which have decayed during BBN are on the contrary more likely to have affected the abundance of the elements, in two different ways. First the scalar field density increases the total density and affects the expansion rate of the Universe. This effect can be particularly important since no strong constraint can limit the decaying scalar field parameters at BBN time, so that large densities are still possible during BBN. Second the decay into radiation injects entropy which modifies the relation between time (or scale factor) and temperature and generates a reheating at the BBN epoch. We considered the most usual cases, *i.e.* a scalar field density scaling as a^{-n} in absence of decay, with $n = 0, 3, 4, 6$, and derived constraints on the reheating temperature $T_{\rm RH}$ and the initial scalar field density.

Regardless of the scalar field model, we showed that it is not possible to find setups which simultaneously satisfy the Y_p,^2H,^3He constraints and the ^7Li one. In other terms, the lithium problem cannot be solved via the scalar field models that we considered. It may

however be possible to design scenarios with scalar fields decaying into specific particles which may affect BBN and decrease the abundance of lithium-7. We defer this task to later studies.

Part II

Primordial Black Holes & Gravitational Waves

5

Basic concepts

In this chapter, we will briefly review some developments on primordial black holes which differ from usual black holes in their origins: primordial black holes are produced in the early Universe. One motivation for studying primordial black holes is that they may constitute a large fraction of dark matter. Gravitational wave detections provide new opportunities to test the predictions of General Relativity and perhaps to observe primordial black holes. So far, general relativity has passed all the tests successfully, but solving Einstein's equations for a binary system requires the use of numerical relativity. The code `Einstein toolkit` [95] can be used to produce gravitational wave-forms from a binary black hole merger. To describe a neutron star, an equation of state must be given and the goal is to use the Meta Model which is able to reproduce all known equations of state and even more. In this case, the code `Whisky_THC` [96, 97] can be used to produce gravitational wave-forms from a binary neutron star merger.

Contents

5.1 Type of black holes

5.1.1 Black holes

In astrophysics, a black hole is a compact object whose gravitational field is so strong that even the light can not escape. Such an object is described by General Relativity with the Schwarzschild metric in the simplest case ($J = 0$ and $Q = 0$) and with the Kerr-Newman metric for a charged and spinning black hole. A black hole appears as a hole in space-time whose a boundary is called "event horizon". If an object crosses such a horizon, it becomes causally disconnected from our Universe.

Black holes are not purely theoretical any more, but they have been observed and at every galactic center, it seems that there is a supermassive black hole. A wonderful picture of the shadow of the M87 supermassive black hole was made by the Event Horizon Telescope [98]. In addition, on September 4, 2015 the first observation of gravitational waves from a binary black hole merger [10] with a mass of about 30 $M_\odot$ for each black hole was made by the Hanford and Livingston LIGO detectors. Since this first detection, the GWTC-1 catalog [99] reports ten binary black hole coalescence events detected in run O1 from September 12, 2015 to January 19, 2016 and in run O2 from November 30, 2016 to August 5, 2017. For the O3 run from April 1, 2019 to October 1, 2019 it is 34 events [99]. Neutron star binaries and black hole - neutron star binaries have also been detected. The distinction between these mergers is done via the mass of compact objects. There is a mass gap between the masses of black holes and neutron stars: even if the boundaries are still under debate, the mass of neutron stars may be estimated to be approximately smaller than 2 $M_\odot$ and the mass of black holes larger than 5 $M_\odot$. However, a compact object of 2.6 $M_\odot$ has been observed [12] thanks to gravitational waves and its nature is undetermined.

According to their masses, black holes can be classified into three main families:

- *stellar black holes* coming from the explosion of massive stars or supernovae, are well observed by the LIGO/Virgo collaboration through gravitational waves. Their masses are between 5 $M_\odot$ and 100 $M_\odot$
- *intermediate mass black holes* which constitute a new class recently discovered by LIGO/Virgo collaboration [100]. Their masses are between 100 $M_\odot$ and 10^5 $M_\odot$
- *supermassive black holes* are found in the center of galaxies. Their masses are between 10^6 $M_\odot$ and 10^9 $M_\odot$. In the future, LISA will study them in more detail.

Finally, with the no-hair theorem, a black hole is a simple object defined only by a few parameters, but it also emits the so-called Hawking radiation [101]. For a neutral and non-rotating black hole of mass M, the temperature T_H of the thermal radiation is given by:

$$k_B T_H = \frac{1}{2\pi} \frac{\hbar c^3}{4GM} , \tag{5.1}$$

where k_B is the Boltzmann constant, c the speed of light, G the Newton constant and $\hbar$ the Planck constant. For a 5 $M_\odot$ stellar black hole, the temperature is only 3×10^{-7} K which

is impossible to observe. However, Hawking radiation can be generated and detected in analogous gravity [102, 103] by the creation of a sonic horizon in transonic flow. A Bose-Einstein condensate in stationary transonic flow spontaneously emits correlated photons which were detected by J. Steinhauer [104], which is the analogue of Hawking radiation. Such radiation is too small to impact a standard black hole, but the Hawking temperature is inversely proportional to the mass M, so it can evaporate a tiny primordial black hole.

5.1.2 Primordial black holes

Primordial black holes are not formed by the collapse of stars or during the formation of galaxies. They were formed at the beginning of the Universe, by collapse of large primordial densities at the end of inflation, or during some phase transitions; or by collapse of cosmic string or domain walls ... The distinction between PBH and BH comes from the "primordial" term, but they are described by the same Kerr-Newman metric. The mechanism of formation of PBH is not well know but it is possible that PBHs formed with a huge spin close to the extremal Kerr BH contrary to stellar BHs which generally have a weak spin. The angular momentum of BHs increases when it accretes matter, but does not approach the extreme spin limit in this way.

Assuming that a PBH is formed in a Hubble volume in the early Universe, one gets [105]:

$$M_{PBH} \sim M_{Planck} \times \frac{t_0}{t_{Planck}} \sim 10^{38} g \times t_0(s) \tag{5.2}$$

where t_0 is the creation time. If a PBH forms at the Planck time, its mass will be the Planck mass which is equal to 10^{-5} g. If a PBH forms after 1 second after the beginning of the Universe, its mass will be 10^5 $M_\odot$ and it will be classified as supermassive black hole.

BHs detected by the LIGO/Virgo collaboration are assumed to originate from star collapse or coalescence of some compact objects, but some gravitational events could originate from PBHs [106–108]. An event with a BH below the Chandrasekhar mass limit will be a big step to prove that PBHs exist.

5.2 Primordial black hole as dark matter candidates

5.2.1 Advantages of primordial black holes

The nature of dark matter remains a major unresolved question in cosmology. In particle physics with models beyond the Standard Model, cold dark matter can be described by involking weakly-interactive particles, but these particles have still not been discovered by direct and indirect detection and there is no clue of new physics at colliders. In Part I, we introduced a light scalar field that can describe dark matter through the fuzzy dark matter model, but another interesting idea is to consider that primordial black holes constitute a significant part of cold dark matter. With such a model, gravity is still described by the usual General Relativity, black holes exist, there is no need to introduce new unobserved particles and the only assumption is that some over-densities in the early Universe collapsed into black holes.

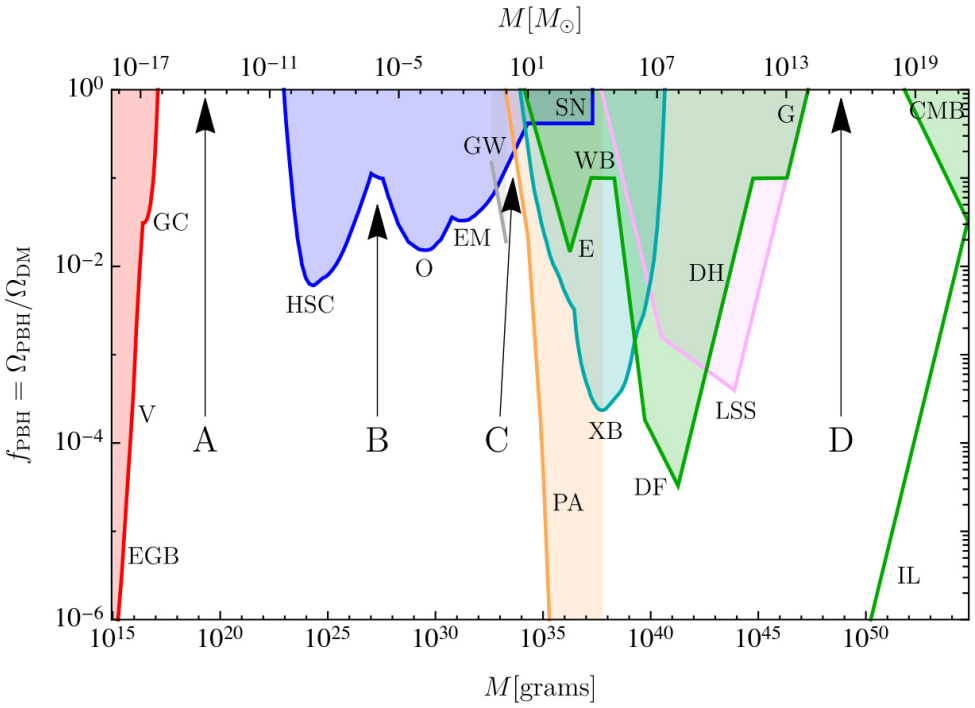

Figure 5.1 – Constraints the fraction of PBHs with respect to DM as a function of the PBH mass from [5]: red from evaporation, blue from lensing, gray from gravitational waves, green from dynamical effects, light blue from accretion, orange from CMB distortions and purples from large scale structure. A, B, C and D are possible open windows.

5.2.2 Open windows

To explain partly cold dark matter with primordial black holes, their masses should fall within one of the four open windows drawn in Figure 5.1 [5]. This figure gathers the current constraints on the upper limit of the mass fraction of primordial black holes with respect to dark matter. If this fraction can be equal to one as is the case in windows A and D, all dark matter could be explained by primordial black holes. The red constraint is the most robust and corresponds to the evaporation of black hole. Below 5×10^{14} g, the time life of primordial black holes is less than the age of the Universe. The blue color corresponds to the gravitational lensing constraint, etc.

5.3 Gravitational sources

A charge displacement will produce electromagnetic waves and, by analogy, a mass displacement will produce gravitational waves. One difference is that in General Relativity, a spherical system does not emit gravitational waves, but any asymmetric supernovae explosion will. A rotating star with a mountain on its surface will also produce them. Another example comes from the binary systems that have been detected by the mod-

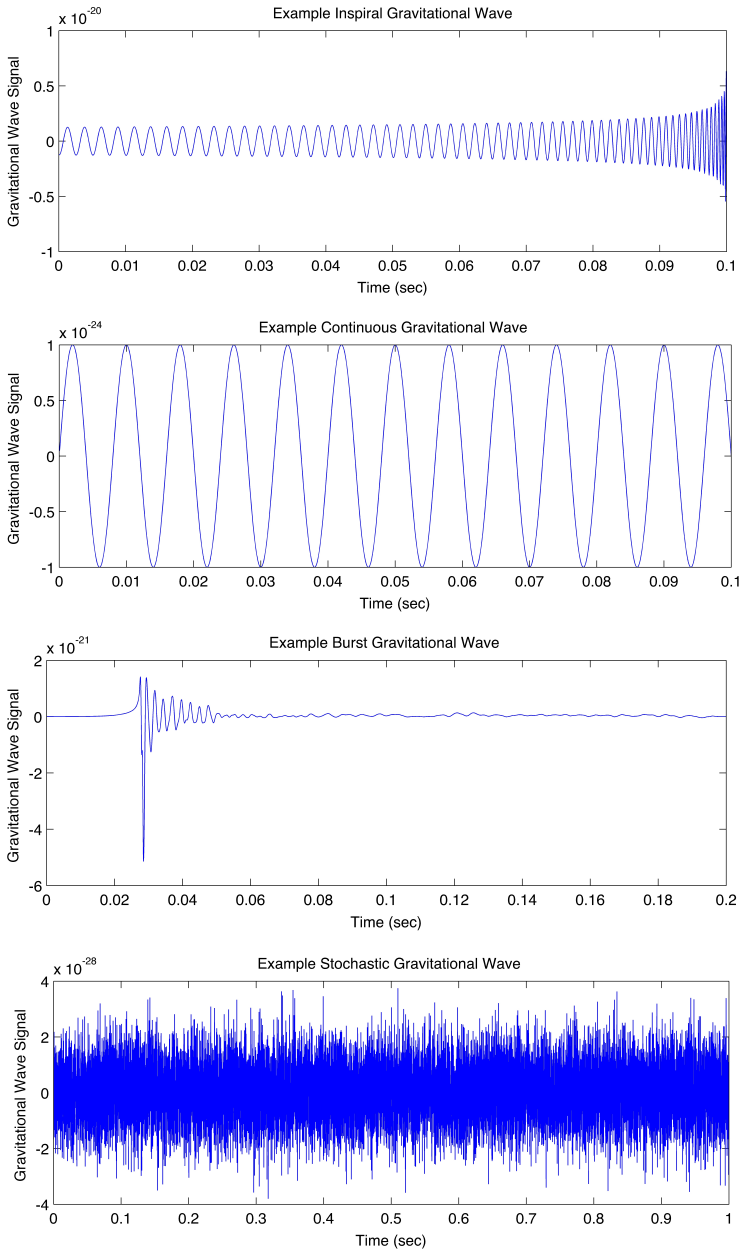

Figure 5.2 – Illustration from [109] of the different types of gravitational waves: inspiral (top), continuous (top-middle), burst (bottom-middle) and stochastic (bottom).

ern LIGO/Virgo detectors. There are different types of gravitational waves, which are illustrated in Figure 5.2:

- *Inspiral gravitational waves:* it is the only source of gravitational waves that has been detected. They are produced by the end of life of a binary system when two compact objects in quasi-circular orbit, coalesce to form a neutron star or a black

hole. The frequency f of the signal increases slowly until the merger and the first order of post-Newtonian expansion in power of v/c gives:

$$\frac{df}{dt} = \frac{96}{5}\pi^{8/3}\left(\frac{G\mathcal{M}}{c^3}\right)^{5/3} f^{11/3}\,, \tag{5.3}$$

where $\mathcal{M}$ is the chirp mass.

- *Continuous gravitational waves:* it is produced by a periodic system and the frequency of the signal is then constant. Well before the merger time, a binary system emits weak gravitational waves with frequency f equal to:

$$f = \frac{1}{\pi}\sqrt{\frac{m_1 + m_2}{a^3}} \tag{5.4}$$

with a the orbital separation, m_1 and m_2 the masses of the objects. The emission must be weak to avoid a back reaction from the system. Another example is a rotating star with a mountain at the surface.

- *Burst gravitational waves:* such waves are expected with gamma-ray bursts (GRBs) and can be produced by supernovae, but they can also be produced by unknown or unexpected sources and systems. After the inspiral gravitational waves, the merger of two neutron stars seems accompanied by short GRBs and will produce gravitational waves classified as bursts. In any case, their waveforms are not well known and their detections would improve the knowledge of the details of the emitting system.
- *Stochastic gravitational waves:* they have a priori two components. The first one is of cosmological origin with relic gravitational waves comparable to continuous noise in all sky localizations. Such a signal is analogous to the Cosmic Microwave Background and could have been created a few seconds after the Big-Bang. The discovery of such a signal could open the way to a new physics. The second is of astrophysical origin and comes from the set of gravitational wave sources having an intensity too weak to be detected individually [110]. It is similar to the diffuse infrared background produced by all unresolved optical sources. Such a signal depends on the stellar evolution, the evolution of galaxies, the cosmology, the distribution of binary systems etc.

5.4 Numerical Relativity and $3+1$ formalism

To calculate the gravitational wave-form emitted by a compact object merger, the Einstein equations must be solved:

$$R_{\mu\nu} - \frac{1}{2}g_{\mu\nu}R = 8\pi G T_{\mu\nu}\,. \tag{5.5}$$

Even in the case of a binary black hole merger where the source term is zero: $T_{\mu\nu} = 0$, there is no analytical solution. As illustrated in Figure 5.3, the gravitational wave-form is composed of three phases. The first one is called quasi-circular inspiral phase. In this phase, the two compact objects are far enough away to calculate the wave-form by a Post-Newtonian development [111]. The second phase is called plunge merger phase, it starts

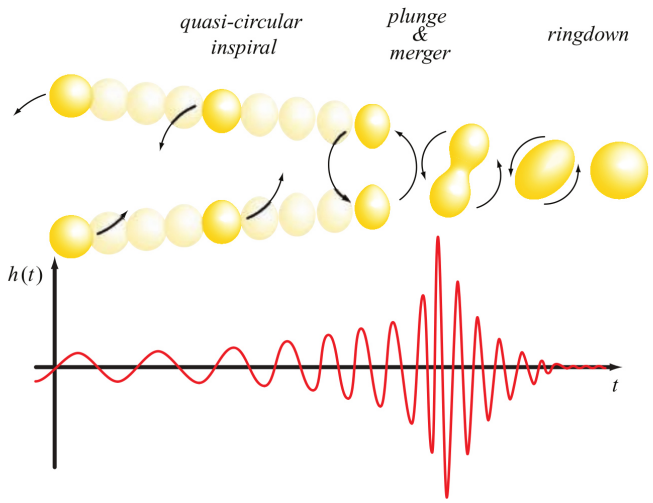

Figure 5.3 – The different phases of compact binary inspiral and coalescence (from Baumgarte and Shapiro, *Numerical Relativity: Solving Einstein's Equations on the Computer* [19])

when the two objects approach the innermost stable circular orbit and ends when the two objects form only one. This phase is the most complicated to describe and requires to fully solve the Einstein equations using Numerical Relativity. Finally, the object resulting from the merge is formed in an excited state and the last phase consists in a de-excitation of this object to form the Kerr metric. This phase is called ringdown and can be described by perturbation of the Kerr metric.

In the following, we will study in more detail the solution of Einstein's equations using the codes developed by the Einstein Toolkit community [18, 112]. To solve these equations numerically, they must be in a particular form. There are three main families: the hyperbolic equations $\partial_t^2\phi = \Delta\phi$, the elliptic equations $\Delta\phi = 0$ and the limit case with the parabolic equations $\partial_t\phi = \Delta\phi$. The parabolic equations are useful to describe diffusion phenomena like the diffusion of a drop of ink in water. By knowing the field ϕ at the initial state t_i over the whole space, it is possible to calculate ϕ at $t_i + \delta t$ and then ϕ at each instant by iteration. An example of elliptic equation is the Poisson equation $\Delta V = 0$ in electrostatics. To solve this equation over a space $\mathcal{V}$, we need to know the value of the field on the edge of the space $\partial\mathcal{V}$, and an algorithm generally called relaxation starts from an initial guess and converge to the right value of the field ϕ. Finally, the initial conditions for solving the hyperbolic equations describing for example the vibration of a string, are the knowledge of the field at each instant on the edge of the space and the knowledge of ϕ and $\partial_t\phi$ at the initial instant over the whole space. The methods of resolution and the approaches to solve numerically the equations are numerous and become more and more complex when there are systems of coupled nonlinear differential equations as it is the case for Einstein's equations (5.5). The problem with this current form is that they are a mixture of different types of equations and insoluble. Indeed, the left side of Einstein's

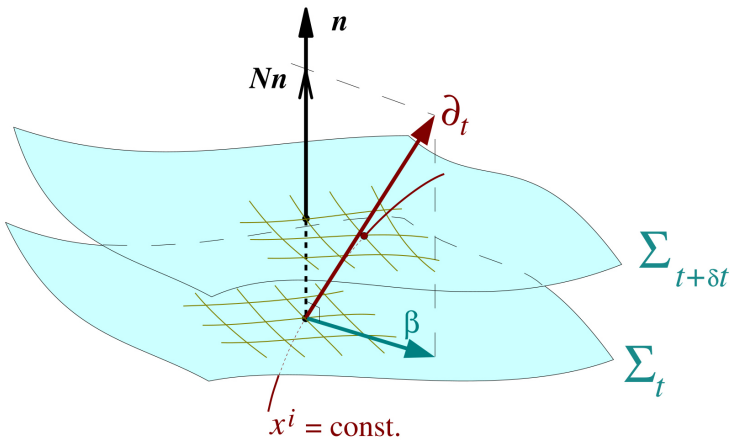

Figure 5.4 – Coordinates adapted to the foliation. Here N is the lapse function *alpha* (from Gourgoulhon, $3+1$ *formalism and bases of numerical relativity* [20])

equations is composed of $g_{\mu\nu}$, $\partial_\rho g_{\mu\nu}$, $\partial_\sigma \partial_\rho g_{\mu\nu}$ and we would like to impose at $t = 0$ the metric with its spacial derivatives in 3-dimension to be able to make it evolve.

To solve Eisntein's equations for a coalescence of compact objects, it is necessary to use the formalism $3+1$ which decomposes the spacetime into space + time [19, 20]. This approach allows to decompose the space-time $\mathcal{M}$ into a family of hypersurfaces Σ_t such that the sum of these hypersurfaces forms the whole spacetime. Thus, by giving the induced metric γ_{ij} ($\gamma_{ij} = g_{ij}$) on a slice Σ_t where t is constant, it will be possible to evolve it in order to compute the next slice $\Sigma_{t+\delta t}$. Conceptually, it is enough to know the following system of differential equations:

$$\begin{aligned} \partial_t \gamma_{ij} &= \dots , \\ \partial_t \dot{\gamma}_{ij} &= \dots . \end{aligned} \tag{5.6}$$

The unit vector normal to a slice Σ_t and oriented towards the future, noted $\boldsymbol{n}$ such that $\boldsymbol{n}.\boldsymbol{n} = -1$, can be written:

$$\boldsymbol{n} = -\alpha \vec{\boldsymbol{\nabla}} t \tag{5.7}$$

with α the lapse function. α is the normalization factor of $\vec{\boldsymbol{\nabla}} t$ which is the dual vector of the form $\boldsymbol{d}t$. Any vector of the space-time can be projected on the sub-vector space defined by $\boldsymbol{n}$ or on the vector space defined by the slice of the space-time. Moreover the shift vector $\boldsymbol{\beta}$ is defined by the following relation (see Figure 5.4):

$$\boldsymbol{\partial}_t = \alpha \boldsymbol{n} + \boldsymbol{\beta} \tag{5.8}$$

α and β represent the choice of the evolution of a slice in the space-time, that is to say to pass from a time t to a time $t + \delta t$. The metric $g_{\mu\nu}$ of the 4D space-time is equal to:

$$g_{\mu\nu} dx^\mu dx^\nu = -\alpha^2 dt^2 + \gamma_{ij}(dx^i + \beta^i dt)(dx^j + \beta^j dt) . \tag{5.9}$$

The projection of the Einstein's equations on the slice gives the following evolution equations [19]:

$$\begin{aligned}(\partial_t - \mathcal{L}_\beta)\,\gamma_{ij} &= -2\alpha K_{ij} \\ (\partial_t - \mathcal{L}_\beta)\,K_{ij} &= -D_i D_j \alpha + \alpha\left(R_{ij} + K K_{ij} - 2K_{ik}K^k_j\right)\end{aligned} \tag{5.10}$$

where K_{ij} is the extrinsic curvature tensor which replaces $\dot{\gamma}_{ij}$ of the equation (5.6), $\mathcal{L}_\beta$ is the Lie derivative along β and D is the connection associated with the metric γ_{ij}. The decomposition on $\boldsymbol{n}$ gives the Hamiltonian constraint and the mixed decomposition on $\boldsymbol{n}$ and on the slice gives the 3 momentum constraints:

$$\begin{aligned}\mathcal{H} &= R + K^2 - k_{ij}K^{ij} = 0\,, \\ \mathcal{M}^i &= D_j\left(K^{ij} - \gamma^{ij}K\right) = 0\,.\end{aligned} \tag{5.11}$$

This formulation of Einstein's equations coming from the decomposition of space-time into $3+1$, developed first by Georges Darmois in the 1920's [113], André Lichnerowicz in the 1930-40's [114] and Yvonne Fourès-Bruhat in the 1950's [115]. These equations are called "standard" $3+1$ equations and sometimes called "ADM" equations after Arnowitt, Deser and Misner [116]. Numerically, this formulation is not stable enough, the formulation used by the Einstein Toolkit community, for example, is the BSSN formulation [117, 118] which is an improved form of the ADM equations.

For a given slice of space-time, the resolution of the equations involves 12 undetermined initial data coming from (γ_{ij},K_{ij}) to which we have to subtract: the 4 constraints (Hamiltonian + Momentum) and the 4 choices of coordinates (α,β^i) [19]:

$$\underbrace{6+6}_{\substack{\text{independent}\\ \text{components}}} \quad \underbrace{-1-3}_{\substack{\text{constraint}\\ \text{equations}}} \quad \underbrace{-4}_{\substack{\text{coordinate}\\ \text{choice}}} \quad = \quad \underbrace{2\times 2}_{\substack{\text{two independent}\\ \text{sets of values}}} \quad . \tag{5.12}$$

Thus, there remain two independent sets of values which correspond to the degrees of freedom of the two gravitational wave polarizations.

5.5 Gravitational Wave-forms for binary black holes

To solve Einstein's equations numerically, the Einstein Toolkit [18, 95] releases core computational tools built on the Cactus [119] infrastructure allowing to realize parallel high performance computing. The Einstein Toolkit source code is divided into different modules called thorns. For example, the `ADMBase` thorn provides, among other things, the 12 evolution variables: the induced metric γ_{ij} and the extrinsic curvature K_{ij} with the lapse function α and the shift vector β^i. The parameter file for running a simulation with Einstein Toolkit must include all the parameters of the thorns used and looks like the sample below. In this example, there are two blocks: a first block sets the `ADMBase` evolution method and a second block that defines the choice of coordinates in the `ML_BSSN` thorn [120–122]. These parameters allow us to fix the $1+log$ slicing given by $F=2$ and $N=1$ in the following equation:

$$\partial_t \alpha = -F\alpha^N + \underbrace{1}_{\text{advectLapse}} \times \beta^i \partial_i \alpha \tag{5.13}$$

and the hyperbolic gamma driver that imposes:

$$\begin{aligned}\partial_t \beta^i &= \underbrace{3/4}_{\text{ShiftGammaCoeff}} \times B^i + \underbrace{1}_{\text{advectShift}} \times \beta^j \partial_j \beta^i \\ \partial_t B^i &= \partial_t \tilde{\Gamma}^i - \underbrace{1.0}_{\text{BetaDriver}} \times B^i + \underbrace{1}_{\text{advectShift}} \times \beta^j \partial_j \beta^i\end{aligned} \tag{5.14}$$

with $\tilde{\Gamma}^i$ the conformal connection functions [19]. To perform a merger of two black holes, one must also use the `TwoPunctures` thorn [123] which allows to define the initial conditions, the `AHFinderDirect` thorn [124] to compute at each instant the apparent horizon of the black holes, two other thorns to extract the decomposition of the Weyl scalar ψ_4 into $s = -2$ spin-weighted spherical harmonics, which is related to the gravitational wave polarization amplitudes by the following equation:

$$\ddot{h}_+ - i\ddot{h}_\times = \psi_4 = \sum_{l=2}^{\infty} \sum_{m=-l}^{l} \psi_4^{lm}(t,r)\, {}_{-2}Y_{lm}(\theta,\phi)\,. \tag{5.15}$$

and so on. A complete example of parameter file can be found on the Einstein Toolkit website [95]. It uses the different thorns described in [18, 120, 123–131]. To give an order of magnitude, a full run of such a code requires about 3 days on 128 cores.

```
##############
# Evolution #
##############
ADMBase::evolution_method         = "ML_BSSN"
ADMBase::lapse_evolution_method   = "ML_BSSN"
ADMBase::shift_evolution_method   = "ML_BSSN"
ADMBase::dtlapse_evolution_method = "ML_BSSN"
ADMBase::dtshift_evolution_method = "ML_BSSN"

ML_BSSN::harmonicN           = 1
ML_BSSN::harmonicF           = 2.0
ML_BSSN::ShiftGammaCoeff     = 0.75
ML_BSSN::BetaDriver          = 1.0
ML_BSSN::advectLapse         = 1
ML_BSSN::advectShift         = 1
##############
```

The result of a simulation of a binary black hole merger is plotted in Figure 5.5 with different snapshots. On the left, there is the gravitational wave-form and on the right the apparent horizon of the black holes. The natural units of the code are $G = c = M_T = 1$ where M_T is the total mass of the system. To plot Figure 5.5, the total mass has been chosen equal to $20M_\odot$ and the initial conditions are two spinless black holes of the same mass. The scaling relations will be studied in details in the next chapter with exotic black holes.

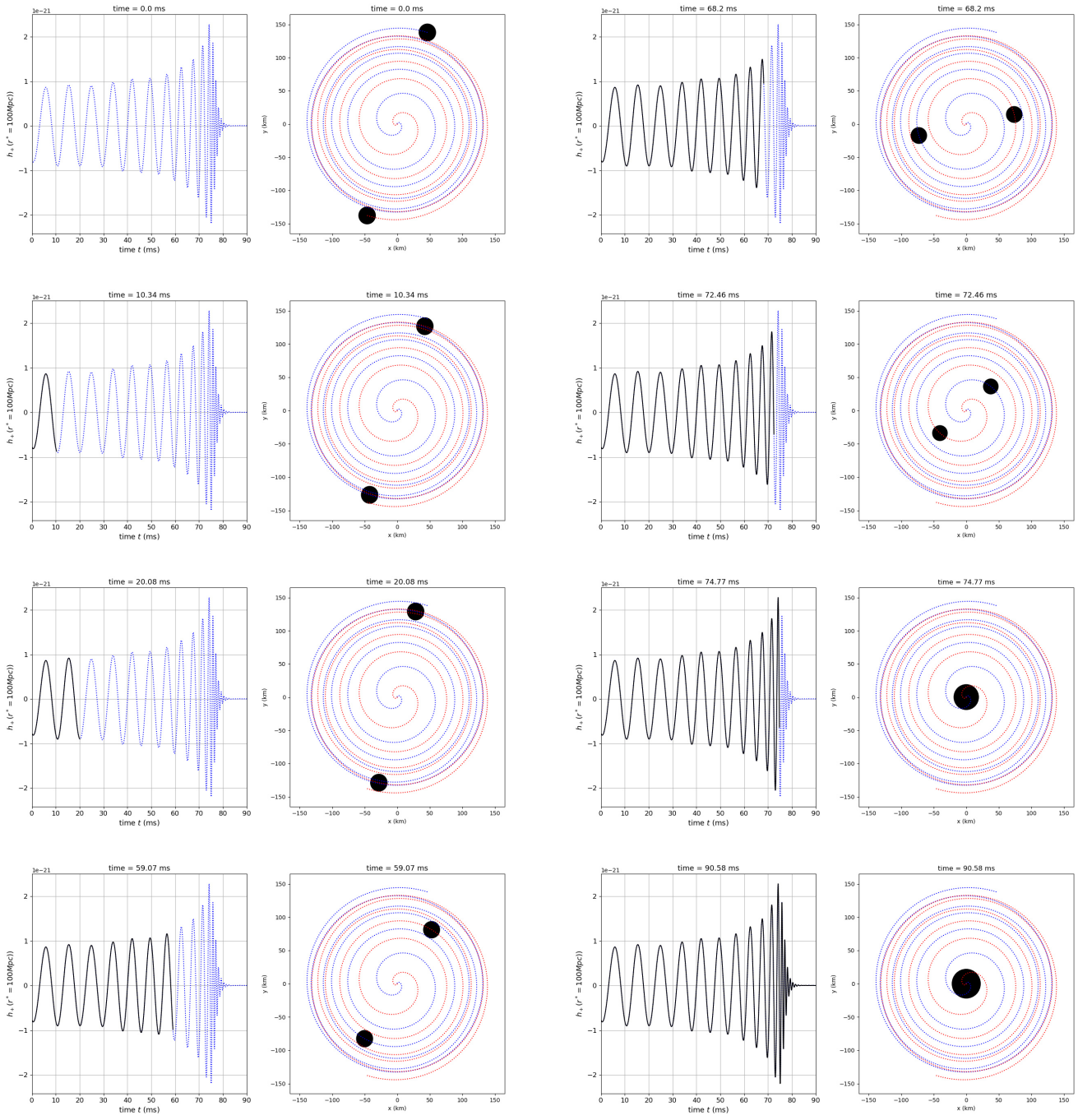

Figure 5.5 – Result of a merger of two black holes obtained with Einstein Toolkit. The different times of the merger are represented by the different figures. On the left, there is the gravitational wave-form and on the right the evolution of the apparent horizon of the black holes.

Thanks to many numerical simulations, libraries like `IMRPhenomPv2` [132–134] have been built to have access to the gravitational wave-form of a merger in an almost instantaneous way. It is also this type of templates that are used to extract gravitational waves from the noise of detectors. Even if the wave-forms are well tabulated for standard black holes, it is not yet the case, for example for 5 dimensional black holes.

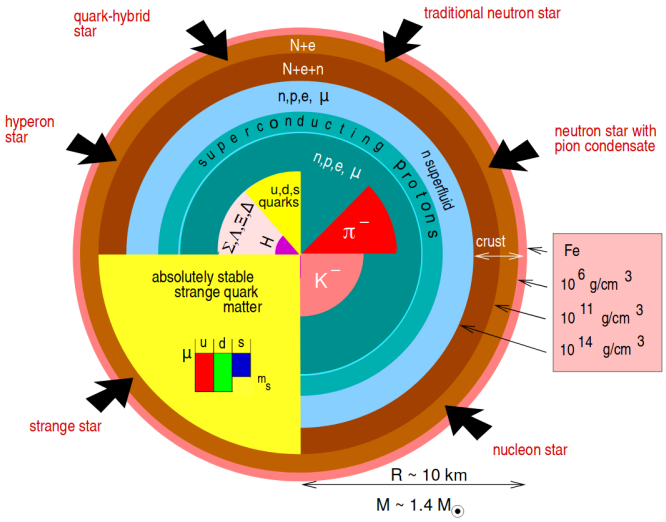

Figure 5.6 – Diagram showing competing structures to describe the interior of a neutron star from [137].

5.6 Gravitational Wave-forms for binary neutron stars

Obtaining the wave-form for a neutron star merger is much more complex because it involves hydrodynamic equations. In this case, the description of the matter must be taken into account with a non-zero energy-momentum tensor. At the beginning of the fusion, in the inspiral phase described by a post-Newtonian development, the composition of a neutron star is only involved at 5PN order by the quadrupole momentum characterized by the tidal deformability [111]. This tidal deformability has been measured for the first time by the LIGO/Virgo collaboration for the GW1708017 event [135]. To compute the complete wave-form, one must solve the Einstein equations with an equation of state that relates the density ρ to the pressure p. A first approach uses a polytropic equation of state: $p = K\rho^{\Gamma}$ with K and Γ two constants. A more realistic description involves a temperature dependent equation of state with a description of neutrino emission and reabsorption. In the following, we will start by describing different models of a neutron star. Then, using `Lorene` [136], initial conditions for binary neutron star mergers will be calculated. These configurations will be used by `WhiskyTHC` [96, 97] to evolve them and calculate the corresponding gravitational wave-forms.

5.6.1 NS description and initial data

Compared to the sun, a neutron star is slightly more massive, of the order of $1.4M_{\odot}$, but its radius is of the order of 10 km and thus far from the 696 340 km radius of the sun. The matter constituting a neutron star is therefore in extremely dense conditions. Figure 5.6 shows different possibilities of the state of matter in the core of such a star. As we can see, there is no consensus and these extreme conditions cannot be realized in laboratory to discriminate the models. But the observation of gravitational waves emitted by a neutron star merger, gives an opportunity to study the structure of a neutron star.

The web page `https://stellarcollapse.org/microphysics` gathers different equations of state that can be used to describe the matter of compact stars. Figure 5.7 shows the evolution of density ρ and pressure p as a function of enthalpy for two equations of state called: LS220 [138] and DD2 [139]. These equations of state can be used to solve the Einstein equations to describe a rotating relativistic star. The energy density profile is plotted for these two equations of state at the bottom right of Figure 5.7 for a $1.45 M_{\odot}$ non-rotating star. This profile has been obtained using the `nrotstar` routine of `Lorene` solving the equations of general relativity in a stationary and axisymmetric space [140]. The circumferential equatorial radius R_c of the stars is close to 13 km. To calculate these profiles, the code uses as input the central value of the enthalpy, in this example, it is approximately equal to 0.2 which gives a gravitational mass of $1.45 M_{\odot}$. The core of the neutron star corresponds to the region where the two equations of state are similar. To realize an initial configuration for a neutron star merger, it is not enough to juxtapose two neutron stars distant of 50 km, indeed, a slice of space-time must verify the Hamiltonian and Momentum constraints and be in co-rotation. On the other hand, such a juxtaposition is a good starting point to compute an initial configuration that can be used by evolution codes. The initial conditions for a binary neutron star merger can be calculated by another routine of `Lorene` [136]. The result given by this routine can be easily used as an initial condition by Eintein Tollkit thanks to the thorn `EinsteinInitialData/Meudon_Bin_NS` which directly takes the result of `Lorene` to initialize the slice of space-time. Recently [141],a new public code for initial data compact-object binaries is available and allows to consider more general cases with neutron stars having an intrinsic spin parallel to the orbit. Moreover, the solver supports extreme mass ratio and spin asymmetries. In the following part, the evolution of three initial conditions, calculated by `Lorene`, will be realized by `WhiskyTHC` whose results are shown in Figure 5.8, Figure 5.9 and Figure 5.10.

The nuclear equations of state to describe the state of matter of a neutron star are numerous, LS220 and DD2 are only two examples among many others. The meta-model [142], developed at the IP2I of Lyon, allows to reproduce all the well known equations of state of nuclear physics. This model is based on the expansion of the nuclear empirical parameters (E_{sat}, L_{sym}, ...) around the saturation density. By imposing the beta equilibrium, the high density extrapolation of such an expansion, up to 2-5 times the saturation density, allows to describe the matter of a neutron star. In this model, a neutron star consists of three distinct but coherent regions. These regions are called: outer crust, inner crust and core. The outer crust is composed of free electrons and nucleons described by the liquid drop model, protons and neutrons are bound. In the inner crust, there are also free neutrons. The core contains free electrons, muons, protons, neutrons and there are no more bound protons and neutrons.

5.6.2 Evolution

After the first detection of the binary neutron star merger GW170817 by LIGO/Virgo, it has become crucial to have accurate descriptions of such events, to be able to compare them with gravitational waves and optical observations. `WhiskyTHC` [96] is the merger of the `Whisky` [143] and `THC` [144] codes that allows to solve fully general-relativity hydrodynamics in high-order codes. Its infrastructure is based on Einstein Toolkit and solves the CCZ4 for-

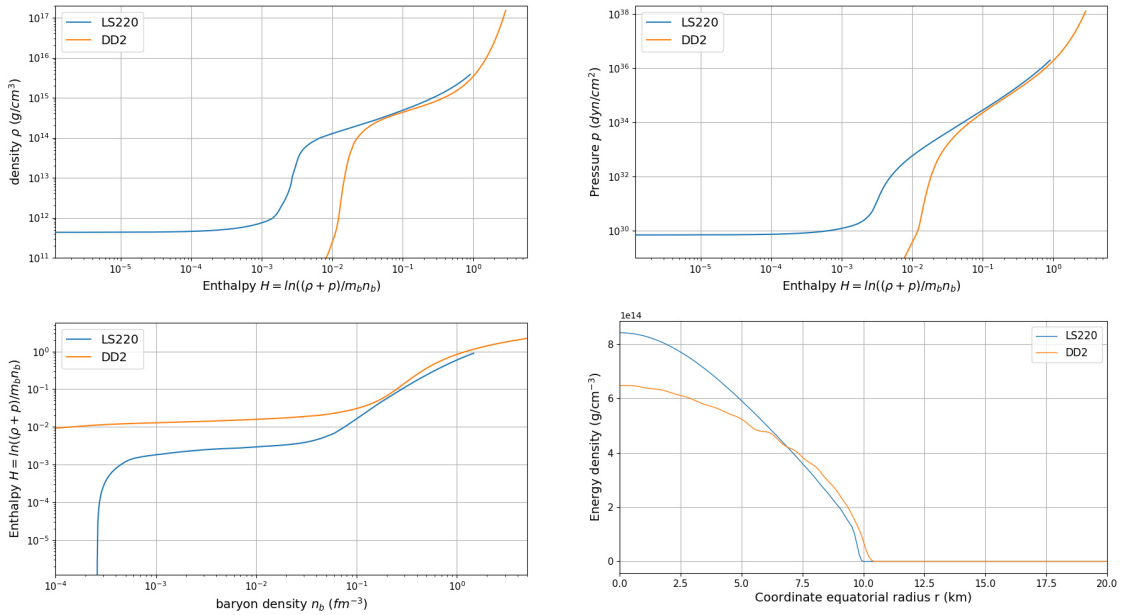

Figure 5.7 – Representation of the equation of state LS220 in blue and DD2 in orange. Top: evolution of density and pressure as a function of enthalpy. Bottom left: evolution of enthalpy as a function of baryon density. Bottom right: energy density profile of a $1.45 M_\odot$ neutron star.

mulation [145] of the Einstein equations. `WhiskyTHC` supports tabulated three-dimensional equations of state with a treatment of neutrinos based on gray leakage scheme [146]. The variables of the equations of state should be the energy density, temperature and electron fraction. The evolution of the electron fraction is done by treating the neutrino emission and absorption. A detailed study of mass ejection, electromagnetic counterparts and nucleosynthesis in neutron star merges has been done in [147] using `WhiskyTHC`.

Figures 5.8, 5.9 and 5.10 show the merger of two neutron stars of the same masses. Each figure gathers several snapshots of the simulation. On the right of each snapshot, there is a xy slice showing the energy density and on the left, there is the plot of the gravitational wave calculated at a distance of 400 Mpc. The blue dashed curve represents the total h_+ amplitude of the wave-form while the black curve shows the emission of the gravitational wave-form over time. Before the merger of the two neutron stars, the wave-form is very similar between the different simulations and is very well described by a post-Newtonian development. It is almost independent of the equation of state: it is the inspiral phase. On the other hand, at merger time, three behaviors are clearly distinguished according to the compact object formed by the fusion. In Figure 5.8, for the equation of state LS220 with two $1.5 M_\odot$ neutron stars, there is a collapse of the system into a black hole very quickly after the merger. For the same equation of state but with neutron stars of $1.35 M_\odot$, there is formation of a kilonava several milliseconds before the collapse into a black hole. During this phase, the frequency of the gravitational wave is much higher than during the inspiral phase and its amplitude is lower. Unfortunately, this part of the

gravitational wave very rich to study the structure of the matter falls for the moment in the noise of the LIGO/Virgo detectors. Finally, for the DD2 equation of state with two neutron stars of $1.45 M_{\odot}$, the resulting object is a neutron star, so there is no black hole collapse.

The description of matter under the extreme conditions of the interior of neutron stars is not well known yet. In particular, are there phase transitions? Is the core of neutron stars made up of quark-gluon plasma? Thus, the study of neutron star mergers could help answering such questions. Performing these simulations with the LS220 and DD2 equations of state is the first step to further investigate these issues. A systematic study with many equations of state would allow to better know the conditions under which a kilonava is formed. This would also improve the templates of the gravitational wave-forms used by the LIGO/Virgo collaboration in the Bayesian analysis. Moreover, it is not only the gravitational wave-form that can be studied. Indeed, understanding the formation of heavy nuclei in this type of system is crucial and must be studied, etc.

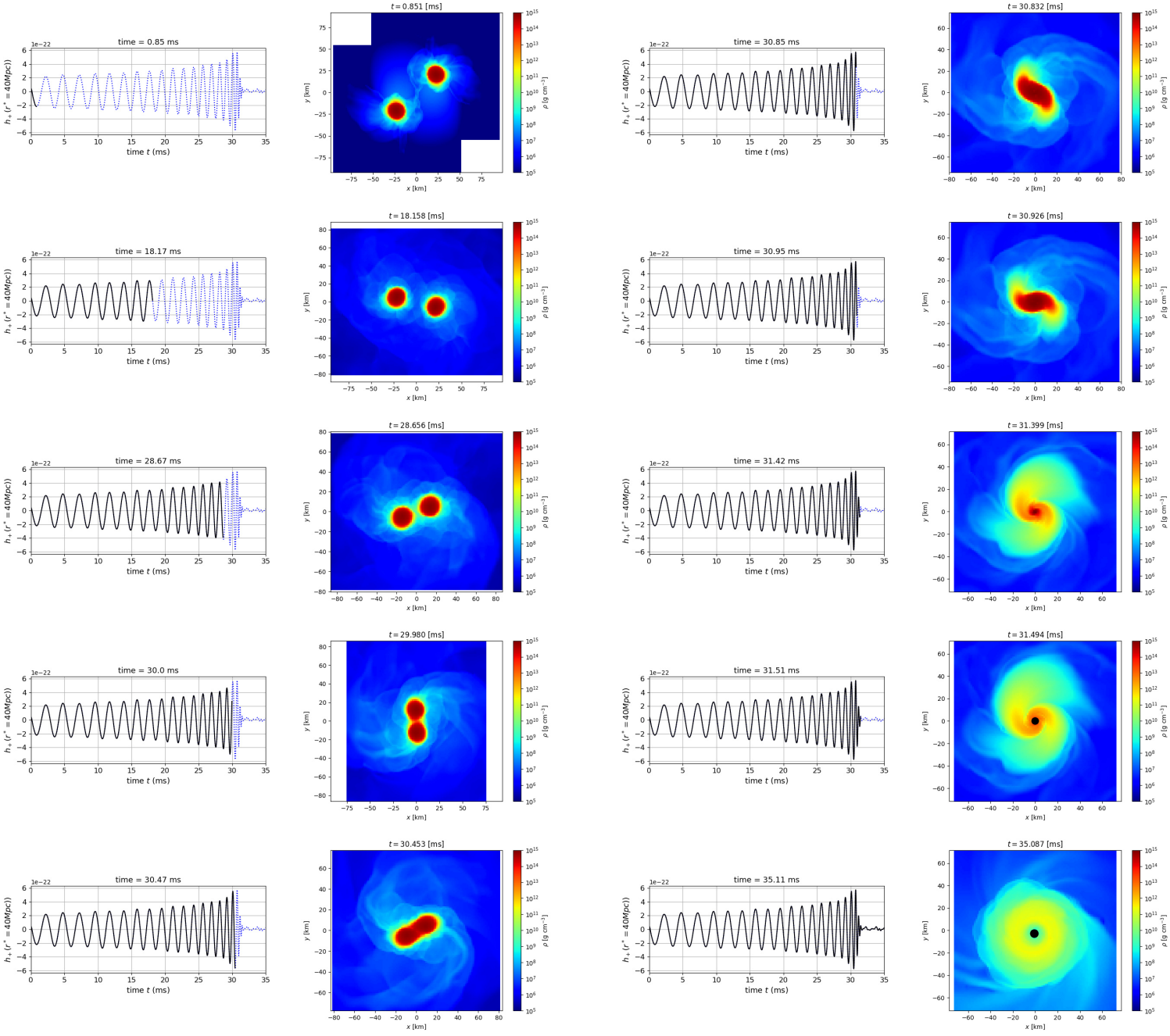

Figure 5.8 – Result of a simulation representing the merger of two neutron stars of $1.5 M_\odot$ realized by `WhiskyTHC` considering LS220 as equation of state.

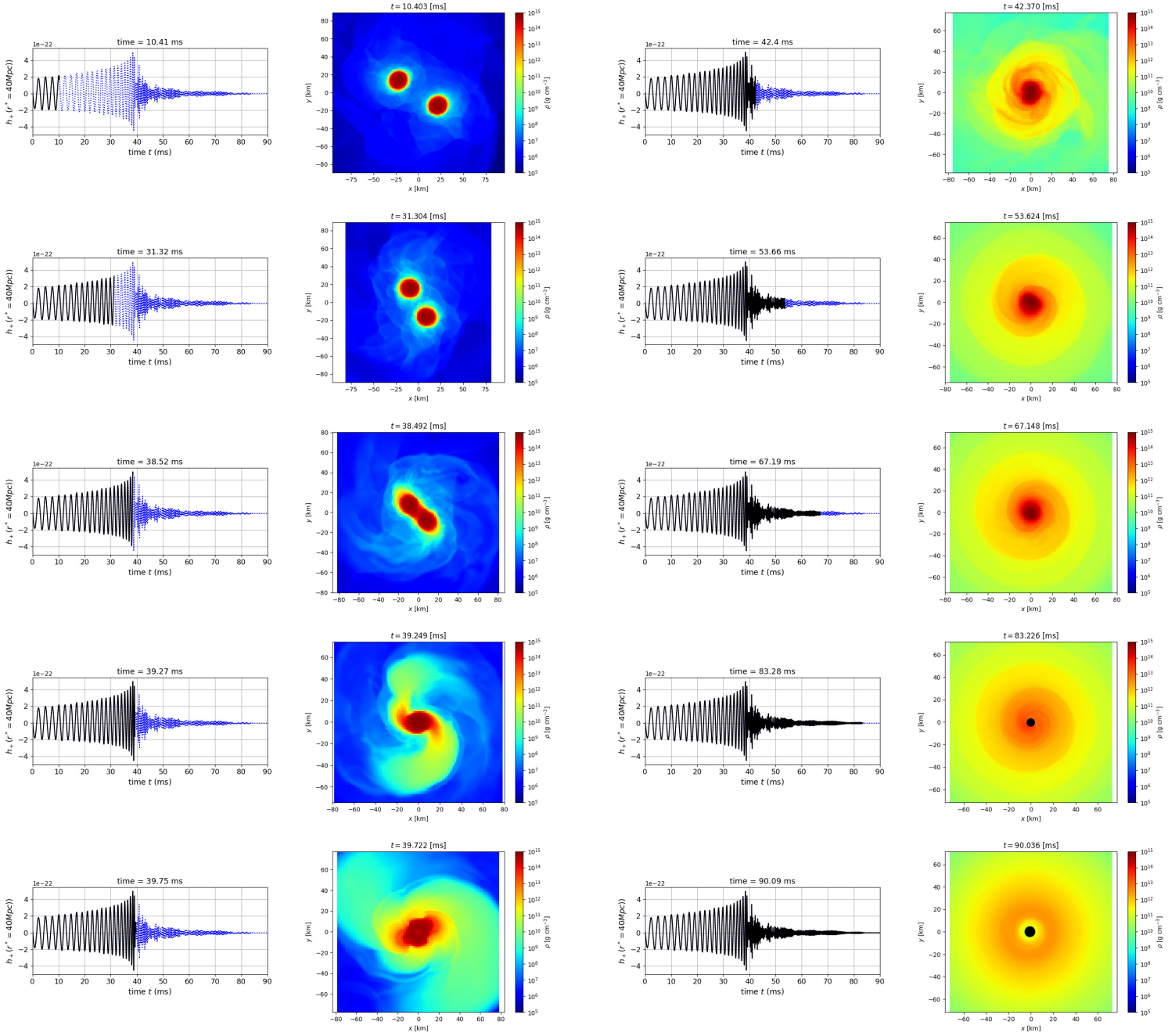

Figure 5.9 – Result of a simulation representing the merger of two neutron stars of $1.35 M_{\odot}$ realized by `WhiskyTHC` considering LS220 as equation of state.

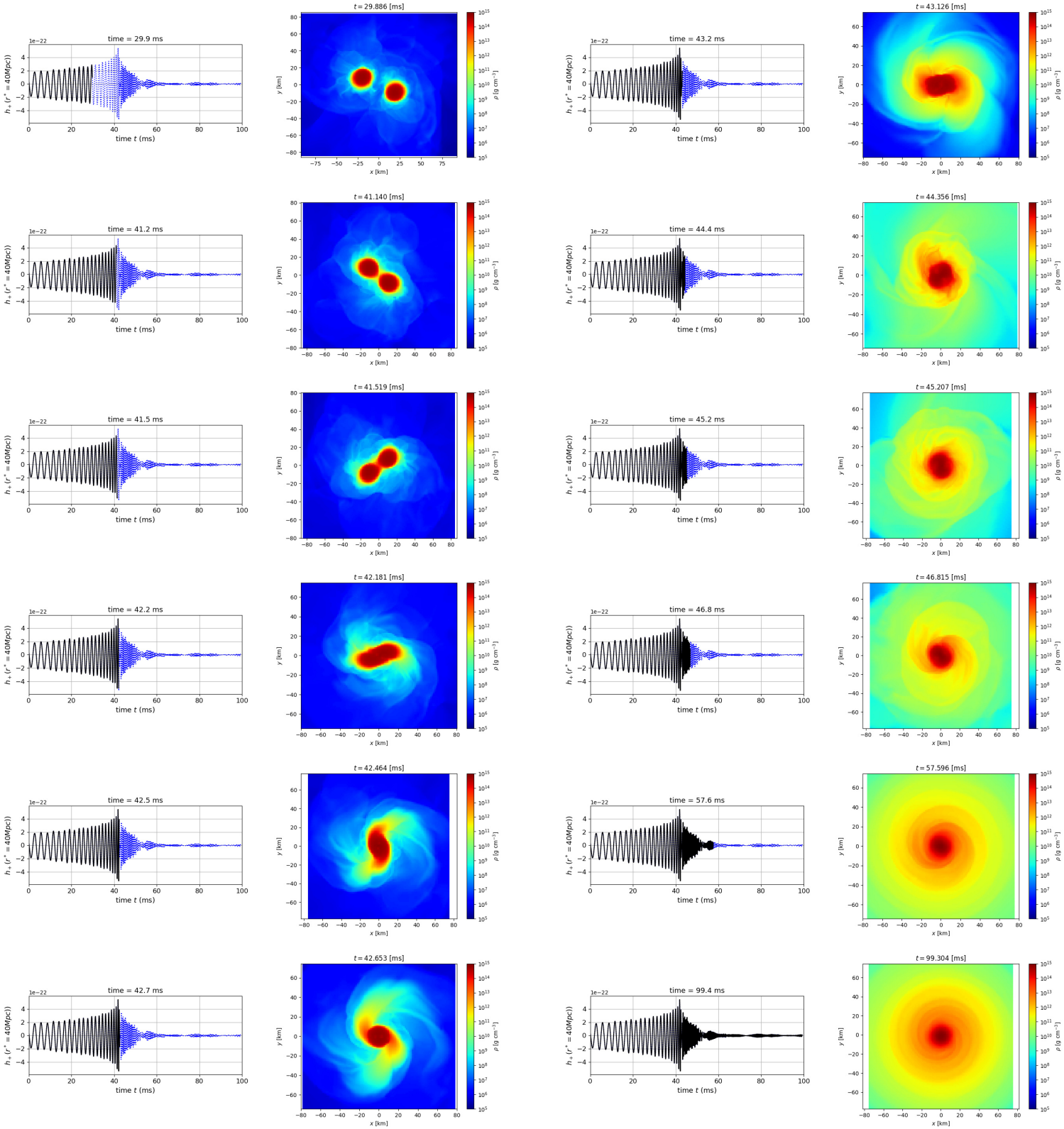

Figure 5.10 – Result of a simulation representing the merger of two neutron stars of $1.45 M_\odot$ realized by `WhiskyTHC` considering DD2 as equation of state.

6

Scaling relations

Observations of gravitational waves provide new opportunities to study our Universe. In particular, mergers of stellar black holes are the main targets of the current gravitational wave experiments. In order to make accurate predictions, it is however necessary to simulate the mergers in numerical general relativity, which requires high performance computing. While scaling relations can be used to rescale simulations for very massive black holes, non-standard black holes have specific properties which can invalidate the rescaling. In this article, we study the scaling relations of general classes of black holes, including primordial black holes affected by the cosmological expansion and Hawking evaporation.

Contents

6.1 Introduction

After the discovery of gravitational waves (GWs) by LIGO [10], studies of mergers of stellar mass black holes (BHs) and of the resulting emission of gravitational waves have multiplied, either with semi-analytical descriptions or with numerical general relativity simulations. In absence of discovery of new particles at the LHC and in dark matter detection experiments, the nature of dark matter is still actively searched for, and the fact that primordial black holes (PBHs) can constitute dark matter is now considered as a viable possibility [5, 148, 149]. Contrary to stellar black holes, the mass of primordial black holes spans from values as low as the Planck mass up to millions of solar masses, and the merger of such PBHs can generate GWs with frequencies and amplitudes very different from those accessible to LIGO and VIRGO. Yet such PBH-generated GWs may be accessible to future GW experiments such as LISA [150], and it is important to correctly model them. However because the masses of the involved PBHs can be very different from the stellar BHs for which numerical simulation codes have been built, it may be very difficult to simulate numerically their mergers, and in particular the final states, which requires numerical simulations for a correct description. Fortunately there exists scaling relations which can in principle be used to rescale results obtained in numerical simulations of stellar BH mergers to very different mass scales and which also apply to GW emission. Nevertheless, some particularities of the primordial black holes, such as very small masses, maximal spins, non-negligible charges and Hawking evaporation, can falsify such scaling relations. Besides, non-standard black hole models also have specific scaling properties. In this paper, we study how the scaling properties can then be used to distinguish between black hole models. In Section 6.2 we explicitly retrieve the scaling relations of standard black holes and derive scaling relations for a more general case, i.e. Kerr-Newman black holes with spin and electromagnetic charge. In Section 6.3 we discuss the domain of validity of such a rescaling, taking into account Hawking evaporation and expansion of the Universe. In Section 6.4, we study whether non-standard models of black holes can also have specific scaling properties. In Section 6.5, we consider the limitations of numerical simulations of black hole mergers in the case where the standard scaling properties are not valid and discuss the advantages of identifying new scaling relations, before concluding.

In the following, we use the natural unit system with $c \equiv 1$.

6.2 Scale invariance of standard black holes

6.2.1 Scale invariance

In the coordinate system $x^\mu = (t, x, y, z)$ associated to a metric $g_{\mu\nu}$, we consider a transformation with a scale factor λ such as

$$x^\mu \longrightarrow \lambda x^\mu \,. \tag{6.1}$$

By definition of the metric and its relation with the local flat coordinates, the metric is scale invariant under transformation (6.1). Under this transformation, we obtain for the proper time τ, Christoffel symbol $\Gamma^{\sigma}_{\mu\nu}$ and Riemann tensor $R^{\sigma}{}_{\mu\nu\kappa}$:

$$\begin{aligned} d\tau^2 &= g_{\mu\nu}dx^\mu dx^\nu \longrightarrow \lambda^2 d\tau^2\,, \\ \Gamma^{\sigma}_{\mu\nu} &= \frac{1}{2}g^{\sigma\alpha}\left(\frac{\partial g_{\alpha\mu}}{\partial x^\nu}+\frac{\partial g_{\alpha\nu}}{\partial x^\mu}-\frac{\partial g_{\mu\nu}}{\partial x^\alpha}\right) \longrightarrow \lambda^{-1}\Gamma^{\sigma}_{\mu\nu}\,, \\ R^{\sigma}{}_{\mu\nu\kappa} &= \frac{\partial\Gamma^{\sigma}_{\mu\kappa}}{\partial x^\nu}-\frac{\partial\Gamma^{\sigma}_{\mu\nu}}{\partial x^\kappa}+\Gamma^{\sigma}_{\mu\alpha}\Gamma^{\alpha}_{\mu\kappa}-\Gamma^{\sigma}_{\kappa\alpha}\Gamma^{\alpha}_{\mu\nu} \longrightarrow \lambda^{-2}R^{\sigma}{}_{\mu\nu\kappa} \end{aligned} \tag{6.2}$$

In addition the four velocity vector $u^\mu = dx^\mu/d\tau$ is scale invariant, and the Ricci tensor $R_{\mu\nu}$, the scalar curvature R and the Weyl conformal tensor $C_{\sigma\mu\nu\kappa}$ scale similarly to the Riemann tensor $R^{\sigma}{}_{\mu\nu\kappa}$. The geodesic equation

$$\frac{d^2x^\mu}{d\tau^2}+\Gamma^{\mu}_{\alpha\beta}\frac{dx^\alpha}{d\tau}\frac{dx^\beta}{d\tau}=0 \tag{6.3}$$

is also scale invariant, and therefore its solutions are unchanged and only the coordinates are dilated.

Concerning Einstein's field equations (EFEs) with a cosmological constant Λ and a stress-energy tensor $T_{\mu\nu}$:

$$R_{\mu\nu}-\frac{1}{2}g_{\mu\nu}R+\Lambda g_{\mu\nu}=8\pi G\,T_{\mu\nu}\,, \tag{6.4}$$

it is clear that the EFEs are not scale invariant. Indeed the cosmological constant is not scale invariant, neither is $T_{\mu\nu}$ in the general case. The scale invariance is retrieved in absence of cosmological constant and in the vacuum.

The description of the merger of black holes and generation of gravitational waves fulfils the scale-invariance condition: the GWs are perturbations of the metric in the vacuum, and the BHs are described as metrics with horizons. In absence of matter outside the BHs, the EFEs are written in the vacuum, and the cosmological constant is too small to have any effect during the black hole coalescence and merger. Let us consider the Kerr metric [151] in the Boyer–Lindquist coordinates [152], which describes a rotating black hole of mass M and angular momentum J:

$$d\tau^2=\left(dt-a\sin^2\theta d\phi\right)^2\frac{\Delta}{\Sigma}-\left(\frac{dr^2}{\Delta}+d\theta^2\right)\Sigma-\left((r^2+a^2)d\phi-adt\right)^2\frac{\sin^2\theta}{\Sigma}\,, \tag{6.5}$$

where (r,θ,ϕ) are spherical coordinates, $a=J/M$, $\Sigma=r^2+a^2\cos^2\theta$, $\Delta=r^2-R_s r+a^2$ and $R_s=2GM$ the Schwarzschild radius. In the case of vanishing angular momentum, the Schwarzschild metric is retrieved:

$$d\tau^2=\left(1-\frac{2GM}{r}\right)dt^2-\left(1-\frac{2GM}{r}\right)^{-1}dr^2+r^2(d\theta^2+\sin^2\theta d\phi^2)\,. \tag{6.6}$$

The scale invariance of the Kerr metric implies that:

$$R_s \longrightarrow \lambda R_s \iff M\longrightarrow\lambda M\,, \tag{6.7}$$

$$a\longrightarrow\lambda a \iff J\longrightarrow\lambda^2 J\,, \tag{6.8}$$

under transformation (6.1). The transformation of J is compatible with the standard definition of angular momentum $\vec{J} = m\,\vec{x} \times \vec{v}$ when applying the coordinate and mass transformations (6.1) and (6.7). Also the Kerr dimensionless spin parameter $a^* = a/M$, which is equal to 0 for Schwarzschild BHs and 1 for extremal Kerr BHs, is scale invariant.

We can now derive the following scaling rules for the merger of n BHs of masses M_i, spins J_i and momentum $\vec{P}_i$ with positions $\vec{x}_i$ $(i = 1 \cdots n)$ at time t:

$$\begin{aligned} M_i &\longrightarrow \lambda M_i \quad , & t &\longrightarrow \lambda t\,, \\ \vec{P}_i &\longrightarrow \lambda \vec{P}_i \quad , & \vec{x}_i &\longrightarrow \lambda \vec{x}_i\,, \\ J_i &\longrightarrow \lambda^2 J_i \quad , & a_i^* &\longrightarrow a_i^*\,. \end{aligned} \tag{6.9}$$

Consequently the local densities scale as $\rho \longrightarrow \lambda^{-2}\rho$, the accelerations as $\vec{a} \longrightarrow \lambda^{-1}\vec{a}$ and the velocities are scale invariant.

Similarly, since gravitational waves can be considered as perturbations of the metric, their frequency f, wavelength Λ, energy E, amplitude (or metric perturbation) h, speed v and stress-energy tensor scale as

$$\begin{aligned} f &\longrightarrow \lambda^{-1} f \quad , & \Lambda &\longrightarrow \lambda \Lambda\,, \\ E &\longrightarrow \lambda E \quad , & h &\longrightarrow h\,, \\ v &\longrightarrow v \quad , & T^{\mu\nu} &\longrightarrow \lambda^{-2} T^{\mu\nu}\,. \end{aligned} \tag{6.10}$$

6.2.2 Scaling relations of charged spinning black holes

While stellar black holes are generally expected to have small spins and negligible electromagnetic charges, primordial black holes can have very small masses, extremal spins and be strongly charged. In particular, the lifetime of primordial black holes can be strongly increased by an electromagnetic charge [153], making possible the existence of the very light ones even today.

In the general case, primordial BHs have to be described by the Kerr-Newman metric [154], which is similar to Eq. (6.5), with $\Sigma = r^2 - R_s r + a^2 + R_Q^2$, where R_Q is related to the black hole charge Q by

$$R_Q = \sqrt{\frac{G}{4\pi\epsilon_0}}\,Q\,, \tag{6.11}$$

with ϵ_0 the void permittivity. The scale invariance can be restored by transforming the charge as

$$Q \longrightarrow \lambda Q\,. \tag{6.12}$$

However, such a rotating charge induces an electromagnetic potential such as

$$A_\mu = \left(\frac{r R_Q}{\Sigma}, 0, 0, -\frac{a^* R_Q r \sin^2\theta}{\Sigma G}\right)\,, \tag{6.13}$$

which is invariant under our set of transformations. The electromagnetic field therefore transforms as

$$F_{\mu\nu} = \frac{\partial A_\nu}{dx^\mu} - \frac{\partial A_\mu}{dx^\nu} \longrightarrow \lambda^{-1} F_{\mu\nu}\,, \tag{6.14}$$

and the associated stress-energy tensor as

$$T^{\mu\nu} = \epsilon_0 \left(F^{\mu\alpha} g_{\alpha\beta} F^{\nu\beta} - \frac{1}{4} g^{\mu\nu} F_{\delta\gamma} F^{\delta\gamma} \right) \longrightarrow \lambda^{-2} T^{\mu\nu} \,, \tag{6.15}$$

which is the behaviour required to let the EFEs invariant in presence of a source term. Turning to Maxwell's equations:

$$\frac{\partial}{dx^\nu} \left(\sqrt{-\det(g_{\mu\nu})} g^{\mu\alpha} F_{\alpha\beta} g^{\beta\nu} \right) = \frac{J^\mu}{\epsilon_0} \,, \tag{6.16}$$

they are invariant when the current four-vector J^μ is zero or scales as λ^{-2}. Therefore, not only a Kerr-Newman BH respects the scaling relation described in Section 6.2.1 and charge normalized to the BH mass Q/M is scale invariant, but the electromagnetic waves emitted by a merger of charged black holes in empty space respect the same scaling properties as gravitational waves, given in Eq. (6.10). There is indeed a strong parallel between Einstein's field equations and Maxwell's equations: in presence of source terms the scaling properties are generally broken.

As a consequence, any simulation of charged spinning black holes can be rescaled to larger or smaller masses, and the gravitational waves and the electromagnetic waves can be rescaled similarly.

6.3 Domain of validity of the scaling relations for primordial black holes

Primordial black holes are by definition created in the primordial Universe, and can have masses as low as the Planck mass. With such small masses, quantum effects have to be taken into account, and interaction of the horizon of light black holes with the vacuum results in the BH evaporation by emission of particles, called Hawking radiation [155]. In the following, we study the domain of validity of the scaling relation with respect to surrounding material acting as source terms, expansion of the Universe and evaporation of BHs.

6.3.1 Surrounding material around black holes

Let us briefly consider the presence of source terms in the EFEs. For a perfect fluid in thermodynamic equilibrium, the stress-energy tensor reads:

$$T^{\mu\nu} = (\rho + P) u^\mu u^\nu + P g^{\mu\nu} \,, \tag{6.17}$$

where ρ and P are the energy density and pressure of the fluid. In order to leave the EFEs scale invariant, the energy density and pressure need to transform under the scale transformation as:

$$(\rho, P) \longrightarrow \lambda^{-2} (\rho, P) \,. \tag{6.18}$$

Such a transformation does not hold in the general case, but it is valid for collisionless particles with negligible pressure, or when $P \propto \rho$, or when both pressure and density are negligibly small. This has been studied numerically for example in [156, 157].

In the general case, when processes dominated by electromagnetic, weak or strong interactions occur the scaling is broken, because these interactions are related to different couplings, and in addition weak and strong interactions have limited ranges. Similarly, quantum effects cannot be expected to be scale-invariant since they are independent from gravity.

6.3.2 Black holes and expansion rate of the Universe

Since PBHs originate in the early Universe, their mergers can be affected by the expansion. As the expansion is time-dependent but affects space, it breaks the scaling of time and space. A simple rule would be to consider that a rescaling is possible as long as the duration of the merger $T_{\rm merger}$ is much smaller than the Hubble time $t_{\rm Hubble}(t)$ at cosmological time t, that is

$$T_{\rm merger} \ll t_{\rm Hubble}(t) \left[\equiv \frac{a(t)}{\dot{a}(t)}\right] , \tag{6.19}$$

where $a(t)$ is the cosmological scale factor. To calculate the merger time, we approximated the trajectory of the BHs to an equilibrium circular orbit with an orbital decay rate $dD(t)/dt$. At lowest order, this expression can be calculated from the quadrupole formula [19] and an integration of the orbital decay gives, for the binary separation distance $D(t)$ of the coalescence of two Schwarzschild BHs of Schwarzschild radius R_s, the following scale invariant expression:

$$D(t) = 4\left[\frac{R_s^3}{20}(T_{\rm merger} - t)\right]^{1/4} , \tag{6.20}$$

which is valid at $t < T_{\rm merger}$. Assuming a ΛCDM model in a flat Universe, using the cosmological parameters measured by Planck [2] and considering 60 e-folds for inflation, we show in Figure 6.1 the individual BH masses of binary mergers for which $T_{\rm merger} = t_{\rm Hubble}(t)$, as a function of the age of the Universe t. BHs with masses above the lines merge faster than the expansion. The line corresponding to the maximal PBH mass has been obtained by assuming that the biggest BH has a Schwarzschild radius equal to the Hubble radius. In particular, at our present epoch, mergers of stellar black holes are affected by the expansion only if their initial distance is larger than about 10^6 km.

6.3.3 Black holes and Hawking evaporation

Light PBHs are expected to vanish via emission of Hawking radiation [155]. Since the lifetime of a BH is typically proportional to its mass cubed [158], the scaling of the mass proportionally to the spacetime scaling is not possible anymore. Therefore, the scaling can be applied only if the duration of the merger is much smaller than the lifetime of the BHs. In Figure 6.2 we show the evaporation time of BHs as a function of their mass, for Schwarzschild BHs and for nearly extremal Kerr BHs with $a^* = 0.99$. The evaporation time has been computed with the public program `BlackHawk` [159]. For comparison, typical durations of mergers of two black holes obtained from Eq. (6.20) are also plotted as a function of the mass of the system, assuming that both BHs have identical masses, for

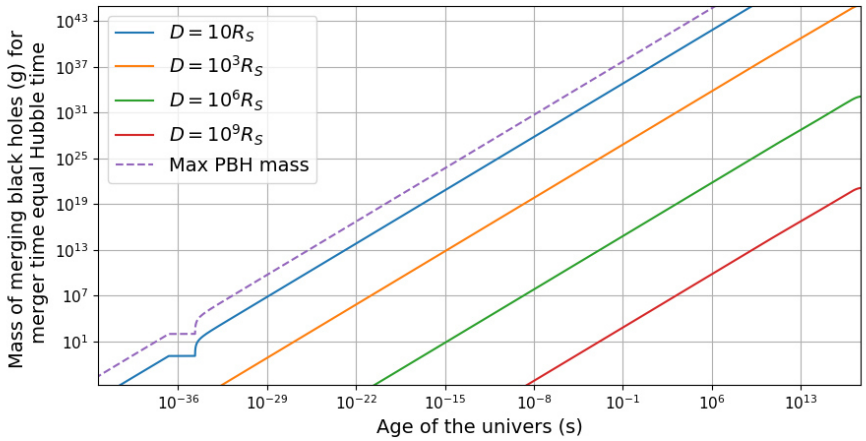

Figure 6.1 – BH masses corresponding to a merger time equal to the Hubble time, as a function of the age of the Universe, for different initial merger BH distances D given as numbers of Schwarzschild radii. The dashed line corresponds to the maximum mass of BHs.

initial distances $D = (10\,R_s, 10^3\,R_s, 10^6\,R_s, 10^9\,R_s)$, so that the rescaling is typically correct down to masses of about $(10^{-4}, 1, 10^6, 10^{12})$ grams, respectively, below which evaporation has to be taken into account and breaks the rescaling. Since PBHs having not completely evaporated today have masses above $10^{14}\,\mathrm{g}$ [160, 161], the mergers of the surviving PBHs are not affected by Hawking evaporation.

6.4 Non-standard black holes

In this section, we study the scaling properties of non-standard black holes, which can either be extensions of the Schwarzschild black hole model within Einstein-gravity, or black holes in non-standard gravity theories. In the latter case, not only the generation of gravitational waves during a black hole merger can be modified, but the propagation of the gravitational waves itself can be affected. Nevertheless, since the propagation of gravitational waves mostly occurs in a weak gravitational field and the observed gravitational waves are in agreement with general relativity, we will disregard the modification of propagation in weak gravitational fields and mainly discuss the scaling properties of non-standard black holes and gravity scenarios.

6.4.1 Black holes in expanding Universe

We first consider the McVittie metric [162], which describes a non-spinning and neutral black hole in a flat expanding Universe:

$$d\tau^2 = \left(\frac{1-\mu}{1+\mu}\right)^2 dt^2 - (1+\mu)^4 a^2(t)(d\rho^2 + \rho^2\, d\Omega^2)\,, \tag{6.21}$$

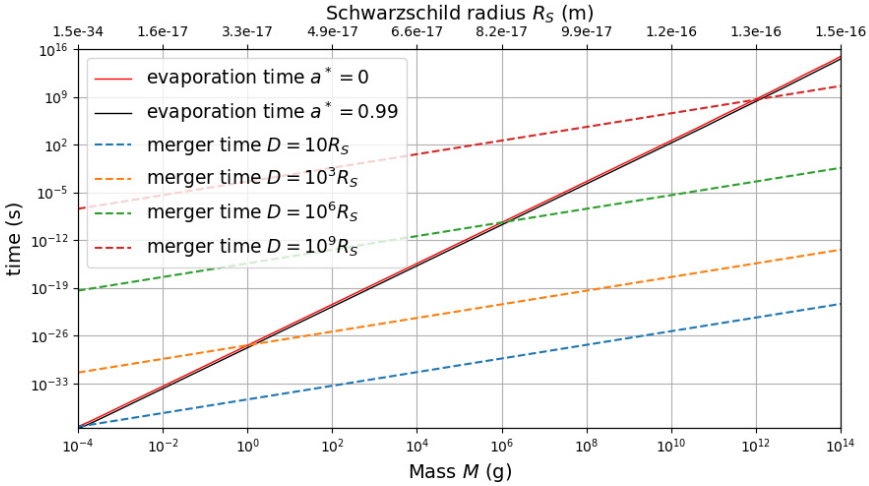

Figure 6.2 – In the time vs. BH mass plane, the solid lines correspond to the evaporation time for a BH of mass M and spin $a^* = 0$ (red) and $a^* = 0.99$ (blue). The dashed lines correspond to the merger time for two identical Schwarzschild BHs of mass M, for different initial distances D given as numbers of the Schwarzschild radius.

where ρ is the comoving radius, $a(t)$ the expansion factor, $d\Omega^2 = d\theta^2 + \sin^2\theta d\phi^2$ is the solid angle and $\mu = GM/[2a(t)\rho]$. This metric coincides with the Schwarzschild metric for a constant $a(t)$ under the redefinition $r = a\,\rho$, and with the Robertson and Walker metric in flat space at large radius. The scaling relations are preserved as long as $a(t)\rho \longrightarrow \lambda\, a(t)\rho$. In the case of a constant scale factor, the scaling relation $\rho \longrightarrow \lambda\rho$ is similar to transformation (6.1). However, in presence of expansion, it is more interesting to consider that the scaling relation would read instead $a(t) \longrightarrow \lambda\, a(t)$. In a radiation-dominated Universe $a(t) = (2\pi G\rho_0^r/3)^{1/4}t^{1/2}$, and in a matter-dominated Universe $a(t) = (6\pi G\rho_0^m)^{1/3}t^{2/3}$, where ρ_0^r and ρ_0^m are the current radiation and matter densities, respectively. Therefore, as long as the dominating component is not changing, the scaling relations are preserved when $\rho_0^r \longrightarrow \lambda^2\,\rho_0^r$ or $\rho_0^m \longrightarrow \lambda\,\rho_0^m$. This result is confirmed when considering that an expanding Universe necessarily involves a non-zero stress-energy tensor, and the density and pressure have the scaling properties given in Eq. (6.18). Using the transformations of ρ_0^m and ρ_0^r, we check that for matter $\rho^m = \rho_0^m a^{-3} \longrightarrow \lambda^{-2}\rho^m$, $P^m \approx 0$, and for radiation $\rho^r = \rho_0^r a^{-4} \longrightarrow \lambda^{-2}\rho^r$ and $P^r = \rho^r/3$, so that the needed scaling properties are respected by the stress-energy tensor. Thus, simulations of black hole mergers in expanding Universe can be rescaled as long as the dominating component is conserved and ρ_0^r or ρ_0^m are rescaled properly. However, it is also clear that there is no possibility to use a rescaling transformation from a static Universe to an expanding one.

6.4.2 Morris-Thorne traversable wormholes

We consider here the Morris-Thorne traversable wormhole metric [163], which is spherically-symmetric and static:

$$d\tau^2 = e^{2\Phi(r)}dt^2 - \frac{dr^2}{1-b(r)/r} + r^2(d\theta^2 + \sin^2\theta d\phi^2)\,, \tag{6.22}$$

where $\Phi(r)$ and $b(r)$ are arbitrary functions of $r = r_0 + l$, where r_0 is the radius of the wormhole throat and l the distance from the throat. A wormhole is connected to two universes, so that a value $r > r_0$ corresponds to two points, one in our Universe and one on the other side of the wormhole. For such a wormhole to exist, the $\Phi(r)$ should not have any singularity and $1 - b(r)/r$ has to remain positive for $r \leq r_0$. Also at infinity $\Phi(r)$ and $b(r)$ go to zero.

Contrary to the case of black holes, there exists a non-zero diagonal stress-energy tensor [164] with elements:

$$\begin{aligned} T_{tt} &= \frac{1}{8\pi G}\frac{b'}{r^2}\,, \\ T_{rr} &= -\frac{1}{8\pi G}\left[\frac{b}{r^3} - 2\left(1-\frac{b}{r}\right)\frac{\Phi'}{r}\right]\,, \\ T_{\theta\theta} = T_{\phi\phi} &= \frac{1}{8\pi G}\left[\Phi'' + \left(\Phi'\right)^2 - \frac{b'r-b}{2r^2(1-b/r)}\Phi' - \frac{b'r-b}{2r^3(1-b/r)} + \frac{\Phi'}{r}\right]\,. \end{aligned} \tag{6.23}$$

It is important to note that if the stress-energy tensor vanishes away from the throat, Birkhoff's theorem implies that the wormhole metric reduces to the Schwarzschild metric, so that an isolated wormhole is indistinguishable from the Schwarzschild black hole away from the center. The coalescence of two wormholes or a wormhole and a black hole would therefore be indistinguishable from the a pure binary black hole when they are far away, but the gravitational effects generated by the non-zero stress-energy tensor can affect the merger and the spectrum of emitted gravitational waves. Considering metric (6.22), under the transformation of Eq. (6.1), the scale invariance imposes that

$$\begin{aligned} \Phi(r) &\longrightarrow \Phi(r)\,, \\ b(r) &\longrightarrow \lambda b(r)\,. \end{aligned} \tag{6.24}$$

These conditions automatically lead to $T_{\mu\nu} \longrightarrow \lambda^{-2}T_{\mu\nu}$ since wormholes are EFE solutions.

Looking at the zero tidal force hypothesis of Morris and Thorne [163], which corresponds to $\Phi(r) = 0$ and $b(r) = (b_0 r)^{1/2}$, the scale invariance implies that the constant b_0 scales as a distance.

Concerning the emission of gravitational waves during a merger involving two wormholes, the question of their scaling properties is therefore not related to the geometry, but to the exotic energy which feeds the stress-energy tensor, and in particular to the interaction of the exotic energy of one of the wormholes with the exotic energy of the other wormhole. If their interaction has similar scaling properties as gravity, then the emitted gravitational waves will have the same scaling properties as in a binary black hole merger, but it will not be the case otherwise.

6.4.3 Loop quantum gravity inspired black holes

One of the major theoretical questions about the Schwarzschild metric concerns the naked irreducible singularity at the center, which may find a solution in quantum gravity, in which the smallest quanta is expected to have a minimal size that could affect the properties of the black hole interior and in particular the geometry at its center. We consider here the loop quantum gravity (LQG) corrected Schwarzschild metric of [165]:

$$d\tau^2 = \frac{(r-r_+)(r-r_-)(r+r_*)^2}{r^4+a_0^2}dt^2 - \left(\frac{(r-r_+)(r-r_-)r^4}{(r+r_*)^2(r^4+a_0^2)}\right)^{-1}dr^2 - \left(r^2+\frac{a_0^2}{r^2}\right)d\Omega^2\,, \tag{6.25}$$

where $r_+ = 2GM(1+P)^{-2}$, $r_- = 2GM\,P(1+P)^{-2}$ and $r_* = \sqrt{r_+\,r_-}$, with $P = (\sqrt{1+\epsilon^2}-1)/(\sqrt{1+\epsilon^2}+1)$, ϵ being a very small constant, $a_0 = A_{\min}/8\pi$ and $A_{\min}$ is the area corresponding to the smallest quanta in the LQG quantification. r_- and r_* are two small radii which prevent the singularity at $r = 0$ in the Schwarzschild metric. The Schwarzschild metric is retrieved for $\epsilon = 0$ and $A_{\min} = 0$. For this metric, the scaling relations still hold as long as $A_{\min} \longrightarrow \lambda^2 A_{\min}$, which is consistent with the scaling of an area, and ϵ is scale-independent. However, it is clear that physically the smallest quanta area should not be rescaled, but the probable small size of a_0 would certainly not allow to distinguish the gravitational waves emitted during a merger of LQG corrected Schwarzschild black holes from the ones of a standard binary black hole merger.

6.4.4 Black holes in $f(R)$ gravity

We now consider the well-known generalization of the Einstein-Hilbert Lagrangian density, where R is replaced by a generic function $f(R)$ [73, 166]. Such a modification encompasses a broad variety of new gravitational theories, including quantum gravity models.

From the definition of the Lagrangian, in empty space the scaling relation $R \longrightarrow \lambda^{-2}R$ in Einstein's gravity becomes $f(R) \longrightarrow \lambda^{-2}f(\lambda^{-2}R)$, or equivalently $R \longrightarrow f^{-1}(\lambda^{-2}f(\lambda^{-2}R))$. This transformation does not obviously hold unless $f(R) = R$. It can nevertheless still be valid in weak gravitational fields at first order in R when $f(R) \approx R$, therefore not affecting the propagation of gravitational waves.

The equation equivalent to EFEs reads in $f(R)$ gravity:

$$f'(R)R_{\mu\nu} - \frac{1}{2}f(R)g_{\mu\nu} = [\nabla_\mu\nabla_\nu - g_{\mu\nu}\Box]f'(R) + 8\pi G\,T_{\mu\nu}\,, \tag{6.26}$$

where ∇_μ is the covariant derivative, $\Box = \nabla^\mu\nabla_\mu$ is the Laplacian, and $T_{\mu\nu}$ is the standard stress-energy tensor. In the vacuum the right hand-side term appears as an effective stress-energy tensor. In case of a constant scalar curvature $R = R_0$ — as for example in empty space in the Einstein's gravity — the equation becomes in vacuum:

$$f'(R)R_{\mu\nu} - \frac{1}{2}f(R)g_{\mu\nu} = 0\,, \tag{6.27}$$

and its trace gives:

$$f'(R_0)R_0 - 2f(R_0) = 0\,, \tag{6.28}$$

which admits as solution $f(R_0) \propto R_0^2$, or $R_0 = 0$ if $f(R_0) = 0$. This second solution is the same of the one of general relativity in empty space, and the standard Schwarzschild metric is therefore a solution of the field equations (6.26) as long as $f(0) = 0$ [1]. In such a case, the scaling properties of the Schwarzschild metric in $f(R)$ gravity are therefore the same as in Einstein's gravity.

A more careful look at the field equations (6.26) reveals that even in absence of the scaling $f(R) \longrightarrow \lambda^{-2} f(\lambda^{-2} R)$ the equation itself scales as λ^{-2} in empty space, so that the scaling properties of general relativity in vacuum are conserved in $f(R)$ gravity. Therefore the merger of two Schwarzschild black holes in $f(R)$ gravity will have the same scaling properties as in Einstein's gravity, and the observed gravitational waves will also have the same properties.

Nevertheless, because of the different field equations, the gravitational waves emitted during the mergers and their propagation will be affected by $f(R)$ gravity. Thus, in the case of detection of non-standard gravitational waves, a scaling of the gravitational wave spectra similar to the one expected in Einstein's gravity would constitute a hint towards $f(R)$ gravity.

6.4.5 Black holes in gravity with higher-curvature terms

More generally, modified gravity can be based on Lagrangians with higher-curvature terms involving higher-rank tensors in addition to the scalar curvature as in $f(R)$ gravity, such as $R_{\mu\nu}R^{\mu\nu}$ or $R_{\alpha\beta\mu\nu}R^{\alpha\beta\mu\nu}$, or more complicated scalar objects such as

$$({}^*R^{\alpha\beta\mu\nu})\, R_{\alpha\beta\mu\nu} = \left(\frac{1}{2} \frac{\epsilon^{\rho\sigma\mu\nu}}{\sqrt{-g}} R^{\alpha\beta}{}_{\rho\sigma} \right) R_{\alpha\beta\mu\nu} \tag{6.29}$$

in Jackiw-Pi theory [167], where $\epsilon^{\rho\sigma\mu\nu}$ is the totally antisymmetric tensor.

In general, as long $R_{\mu\nu} = 0$ is a solution of the field equations, the Einstein's gravity Schwarzschild metric is a solution to describe static and spherically-symmetric black holes, and the scaling relations of general relativity in empty space will still be valid. This is the case for the three examples of scalars given above, but in general not for a cubic contraction of the Riemann tensor [168]. If the Schwarzschild metric is valid, similarly to $f(R)$ gravity, the emitted gravitational waves and their propagation will be affected by the modified gravity, but the scaling properties will still hold.

6.4.6 Extra-dimensional black holes

The generalization of general relativity to extra-dimensions is rather straightforward, and the geometrical part of the action in a $4+n$ dimensional spacetime reads:

$$S_g = \frac{M_*^{2+n}}{16\pi} \int d^{4+n}x \sqrt{-g} (R_4 + R_n)\,, \tag{6.30}$$

where M_* is the fundamental mass scale, R_4 is the 4-dimensional part of the scalar curvature and R_n is its n-dimensional part. An effective 4 dimension-action can be obtained

1. The converse is not necessarily true, and other spherically-symmetric and static black hole metric solutions may also exist in $f(R)$ gravity, without being valid in Einstein's gravity.

by integrating over the extra-dimensions and by neglecting the R_n term which only affects the geometry of the extra-dimensions, leading to:

$$S_g^4 = \frac{M_*^{2+n} L^n}{16\pi} \int d^4x \sqrt{-g} R_4 \,, \tag{6.31}$$

where it is assumed for simplicity that the extra-dimensions have the same size L. The Planck mass is therefore related to M_* by

$$M_P = M_*^{1+n/2} L^{n/2} \,. \tag{6.32}$$

The number n and the size L of the extra-dimensions are therefore the main parameters of this model. The Schwarzschild solution for a spherically-symmetric and static metric also exists and reads [169, 170]:

$$d\tau^2 = \left(1 - \left(\frac{r_h}{r}\right)^{1+n}\right) dt^2 - \left(1 - \left(\frac{r_h}{r}\right)^{1+n}\right)^{-1} dr^2 + r^2 d\Omega_{2+n}^2 \,, \tag{6.33}$$

where the horizon radius is given by:

$$r_h = k_n \frac{1}{M_*} \left(\frac{M}{M_*}\right)^{\frac{1}{1+n}} \,, \tag{6.34}$$

with M the black hole mass and

$$k_n = \left(\frac{8\Gamma((3+n)/2)}{(2+n)\pi^{(1+n)/2}}\right)^{\frac{1}{1+n}} \,. \tag{6.35}$$

By definition, the field equations in $(4+n)$ dimensions are scale-invariant in empty space. However, the mass scale M_* is embedded in the Schwarzschild metric. In 4 dimensions, $M_* = M_P$, which is fixed and is not modified under transformation (6.1). As for the 4 dimensional case, the scaling properties of the metric (6.33) imply that $r_h \longrightarrow \lambda r_h$, and as a consequence the scaling of the mass reads in $(4+n)$ dimensions:

$$M \longrightarrow \lambda^{1+n} M \,. \tag{6.36}$$

Similarly, the scaling properties of gravitational waves are identical to the 4-dimensional case apart from the energy which scales as the mass. The propagation of gravitational waves can be affected by the existence of extra-dimensions since the gravitational waves can propagate into the extra-dimensions, modifying for example the propagation speed.

As a consequence, one can expect deviations from the scaling of the observed gravitational waves with the masses of a black hole merger, which would be a characteristic of the considered extra-dimension model.

We studied here the case of a very simple extra-dimension scenario, but there exist many extra-dimension models, with for example more complicated geometries. In such cases both the emission and propagation of gravitational waves can be modified, altering the scaling properties obtained in this section.

6.4.7 Lovelock black holes

We consider now the case of Lovelock black holes in the 5-dimensional Einstein-Gauss-Bonnet theory [171]. The geometrical part of the effective 4-dimensional action reads:

$$S_g = \frac{1}{16\pi G}\int d^4x\sqrt{-g}\Big(-2\Lambda + R + \alpha(R^2 + R_{\alpha\beta\mu\nu}R^{\alpha\beta\mu\nu} - 4R_{\mu\nu}R^{\mu\nu})\Big)\,, \tag{6.37}$$

where Λ is the cosmological constant and α is a constant. The last term is the so-called Gauss-Bonnet term, which appears as an ultraviolet correction to Einstein's gravity.

Neglecting the cosmological constant, the spherically-symmetric and static solution of the field equations leads to the following metric [172–174]:

$$d\tau^2 = \left(1 + \frac{r^2}{4\alpha} - \frac{r^2}{4\alpha}\sqrt{1 + \frac{8k_2^2\alpha M}{M_*^3 r^4}}\right)dt^2 - \left(1 + \frac{r^2}{4\alpha} - \frac{r^2}{4\alpha}\sqrt{1 + \frac{8k_2^2\alpha M}{M_*^3 r^4}}\right)^{-1} dr^2 - r^2 d\Omega_3^2\,, \tag{6.38}$$

where k_2 is given in Eq. (6.35) and M_* is the fundamental mass scale in 5 dimensions. This metric reduces to the Schwarzschild metric in 5 dimensions when $\alpha \approx 0$ or $r^2 \gg |\alpha|$. The horizon is located at $r_h = \sqrt{k_2^2 M M_*^{-3} - 2\alpha}$, hence the condition $M > 3\pi\alpha M_*^3/k_2^2$. An interesting feature of this metric is that there is no naked singularity at the center.

For this metric to be invariant, first the mass has to follow the scaling relation $M \longrightarrow \lambda^2 M$, which is a particular case of Eq. 6.36, and second $\alpha \longrightarrow \lambda^2\alpha$. However, since α is the fundamental coupling of the Gauss-Bonnet term, it is fixed in the theory and cannot be rescaled. At long distance, since the terms involving α vanish, the gravitational waves emitted by the black hole will have the same properties as in the simple 5-dimension extension of Einstein's gravity presented in Section 6.4.6. At short distance, the Schwarzschild metric is also retrieved, but the effective mass is modified. At intermediate distance, the terms proportional to r^2 can dominate. As a consequence, the emitted gravitational waves will be similar to the ones emitted by black hole mergers in Einstein's gravity at low frequencies, with the difference that the masses will scale as λ^2, but at high frequencies such scaling relations will not hold anymore.

6.4.8 Black holes in scalar-tensor gravity

A generic class of theories is based on the existence of a scalar field coupled to geometrical tensors. For black holes, there exists a "no-hair conjecture" [175–177] which states that black hole solutions of the EFEs are completely characterized by only three parameters, the mass, the electric charge, and the angular momentum. This conjecture generally does not apply to scalar-tensor gravity scenarios, in which the black holes can develop "scalar hair" [178, 179].

We consider here the example of black holes in the Einstein-Scalar-Gauss-Bonnet theory [180], in which the geometrical part of the action reads

$$S_g = \frac{1}{16\pi G}\int d^4x\sqrt{-g}\left[R - \frac{1}{2}\,\partial_\mu\varphi\,\partial^\mu\varphi + f(\varphi)R_{GB}^2\right], \tag{6.39}$$

where $f(\varphi)$ is a generic function of the scalar field φ and

$$R_{GB}^2 = R_{\mu\nu\rho\sigma}R^{\mu\nu\rho\sigma} - 4R_{\mu\nu}R^{\mu\nu} + R^2 \tag{6.40}$$

is the quadratic Gauss-Bonnet term. In empty space, the field equations can be obtained from the action [180]:

$$R_{\mu\nu} - \frac{1}{2} g_{\mu\nu} R = T^{\varphi}_{\mu\nu} \,, \tag{6.41}$$

$$\Box\varphi + f'(\varphi) R^2_{GB} = 0 \,, \tag{6.42}$$

with

$$T^{\rm vac}_{\mu\nu} = -\frac{1}{4} g_{\mu\nu} \partial_\rho\varphi \partial^\rho\varphi + \frac{1}{2} \partial_\mu\varphi \partial_\nu\varphi - \frac{1}{2} (g_{\rho\mu} g_{\lambda\nu} + g_{\lambda\mu} g_{\rho\nu}) \eta^{\kappa\lambda\alpha\beta} \eta^{\rho\gamma\sigma\tau} R_{\sigma\tau\alpha\beta} \nabla_\gamma \partial_\kappa f(\varphi) \,, \tag{6.43}$$

and $\eta^{\rho\gamma\sigma\tau} = \epsilon^{\rho\gamma\sigma\tau} / \sqrt{-g}$.

A scaling $T^{\rm vac}_{\mu\nu} \longrightarrow \lambda^{-2} T^{\rm vac}_{\mu\nu}$ would imply for the scalar field $\varphi \longrightarrow \varphi$ and $f(\varphi) \longrightarrow \lambda^2 f(\varphi)$. These transformations are obviously self-contradictory since $f(\varphi)$ does not vary when φ is constant. However, since the last term of $T^{\rm vac}_{\mu\nu}$ is multiplied by $R_{\sigma\tau\alpha\beta}$, in the case of a weak field it will be negligible and will in particular not affect the gravitational waves.

We will now check whether the geometry around black holes can conserve its scaling properties in spite of the presence of the scalar field. In a spherically-symmetric and static metric such as:

$$d\tau^2 = A(r) dt^2 - B(r) dr^2 - r^2 (d\theta^2 - \sin^2\theta \, d\phi^2) \,, \tag{6.44}$$

the EFEs connect $A(r)$ and $B(r)$ to $\phi(r)$. Solving the set of field equations in such a metric is a complicated task, but it is interesting to consider the asymptotic solution at infinity. It reads at second order in $1/r$:

$$\begin{aligned} A(r) &= 1 - \frac{2GM}{r} \,, \\ B(r) &= \left(1 - \frac{2GM}{r} - G^2 \frac{16M^2 - P^2}{4r^2} \right)^{-1} \,, \\ \varphi(r) &= \varphi_\infty + \frac{GP}{r} + \frac{G^2 MP}{r^2} \,, \end{aligned} \tag{6.45}$$

where M is the effective mass and P is the scalar charge. The value of the scalar field at infinity φ_∞ does not play any role as long as $f(\varphi_\infty) = 0$. As a consequence, at infinity the Schwarzschild metric is retrieved at first order in r^{-1}. The next orders can be written in terms of P, so that the scalar charge appears as a new parameter (a "hair") to describe black holes in tensor-scalar gravity. It is interesting to compare this expression to the case of the charged black hole in Einstein's gravity, for which $A(r) = B^{-1}(r) = 1 - \frac{2GM}{r} + \frac{Q^2 G}{4\pi\epsilon_0 r^2}$. As for the electric charge Q, the scaling rule associated to scalar charge is therefore the same as for the mass M: $P \longrightarrow \lambda P$. This scalar charge is however generally not independent of the mass M and is related to the definition of the $f(\varphi)$ function [179].

Concerning the gravitational waves themselves, the ones emitted in the early stages of a black hole merger will be very similar to the ones in Einstein's gravity, and their propagation will be unaffected in weak gravitational fields. However, when the black holes get closer, deviations due to the presence of a scalar charge will appear, and the scaling properties will be changed, unless there exists a regime in which the scalar charge is proportional to the mass.

6.4.9 Black holes in other modified gravity models

There exist many other possibilities to alter Einstein's gravity, we consider here one last case, namely the non-relativistic Hořava-Lifshitz four-dimensional theory of gravity [181, 182], which is a renormalizable gravity theory in four dimensions which reduces to Einstein's gravity in IR but with improved UV behaviours. We will not consider here the gory detail, but study the case of the asymptotically flat, spherically-symmetric and static case, for which the metric is [183, 184]:

$$d\tau^2 = f(r)dt^2 - \frac{dr^2}{f(r)} - r^2(d\theta^2 + \sin^2\theta d\phi^2)\,, \tag{6.46}$$

where

$$f(r) = 1 + \omega r^2 - \sqrt{r(\omega^2 r^3 + 4\omega M)}\,, \tag{6.47}$$

with ω a fundamental constant of the theory and M a mass parameter. For $r \gg (M/\omega)^{1/3}$, the Schwarzschild metric is retrieved. There are two horizons located at radii:

$$r_\pm = M\left(1 \pm \sqrt{1 - \frac{1}{2\omega M^2}}\right)\,. \tag{6.48}$$

Therefore, if $\omega M^2 \geq 1/2$, there is no naked singularity at the center, where the geometry is flat. Once the fundamental parameters are fixed, only M can be changed. For $f(r)$ to be invariant under the transformation $r \longrightarrow \lambda r$, the necessary transformation laws are $\omega \longrightarrow \lambda^{-2}\omega$ and $M \longrightarrow \lambda M$. The scaling of the mass is therefore the same as in Einstein's gravity. Nevertheless, because ω is a fixed parameter, even if the gravitational waves emitted during a merger of black holes are similar to the ones of Einstein's gravity at long distances and low frequencies, the scaling properties will become invalid at short distances and high frequencies.

6.5 Testing the scaling relations

6.5.1 Rescaling of simulations of black hole mergers

We now discuss simulations of mergers of binary black holes and emission of gravitational waves, and their rescaling properties. Such simulations are computationally intensive, and each of our simulations necessitated about one week on a 64-processor server. The evolution of binary black holes includes different phases. The first one, which is the longest, is the inspiral phase described using post-Newtonian techniques. The second one is the plunge and merger phase, which can be only described via numerical relativity. The last one is the ringdown phase described by perturbation methods.

To produce some examples of simulations and solve the Einstein equations, we use the `Einstein Toolkit` code [18, 124, 127, 185]. The initial data are generated via the `TwoPunctures` routine [128] for a merger with a near circular orbit. We consider only this case since for a binary orbit with a given eccentricity e, the emission of gravitational waves leads to a decrease in eccentricity. The evolution is performed using the BSSN formulation [19] via the `McLachlan` routine [120]. To compute the properties of the emitted

gravitational waves, we use the Newman-Penrose formalism [19] where the Weyl scalar ψ_4 and the GW polarization amplitudes $h_{+,\times}$ are related by:

$$\ddot{h}_+ - i\ddot{h}_\times = \psi_4 = \sum_{l=2}^{\infty} \sum_{m=-l}^{l} \psi_4^{lm}(t,r)_{-2}Y_{lm}(\theta,\phi)\,. \tag{6.49}$$

This corresponds to the decomposition of ψ_4 into $s = -2$ spin-weighted spherical harmonics. The dominant modes for the gravitational wave strain h are the $l = m = 2$ modes: $h^{22}_{+,\times}$. Considering the scaling relations, since $h_{+,\times}$ are scale invariant, we have $\psi_4 \longrightarrow \lambda^{-2}\psi_4$.

The scaling relations have been used for binary black holes since a long time [186,187], and the natural units of codes correspond to $c = M_T = G = 1$ units, where $M_T = m_1 + m_2$ is the total mass of the binary system. Setting $G = 1$ corresponds in our convention to considering that the distance, time and mass units are equal, or in terms of scaling that they all scale as λ, which is correct in Einstein's gravity. We first perform two simulations of Schwarzschild BH mergers. The first one is the merger of two BHs of masses equal to 0.5, which can be taken as the reference simulation. The second one is a similar simulation with two BHs of mass 0.005, corresponding to a scale factor of $\lambda = 0.01$ and a total mass of 0.01, and for which the code is not optimized since it runs outside its natural units in which the total mass is equal to 1. Such a case would appear when non-standard black holes with different scales are considered, since one scale would need to be chosen to adjust the simulation parameters, and the other scale may be sufficiently different to generate numerical instabilities. To compare both simulations, all the initial quantities are rescaled using the relations given in Section 6.2.1 (e.g. mass of the BHs, initial angular momenta of the two BHs, ...). In Figure 6.3, we show the real part of the Weyl tensor and the GW strain for $l = m = 2$, as a function of time. To fulfil the scale invariance, the time and Weyl tensor have been adimensioned using the total initial mass, as given in the axis labels. As expected the two simulations give similar results in these scale invariant parameter planes. The main difference is a high-frequency numerical noise, which comes from interpolation procedures between the different path grids. In order to reduce this noise, it is necessary to finely adjust the strength of the Kreiss-Oliger artificial dissipation term [188] or change the finite differential order, but this requires re-running simulations with adjusted parameters until the correct precision is reached. On the contrary, the reference simulation does not show any instability. Such effects are even more primordial for binary neutron star mergers to characterized matter effects. In numerical relativity simulations, the tidal effects tend to be overestimated because of numerical dissipation which accelerates the inspiral phase, and on the other hand the post-Newtonian development tends to underestimated them because of the limited knowledge of higher post-Newtonian order.

Figure 6.4 shows ψ_4^{22} and h_+^{22} for a similar merger, for two Kerr BHs with reduced spin parameters $a^* = \pm 0.5$, as a function of time. Similarly to Figure 6.3, we made two simulations of BH mergers with total masses of 1 and 0.01. We see that the numerical noise has in the case of Kerr BHs a larger impact which leads to a shift at later times. This can only be reduced using a very finely adjusted Kreiss-Oliger dissipation strength and/or a change of finite differential method, after which it is mandatory to run many simulations to reach a correct precision.

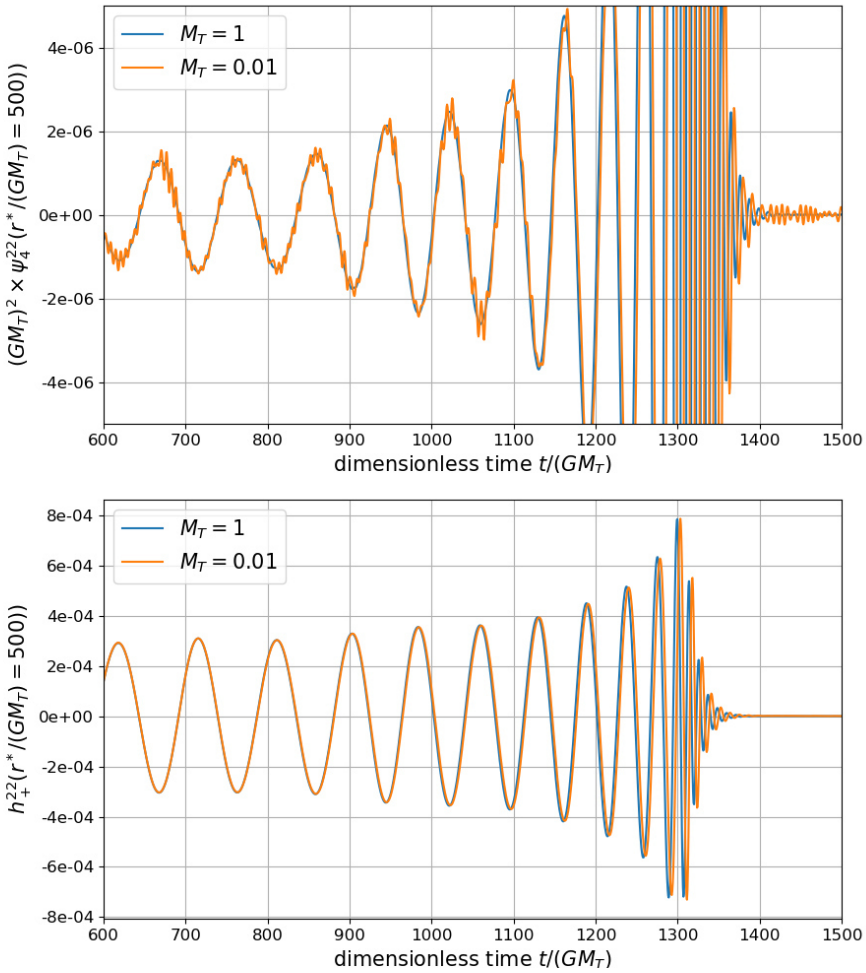

Figure 6.3 – Real part of the dimensionless Weyl scalar ψ_4^{22} (up) and GW strain signal h_+^{22} (down) as a function of the dimensionless time, corresponding to the mergers of two Schwarzschild BHs for a total mass M_T of 1 (blue) and for a total mass M_T of 0.01 (orange).

As discussed in the previous sections, when comparing the spectra of the observed gravitational waves of numerous black hole mergers, a breaking of the scaling relations of Einstein's gravity would be an unambiguous sign of non-standard gravity. The simulations that we have produced show that if there exists a scale in the studied non-standard black hole models which differs by two orders of magnitude from the main scale (set in general by the mass), numerical instabilities can occurs, in particular at high frequencies. This problem already exists when simulating mergers of two black holes with very different masses (even if, when one mass is negligible, a perturbative approach may be possible). In the case the gravitational waves of binary black hole mergers reveal a breaking of the scaling relations, it will be necessary to perform simulations in non-standard gravities in order to interpret the results, and to generate templates for gravitational wave experiments. It will

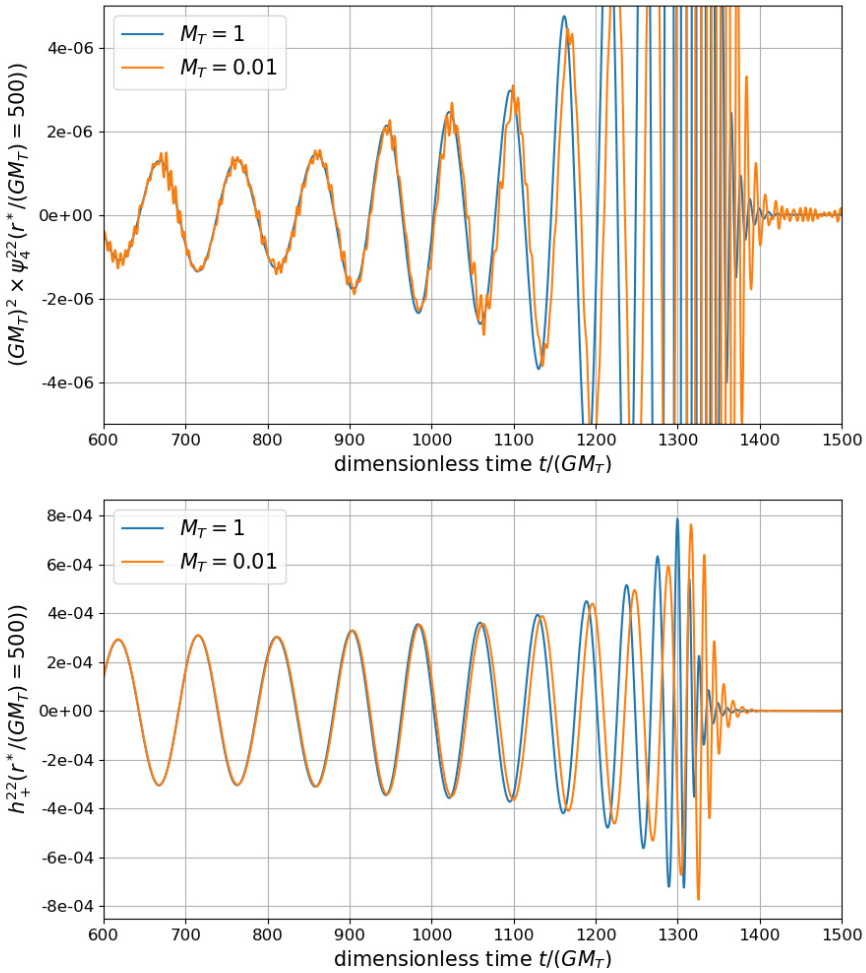

Figure 6.4 – Same as Figure 6.3 for two spinning BHs of reduced spin parameters $a^* = \pm 0.5$.

then be important to pay attention to the fact that numerical instabilities induced by the presence of several scales may generate a spurious breaking of scaling properties, which may misleadingly be interpreted as non-standard physics. Nevertheless, as we have seen, in non-standard models the new parameters can also follow scaling rules. If they are unknown on the theory side, the scaling relations can be used to reduce the number of simulations to be performed to generate a library of templates spanning the model parameters, and to rescale the resulting templates by rescaling also the fundamental parameters.

6.5.2 Testing General Relativity

The limits of general relativity can be tested in extreme gravity environments via gravitational wave detections by comparing theoretical predictions with the observated waveforms. A first approach is to subtract a computed template from the data and check whether it is compatible with the detector design noise. A more elaborate approach is

to measure the deviations by using the so-called parameterized post-Einsteinian (ppE) formalism introduced by Yunes and Pretorius [189]. This strategy does not suppose any knowledge of a new theory and is model-independent. There is no need to compute gravitational waveforms beyond the usual general relativity, which may prove to be difficult, if not impossible; however, if some deviations are measured, this formalism will not give information on the underlying model. The ppE formalism describes the amplitude A and phase Ψ corrections at a post-Newtonian order n to the gravitational waveform h by a couple of two parameters (α_n, β_n) given by:

$$\begin{aligned} A &\to A(1+\alpha_n u^{2n})\,, \\ \Psi &\to \Psi + \beta_n u^{2n-5}\,, \end{aligned} \tag{6.50}$$

with $u = (\pi \mathcal{M} f)^{1/3}$, where $\mathcal{M}$ is the chirp mass of the binary system. To recovered general relativity, α_n and β_n must be equal to zero. The study of the GW150914 [190] and GW151226 [191] events performed in [192] sets only upper limits on $|\alpha_n|$ and $|\beta_n|$, showing the compatibility with general relativity. With the improvement of detectors, or with future generations such as Einstein Telescope, deviations may be observed. Scaling relations derived in the previous sections represent a powerful tool to discriminate models. Indeed, in a scaling theory, the observations will all lead to the same values for (α_n,β_n) because the gravitational waveforms h are scale-invariant, contrary to a non-scaling theory.

To give an example, one can consider the Einstein-dilaton Gauss-Bonnet Gravity described in Ref. [193]:

$$\mathcal{S} = \int d^4x\sqrt{-g}\left[\alpha\psi(R^2 + R_{\alpha\beta\mu\nu}R^{\alpha\beta\mu\nu} - 4R_{\mu\nu}R^{\mu\nu}) - \frac{1}{2}\nabla_\nu\psi\nabla^\nu\psi\right]. \tag{6.51}$$

In this theory, the amplitude A and the phase Ψ are modified at the (-1) post-Newtonian order and are given by [192, 193]:

$$\begin{aligned} \alpha_{-1} &= -\frac{-5}{192}\frac{16\pi\alpha^2}{M_T^4}\frac{\left(m_1^2\tilde{s}_2 - m_2^2\tilde{s}_1\right)^2}{M_T^4\eta^{18/5}}\,, \\ \beta_{-1} &= -\frac{-5}{7168}\frac{16\pi\alpha^2}{M_T^4}\frac{\left(m_1^2\tilde{s}_2 - m_2^2\tilde{s}_1\right)^2}{M_T^4\eta^{18/5}}\,, \end{aligned} \tag{6.52}$$

where $\tilde{s}_i = 2\left(\sqrt{1-\chi_i^2} - 1 + (a_i^*)_i^2\right)/(a_i^*)^2$, with $a_i^* = |\vec{J}_i|/m_i^2$ the dimensionless spins. The scale rules $m_i \to \lambda m_i$, $J_i \to \lambda^2 J_i$ and $f \to \lambda^{-1} f$ imply that u is scale invariant but not (α_{-1},β_{-1}):

$$\begin{aligned} \alpha_{-1} &\to \lambda^{-4}\alpha_{-1}\,, \\ \beta_{-1} &\to \lambda^{-4}\beta_{-1}\,, \end{aligned} \tag{6.53}$$

which is incompatible with the scale-invariance of a waveform h.

On the other hand, if one considers the scalar-tensor theory described in [192, 194], the correction β is given by:

$$\beta = -\frac{5}{1792}\dot{\phi}^2\eta^{2/5}\left(m_1\bar{s}_1 - m_2\bar{s}_2\right)^2\,, \tag{6.54}$$

with $\bar{s}_i = \left(1 + \sqrt{1 - (a_i^*)^2}\right)/2$. Thus β is scale invariant by considering the usual rules: $m_i \to \lambda m_i$, $J_i \to \lambda^2 J_i$, $f \to \lambda^{-1} f$, $t \to \lambda t$ and $\phi \to \phi$.

Scaling relations can therefore be used to discriminate between models if deviations from general relativity are measured through gravitational wave detection.

6.6 Conclusions and perspectives

In this chapter, we have studied scaling transformations for black hole mergers, from primordial to supermassive black holes. We have verified that these rescaling relations are not only valid for Schwarzschild and Kerr spinning black holes, but also for Kerr-Newman charged spinning black holes, and that they extend to both the gravitational and electromagnetic waves emitted by such mergers. This opens the way to a rescaling of numerical simulations for the most general cases of black holes, and in particular for primordial black holes which are more likely to have extremal spins and large electromagnetic charges, thus reducing the number of parameters to be varied for a full coverage of the parameter space of black hole mergers. However, primordial black holes have specificities which can lead to a breaking of the scaling relations. We have therefore studied the limitations of the rescaling of primordial black holes: first, in the early Universe, the cosmological expansion can prevent the merger because it increases the distances faster than the merger decreases them. Then, for light primordial black holes, Hawking evaporation can be faster than the merger. Finally, we have considered non-standard black holes models, such as the Morris-Thorne wormhole model, the loop quantum gravity inspired Schwarzschild hole model, and several cases of modified gravity black hole models, which can have different scaling properties.

The scaling relations for black hole mergers and their emission of gravitation and electromagnetic waves are of utmost importance, because they emerge from the invariance of general relativity and electromagnetism in empty space, and can allow to speed up numerical simulations of numerous templates. As a consequence, with the multiplication of observations of GWs from BH mergers, it will be important to compare the observed spectra of binary black holes with different masses, because deviations from the scaling relations will be a clear sign of the presence of non-standard phenomena and may lead to the discovery of new gravitational physics.

7

Discriminating same-mass Neutron Stars and Black Holes gravitational wave-forms

Gravitational wave-forms from coalescences of binary black hole systems and binary neutron star systems with low tidal effects can hardly be distinguished if the two systems have similar masses. In the absence of discriminating power based on the gravitational wave-forms, the classification of sources into binary neutron stars, binary black holes and mixed systems containing a black hole and a neutron star can only be unambiguous when assuming the standard model of stellar evolution and using the fact that there exists a mass gap between neutron stars and black holes. This approach is however limited by its own assumptions: for instance the 2.6 solar mass object detected in the GW190814 event remains unclassified, and models of new physics can introduce new compact objects, like primordial black holes, which may have masses in the same range as neutron stars. Then, without an electromagnetic counterpart (kilonova), classifying mergers of compact objects without mass gap criteria remains a difficult task, unless the source is close enough. In what follows we investigate a procedure to discriminate a model between binary neutron star merger and primordial binary black hole merger by using a Bayes factor in simulated wave-forms that we superimpose to realistic detector noise.

Contents

7.1 Introduction

Gravitational wave astronomy has entered a new era, characterized by the detection of a plethora of coalescing compact binary objects from the recent LIGO and Virgo runs [99, 195], with a large range of masses for the individual compact objects. In particular, the GW190814 event [12] corresponds to a merger involving a compact object with a 2.6 solar masses. Such a mass falls typically in the intermediate range between the known black hole masses and neutron star masses [196–198], therefore this object can be either the most massive neutron star or the lightest black hole ever detected. In terms of gravitational wave emission, the main difference to be expected is related to the condensed matter effect of neutron stars. Unfortunately, the detector sensitivities are currently too low to observe the impact of matter effect, and in absence of electromagnetic counterpart to determine the nature of this compact object. The mechanisms of formation of a black hole or a neutron star of 2.6 solar masses remains unclear and an interesting idea is to consider that this object is a primordial black hole (PBHs) [199].

Contrary to stellar black holes which are produced by supernovae, PBHs may have been produced in the early Universe, during e.g. a phase transition. Their size is limited by the Hubble scale, which is related to the cosmological time, providing a link between the maximum PBH mass and the epoch of formation [5], and in practice PBHs can theoretically have a mass between the Planck mass and millions of solar masses. Because of Hawking evaporation, light PBHs lose mass under the form of radiation, and it has been shown that PBHs with masses below 10^{15} grams would have already evaporated since their formation [5], but heavier PBHs have sufficiently low evaporation rates to still remain. Because of this, PBHs can constitute the whole or a large fraction of dark matter, and they are usually considered as good candidates for dark matter [5]. The GW190814 event is not the only event to contain a compact object of unknown nature because of a too low resolution of detectors ; the question about the nature of compact objects can also be asked for the GW190425 event [200].

In this chapter, we study the differences between gravitational wave-forms (GWs) produced by the coalescence of binary neutron stars (BNS), binary black holes (BBH) and mixed systems containing a black hole and a neutron star (BHNS). The shapes of these gravitational wave-forms are rather similar when the objects involved in the merger have similar masses. The main goal of this paper is to understand under which circumstances and conditions it is possible to discriminate between BBH and BNS wave-forms by making use of injected signals with realistic noise profiles. In section 7.2, BBH, BHNS and BNS templates will be compared using the match which is equivalent to the overlap maximized over time and phase, and the odds number will be introduced to compare two competing models. In section 7.3, we will study the possibility of misinterpreting the results when injecting a PBH wave-form into advanced detector noise and interpreting the data in the context of BNS mergers. We will also explore the opposite problem, when BNSs are interpreted as BBHs, and we will conclude in Section 7.4.

7.2 Model selection

7.2.1 Degeneracy between BNS, BHNS and BBH wave-forms

A first approach to compare two GWs is to use the convolution product of the two GWs in the time domain which is defined as the integral of the product of two GWs after one of them has been reversed, shifted and extended by zero values. The discriminating parameter to vary between BNS, BHNS and BBH wave-forms is the tidal deformability characterizing the matter effect [201–203] which is only defined for neutron stars [1]. Without mass gap hypothesis, it is this parameter that will play a central role in characterizing the nature of compact objects. For example, the convolution product of the wave-forms between a BBH and a BNS normalized with the convolution product of BBH with itself is 0.937 for tidal deformabilities equal to $\Lambda_1 = \Lambda_2 = 600$ and 0.997 for $\Lambda_1 = \Lambda_2 = 0$.

Following the article [205], the approach to compare two wave-forms taking into account the sensitivity of the detectors, is based on the noise-weighted inner product between two wave-forms h_1 and h_2 defined by:

$$\langle h_1|h_2\rangle = 4\Re \int_{f_{min}}^{f_{max}} \frac{h_1(f)h_2^*(f)}{S_n(f)}\,, \tag{7.1}$$

where $S_n(f)$ is the power spectral density, that encodes the frequency-dependent sensitivity of a detector [206]. To calculate such scalar product, we take the advanced LIGO design sensitivity given by *aLIGOZeroDetHighPower* [207], plotted in Figure 7.1. The separation between two wave-forms h_1 and h_2 can be related to their match, which is defined by the overlap maximized on the coalescence time and the coalescence phase:

$$M(h_1, h_2) = \max_{\Delta t, \Delta\phi} \frac{\langle h_1|h_2\rangle}{\sqrt{\langle h_1|h_1\rangle}\sqrt{\langle h_2|h_2\rangle}}\,. \tag{7.2}$$

In gravitational wave searches for Compact Binary Coalescences (CBC), the LIGO/Virgo Collaboration constructs template banks so that the match is at least 0.97 between the two closest wave-forms [208]. To measure a difference between a neutron star and a black hole via their gravitational wave-forms without taking into account the masses of the compact objects, it is necessary to detect a significant matter effect affecting the wave-form through the tidal deformability. To give an example of the difficulty of such a task, the match between a BBH and a BNS with $\Lambda_1 = \Lambda_2 = 600$ with a chirp mass of 1.44 $M_\odot$ and a mass ratio of 0.9 is higher than 0.97. It requires at least $\Lambda_1 = \Lambda_2 = 800$ to have a match lower than 0.97.

When a signal is detected, given a model $\mathcal{M}_A$, the marginalized posterior probability density function of all unknown parameters θ is typically computed by using a Bayesian analysis. The mean of the parameters θ is noted $\langle\theta\rangle$. Following the Eq. (18) of [209], the confidence region at a given probability p is the set of points that verifies the following condition:

$$2\rho^2\left[1 - M(h(\theta), h(\langle\theta\rangle))\right] \leq \chi_k^2(1-p)\,, \tag{7.3}$$

1. The tidal deformability is also defined for a black hole submitted to an external gravitational field [204], but its value is so small that it can be neglected for our study.

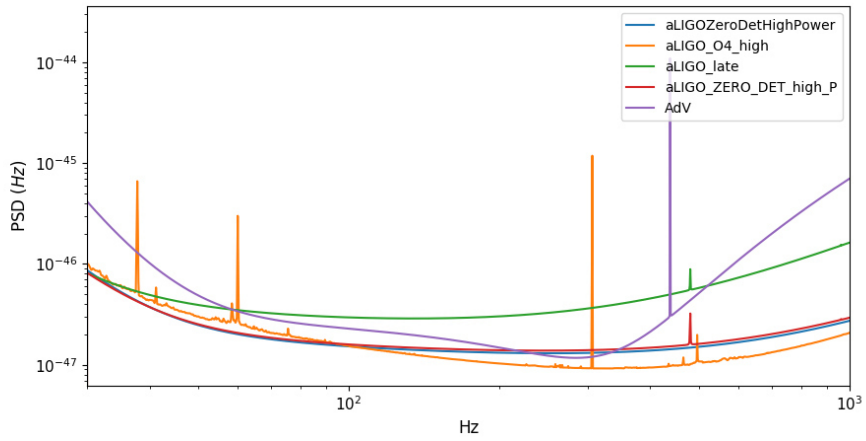

Figure 7.1 – Power spectral density of noise for the advanced LIGO and Virgo detector configurations.

where ρ is the signal to noise ratio (SNR) and $\chi^2_k(1-p)$ is the chi-squared, in the case of k degrees of freedom. We can use this relation to determine the regions in the parameter space in which two different wave-forms can be distinguished. For a given SNR, if spins are neglected, BNS templates have only 4 parameters: the chirp mass $\mathcal{M}$, the mass ratio q and the two tidal deformabilities Λ_1, Λ_2 because the match is maximized over phase, time and distance. Since we want to measure matter effects to distinguish between a neutron star and a black hole, we consider only the tidal deformabilities as free parameters and fix the others. In addition, we make the simplifying assumption that $\Lambda_1 = \Lambda_2$. We write Eq. (7.3) for the case where $h(\langle\theta\rangle)$ is a BBH wave-form and for the case where $h(\theta)$ is a BNS one with $\Lambda_1 = \Lambda_2$. It follows that BBH and BNS can be distinguished (and the nature of the compact object can be determined) if:

$$2\rho^2 \left[1 - M(h_{\rm BNS}, h_{\rm BBH})\right] \geq \chi^2_k(1-p)\,, \tag{7.4}$$

with $\chi^2_k(1-p) = 2.71$ at 90% C.L., which corresponds to one degree of freedom since the tidal deformability is the only free parameter ($\Lambda_1 = \Lambda_2$). The left-hand side of Eq. (7.4) depends on the fixed parameters but also on the luminosity distance d through the SNR: $\rho \simeq \langle h_{\rm BBH}|h_{\rm BBH}\rangle^{1/2} \simeq \langle h_{\rm BNS}|h_{\rm BNS}\rangle^{1/2}$ which is proportional to $1/d$. Figure 7.2 shows $2\rho^2 \left[1 - M(h_{\rm BNS}, h_{\rm BBH})\right]$ as a function of the deformability of neutron stars. The horizontal lines correspond to the 90 and 99% C.L. limits: a point above one of these lines means that BBH and BNS mergers can be distinguished at more than 90% of 99% C.L. The wave-forms are calculated using `IMRPhenomPv2` [132–134] for BBH and `IMRPhenomPv2_NRTidal` [210–212] for BNS. As expected, the ability of distinguishing BBH and BNS increases with the tidal deformabilities and the chirp mass, and decreases with the distances. For example, for a distance of $d = 200$ Mpc, with $\mathcal{M} = 1.44\ M_\odot$ and $q = 0.9$, the nature of the compact objects can be determined if the tidal deformabilities are higher than 200, while for a distance of 400 Mpc even tidal deformabilities of 1000 are not enough to make the BBH and BNS wave-forms distinguishable at 99% C.L.

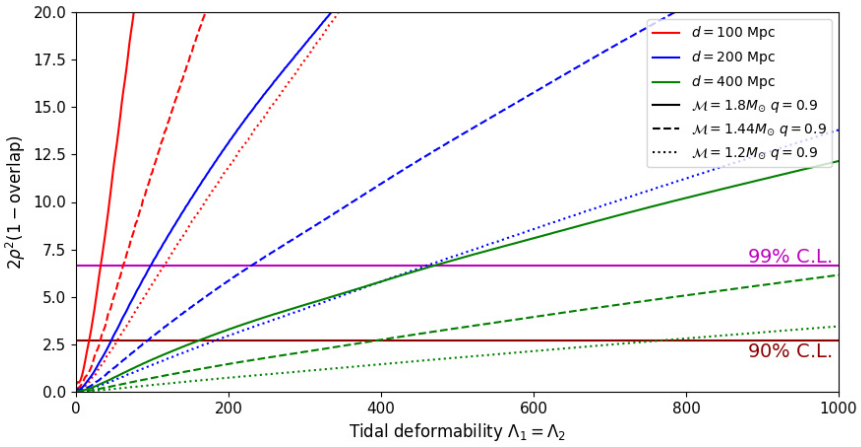

Figure 7.2 – Comparison between BBH and BNS wave-forms. The curves show the left-hand side of Eq. (7.4) as a function of the tidal deformabilities of the neutron stars. The horizontal lines show the value of χ^2_k for different confidence level thresholds : if a point is below the horizontal lines, the two mergers are too similar to be distinguished at the given confidence level. Different types of curves (solid, dashed and dotted) of the same color indicate different chirp masses and different types of colors indicate different distances. In particular, ($\mathcal{M} = 1.2 M_\odot$, $q = 0.9$) corresponds to ($m_1 = 1.45 M_\odot$, $m_2 = 1.31 M_\odot$), ($\mathcal{M} = 1.44 M_\odot$, $q = 0.9$) to ($m_1 = 1.74 M_\odot$, $m_2 = 1.57 M_\odot$) and ($\mathcal{M} = 1.8 M_\odot$, $q = 0.9$) to ($m_1 = 2.18 M_\odot$, $m_2 = 1.96 M_\odot$)

We performed a similar study for the comparison of BBH and BHNS wave-forms, to determine the conditions under which it is possible to distinguish the nature of the compact object coalescing with the black hole. For this case, the BBH wave-forms are generated with `IMRPhenomPv3HM` [213], because higher-order modes are important for such asymmetric systems, and `IMRPhenomNSBH` [214] is used for BHNS. The results are shown in Figure 7.3, for different asymmetric systems. For a small mass ratio of 0.112, the overlap between BBH and BHNS wave-forms does not really depend on the tidal deformability of the second compact object. Indeed, in such asymmetric configurations, the coalescence evolution is driven by the most massive object: the smallest object is absorbed by the black hole and its tidal deformability has a negligible effect. In this case, for a chirp mass of 4 $M_\odot$, the nature of the companion can be determined only for a system at low distance (less than 200 Mpc). The more symmetric the system, the more important the tidal deformability is to distinguish BBH and BHNS wave-forms.

The results shown in Figures 7.2 and 7.3 depend strongly on the detector sensitivity. Indeed, any change in the power spectral density (PSD) $S_n(f)$ directly affects the noise-weighted inner product between two wave-forms (Eq. (7.1)). Some examples of PSD are drawn in Figure 7.1. Their impact on the ability to distinguish between BBH and BNS templates and to determine the nature of compact objects is shown in Figure 7.4 for the system defined by $\mathcal{M} = 1.44\ M_\odot$, $q = 0.9$ and $d = 200$ Mpc.

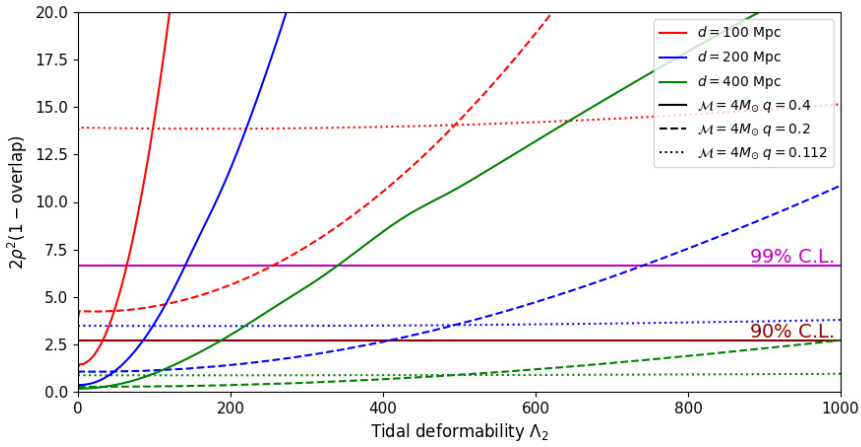

Figure 7.3 – Same as Figure 7.2 for BBH and BHNS templates. ($\mathcal{M} = 4M_\odot$, $q = 0.112$) corresponds to ($m_1 = 15.2M_\odot$, $m_2 = 1.7M_\odot$), ($\mathcal{M} = 4M_\odot$, $q = 0.2$) to ($m_1 = 10.9M_\odot$, $m_2 = 2.2M_\odot$) and ($\mathcal{M} = 4M_\odot$, $q = 0.4$) to ($m_1 = 7.4M_\odot$, $m_2 = 3.0M_\odot$).

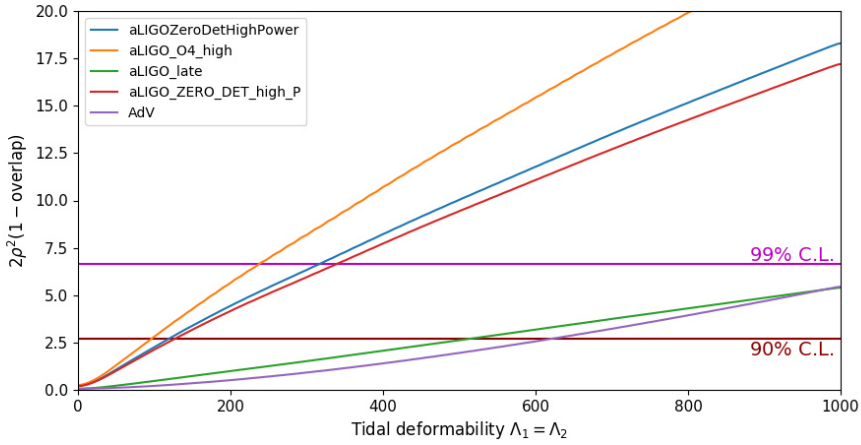

Figure 7.4 – Comparison between BBH and BNS mergers, assuming the different power spectral densities shown in Figure 7.1. The chirp mass is fixed at 1.44 $M_\odot$, the mass ratio at 0.9 and the distance at 200 Mpc.

7.2.2 The odds number

The Bayes' theorem links the posterior distribution to the likelihood, the prior and the evidence [215]:

$$p(\theta|d, \mathcal{M}_A) = \frac{\pi(\theta|\mathcal{M}_A)\mathcal{L}(d|\theta, \mathcal{M}_A)}{\mathcal{Z}(d|\mathcal{M}_A)}\,, \tag{7.5}$$

$p(\theta|d, \mathcal{M}_A)$ is the posterior distribution which gives the probability of all unknown parameters θ, given the experimental data d within the model $\mathcal{M}_A$. $\mathcal{L}(d|\theta, \mathcal{M}_A)$ is the likelihood

function. $\pi(\theta|\mathcal{M}_A)$ is the prior assuming $\mathcal{M}_A$. $\mathcal{Z}(d|\mathcal{M}_A)$ is the evidence which is the integral over the full set of parameters θ of the product of the likelihood and the prior:

$$\mathcal{Z}(d|\mathcal{M}_A) = \int d\theta \mathcal{L}(d|\theta, \mathcal{M}_A)\, \pi(\theta|\mathcal{M}_A)\,. \tag{7.6}$$

Our goal is to study when BNS, BHNS and BBH mergers can be distinguished via the wave-forms of the emitted GWs. Bayesian analysis estimates the posterior probability density function for a given model $\mathcal{M}_A$. In order to compare two competing models, the odds number can be used [215]:

$$\mathcal{B}_{AB} = \frac{p(\mathcal{M}_A|d)}{p(\mathcal{M}_B|d)} = \frac{p(\mathcal{M}_A)}{p(\mathcal{M}_B)} \frac{\mathcal{Z}_A}{\mathcal{Z}_B}\,, \tag{7.7}$$

where $\mathcal{Z}_{A/B}$ is the evidence and $p(\mathcal{M}_{A/B})$ is the prior belief in model A/B. Thereafter, GW data are analyzed without assumption on the nature of the compact objects whichever their mass, and $p(\mathcal{M}_A)/p(\mathcal{M}_B)$ is fixed to one. $\mathcal{B}_{AB} = \mathcal{Z}_A/\mathcal{Z}_B$ is the Bayes factor between the two competing models $\mathcal{M}_A$ and $\mathcal{M}_B$. Jeffrey's scale [216] gives an empirical calibration of the strength of evidence and if $\ln \mathcal{B}_{AB} > 5$, $\mathcal{M}_A$ is strongly preferred. Limits for strong evidence, moderate evidence and inconclusive are given in the Table 7.1.

It is important to notice that a Bayes factor penalizes more complicated models with a large prior volume or a fine tuning. In other words, a particularly simple model giving a worse fit to the data can be preferred over a complicated model giving a better fit. This can be intuitively understood invoking the Occam's razor principle as explained in reference [217].

$\lvert \ln \mathcal{B}_{AB} \rvert$	Probability	
< 1	< 0.731	Inconclusive
2.5	0.924	Moderate evidence
5	0.993	Strong evidence

Table 7.1 – Jeffrey's scale to compare two competing models using the Bayes factor.

7.3 Model comparison with Bayes factor in injected data

In this section we use `IMRPhenomPv2`, `IMRPhenomPv2_NRTidal` and `IMRPhenomNSBH` to describe BBH, BNS and BHNS wave-forms, respectively. The generated templates are used to analyze LIGO/Virgo data, and will constitute our model hypothesis to test against the simulated data. For this, we choose to perform a Bayesian analysis for each template and study its output in terms of the posterior distribution of the parameters and the signal-to-noise ratio. To determine which template better describes the data, we use the odds number introduced in the previous section. The power spectral density of the detector noise is taken to be the one of the advanced configurations for the O_4 simulations [2]. As the nature of the compact objects is assumed unknown, three analyses are performed, one with the BBH system, one with the BNS system and finally one with the BHNS system. Then,

2. https://dcc.ligo.org/LIGO-T2000012/public

we compute the Bayes factor between these models in order to find which one describes best the simulated data, with a decisive choice whenever the Bayes factor is higher than 5. The results are computed using `pBilby` [218–220] with nested sampling, as introduced by Skilling [221].

7.3.1 Injected wave-form

The first step in this study consists in generating a gravitational wave-form given by a template and adding it to the design Gaussian noise of advanced detector configurations as reported in [222]. The GW depends on 15 parameters: chirp mass $\mathcal{M}$, mass ratio q, two angular momenta $\vec{S}_{1,2}$ (for aligned spin systems, only $\chi_i = \vec{S}_i.\hat{\vec{L}}/m_i^2$ are needed, where $\hat{\vec{L}}$ is the normalized orbital momentum), 2-dimensional sky localization (right ascension ra and declination dec), luminosity distance d, two angles for the orbital plane (inclination angle ι and the polarization angle ψ), coalescence time t and phase of coalescence ϕ. For a BNS merger, 17 parameters must be used because the two tidal deformabilities Λ_1 and Λ_2 must be added to the list.

The location of the source in the sky is chosen to maximize the signal for the most sensitive detector (optimal configuration). The PSD for the Virgo detector, which determines the sensitivity of the detector, is chosen for the advanced configuration, shown in purple in Figure 7.1. For the Hanford and Livingston detectors, the PSD has been represented in orange and is the same for both. The source location is taken to maximize the signal for the Hanford detector. For a coalescence at a GPS time of 1.2×10^9 s, this gives 5.49 rad for right ascension and 0.81 rad for declination. The inclination and polarization are chosen at 0 rad. For a physical luminosity distance of 400 Mpc, the effective distance for these parameters gives 400 Mpc for Hanford, 449 Mpc for Livingston, and 1867 Mpc for Virgo; the antenna pattern of the emission is maximal for Hanford as expected. Unfortunately, the Virgo detector is almost blind. A simple change in declination improves the average effective distance of the three detectors. For example, a declination of 1.49 rad instead of 0.81 rad gives an effective distance of 512 Mpc for Hanford, 626 Mpc for Livingston and of 590 Mpc for Virgo. However, this change in declination does not improve the signal/noise Bayes factor: $\mathcal{B}_{SN} = \mathcal{Z}_S/\mathcal{Z}_N$ where $\mathcal{Z}_N$ is the noise evidence sometimes called null likelihood.

The spin of neutron stars in a binary system is generally extremely weak. Well before the inspiral phase detected by gravitational wave detectors, the spin of neutron stars is suppressed by electromagnetic interactions. On the contrary, standard and primordial black holes, which do not have this suppression mechanism, can have larger spins during the merger, and a primordial black hole can even have a spin very close to that of an extreme Kerr black hole. If a compact object is detected with a large spin, there is a strong chance that it is a black hole and if the spin is almost equal to 1: a primordial black hole. As for the mass criterion, we propose here to study the distinction between BH and NS only with the Bayes factor without adding assumptions in the prior and we will restrict ourselves to compact objects injected without spin. A priori, the presence of a spinning BH in the coalescence will not increase the odds number to distinguish two models, because it is always possible to assume a spinning NS.

In the following, we will consider an injected signal with the optimal configuration for

	Name of models	Number	Sampling parameters
Restricted space	BBH W/O Spin	2	$\mathcal{M}$, q
	BNS W/O Spin	4	$\mathcal{M}$, q, Λ_1, Λ_2
	BBH 1D Spin	4	$\mathcal{M}$, q, χ_1, χ_2 (aligned spin)
	BBH 3D Spin	8	$\mathcal{M}$, q, a_1, a_2, θ_1, θ_2, ϕ_{JL}, ϕ_{12} (full spin description)
	BNS W/O Spin with Λ_i fixed	2	$\mathcal{M}$, q (Λ_1 and Λ_2 are fixed at 0)
Full space	BBH	11	$\mathcal{M}$, q, χ_1, χ_2, ra, dec, d, θ_{JN}, ψ, t, ϕ
	BHNS	12	$\mathcal{M}$, q, χ_1, χ_2, Λ_2, ra, dec, d, θ_{JN}, ψ, t, ϕ
	BNS	13	$\mathcal{M}$, q, χ_1, χ_2, Λ_1, Λ_2, ra, dec, d, θ_{JN}, ψ, t, ϕ
	BNS with Λ_i fixed	11	$\mathcal{M}$, q, χ_1, χ_2, ra, dec, d, θ_{JN}, ψ, t, ϕ ($\Lambda_1 = \Lambda_2 = 0$)

Table 7.2 – Sampling parameters used for the different Bayesian analyses. The parameters not mentioned in sampling parameters are set to the value used in the injected data.

Hanford as described in above. Compact objects are chosen without spin and with masses equal to $m_1 = 1.74\ M_\odot$ and $m_2 = 1.57\ M_\odot$ i.e. a chirp mass of $\mathcal{M} = 1.44\ M_\odot$ with $q = 0.9$ and $\chi_i = 0$. For an injected BBH data created by `IMRPhenomPv2` routine, only the luminosity distance varies between the different injections. For BNS data created by the `IMRPhenomPv2_NRTidal` routine, the luminosity distance and the tidal deformabilities will be varied.

7.3.2 Black hole mergers interpreted as neutron star mergers

The Bayes factor is calculated between BBH/BHNS models and BBH/BNS models for an injected BBH signal of 128 seconds as described in the previous section. The sampling parameters used for the Bayesian analysis, performed using parallel bilby are given in Table 7.2. The full set of parameters is searched: there are 11 parameters for BBH, 12 parameters for BHNS and 13 parameters for BNS. The Bayes factor depends on the template but also on the prior. To reduce the dependence on the prior, the same is used for a BBH and for a BNS, namely we use a uniform prior between $0.87M_\odot$ and $5M_\odot$ for the chirp mass and between 0.125 and 1 for the mass ratio with constraints $1M_\odot < m_1 < 5M_\odot$ and $1M_\odot < m_2 < 3M_\odot$ for all the models. We also use aligned spins in the low spin limit corresponding to $|\chi_i| < 0.05$ for each model. Only the tidal deformability, modeling the matter for a NS, has no correspondent for a BH. In this case, a uniform prior between 0 and 5000 for Λ is added for a NS.

Figure 7.5 shows the variation of the Bayes factor as a function of the distance. In all cases the values of $\ln \mathcal{B}_{AB}$ represented by the dots are positive, meaning that the $\mathcal{M}_A$ model is always preferred. If a point is above the dashed horizontal line, the $\mathcal{M}_A$ model is *strongly* better (cf. Table 7.1). The $\mathcal{M}_A$ model corresponds to a BBH merger, i.e. the model which corresponds to the BBH injected signal, and the $\mathcal{M}_B$ model corresponds

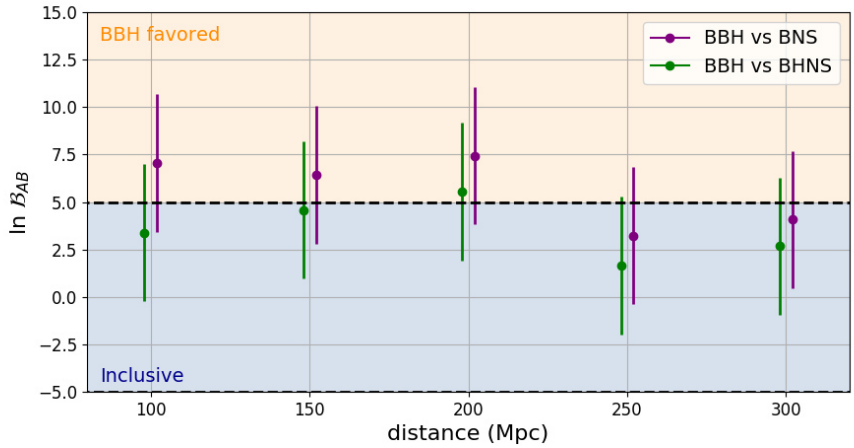

Figure 7.5 – Bayes factor for different models as a function of the luminosity distance for the optimal configuration. The chirp mass of BBH injected data is chosen to be 1.44 $M_\odot$ with a mass ratio of 0.9 and the sampling parameters for BBH, BHNS and BNS are given in Table 7.2. A point above the dashed black lines means that the BBH hypothesis is strongly favoured. In the blue region labelled "Inclusive" it is not possible to strongly prefer one model over the other.

either to a BNS merger or to a BHNS merger. For a distance smaller than 200 Mpc, the purple dots in Figure 7.5 are in the orange region and the BBH model is preferred over the BNS model which is not really the case for the BHNS model (green dots). We can therefore conclude that there is at least one black hole in the source that emitted the gravitational wave. The BNS wave-form with almost zero tidal deformability fits very well with the BBH wave-form, so the Bayes factor will prefer the model with the least parameter and as expected, the purple dots are above the green dots and above zero. Each dot plotted in Figure 7.5 is the result of one or two independent Bayesian analyses and is accompanied by a vertical bar corresponding to the possible variation of the result: this bar represents the uncertainty of the Bayes factor and its variation due to different realizations of the noise. This uncertainty has been estimated with eight simulations in the zone where a model is strongly favored (d = 150 Mpc) and in the "Inclusive" zone (d = 300 Mpc). Later in the manuscript (Figure 7.7), we show those simulation points. When the odds number is close to the limit of 5 it is not always possible to discriminate between the BBH and BNS models even with a source at a distance of 100 Mpc.

In this section and in the following we have assumed the source as oriented favorably for detection and the results are therefore rather optimistic. Moreover, we have considered a Gaussian noise for the detectors without considering terrestrial noise due for instance to meteorological conditions or human activity which is an ideal case. On the other hand, the limit can slightly improve with the increase of the chirp mass.

7.3.3 Neutron star mergers interpreted as black hole mergers

In this section, we consider the case where the injected data are generated by mergers of BNS and we try to determine whether it is possible to confuse a BNS merger with nonzero tidal deformability with a BBH merger. We inject the GWs generated by mergers of BNS with different tidal deformabilities and zero spin at different distances and study the Bayes factor between BNS and BBH.

Study on spin modeling in a restricted parameter space for Bayessian analysis

First, we focus on the impact of the BH spins on the Bayes factor. In order to reduce the computational cost, only the physical parameters of the objects are searched for, using a Bayesian analysis. The sampling parameters for the different models considered are given in Table 7.2 and the results are shown in Figure 7.6. In the top panel, the Bayes factor is calculated between the "BNS without Spin" model and a BBH model with different spin descriptions defined in Table 7.2. For data injected with $\Lambda_1 = \Lambda_2 = 600$ or with $\Lambda_1 = \Lambda_2 = 300$, the "BNS without Spin" model is always preferred regardless of the BBH models. For data injected with $\Lambda_1 = \Lambda_2 = 600$, the most favored case is the "BBH without Spin" model. Not taking spin into account in the BBH analysis, a BBH is unable to mimic a BNS and the posterior distribution of the mass ratio is not compatible with the injected value of 0.9. The spin description allows for an improved signal fit with the BBH model due to the flexibility provided by a larger parameter space. On the other hand, the Bayes factor will not automatically be better because it penalizes models with a larger number of parameters, as shown by the blue and red dots, and using a 3D spin description is worse than a 1D description within the BBH model. For data injected with $\Lambda_1 = \Lambda_2 = 100$, some values of $\ln \mathcal{B}_{AB}$ slightly prefer the BBH model in spite of the fact that the signal was created with a BNS model. The bottom panel of Figure 7.6 shows a new Bayesian analysis with the model "BNS without Spin with Λ_i fixed" represented with black dots. In this case, the BBH model is no longer preferred compared to the BNS model.

Full space parameters

In this section, the complete parameter space is probed via a Bayesian analysis (see Table 7.2) for the same injected data as in Figure 7.6. The Bayes factor between BNS and BBH is shown in Figure 7.7. As expected, the larger the tidal deformability, the clearer the distinction and the less a BBH merger can mimic a BNS merger. We can also notice the strong impact of the distance from the source on the results. When $d = 100$ Mpc, the tidal deformability is clearly reconstructed if $\Lambda_1 = \Lambda_2 \geq 300$. For a distance around 200 Mpc, the Bayes factor is not systematically in the orange region even for a strong tidal deformability and for a distance of 300 Mpc, it is no longer possible to discriminate the nature of the compact objects.

When the injected signal is a BBH (see Figure 7.5), the Bayesian analysis never prefers the BNS model even if it is not possible to conclude that it is a BBH because the Bayes factor does not reach the strong evidence limit. The purple dots in Figure 7.7, which correspond to a BNS signal with $\Lambda_1 = \Lambda_2 = 100$, seem to suggest that the BBH merger is preferred over the BNS one. This preference is just a reminder that the BNS model

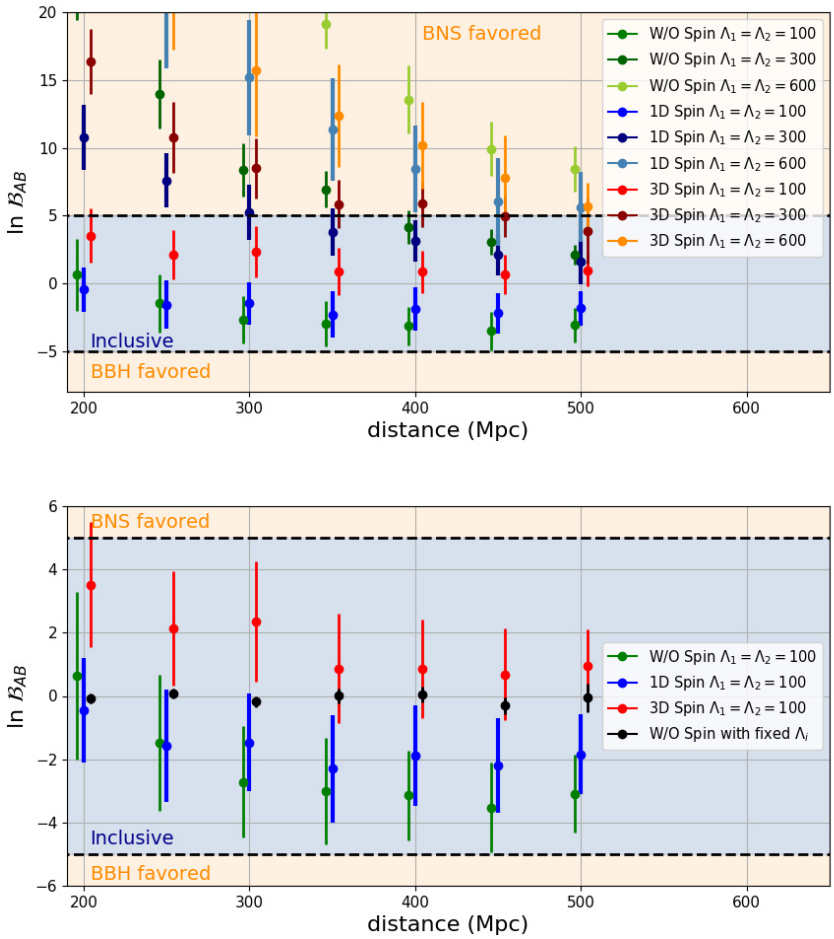

Figure 7.6 – Top panel: Bayes factor in restricted space between the model called "BNS without Spin" and different models of BBH as a function of the luminosity distance. The sampling parameters corresponding to the different models are given in Table 7.2 and the injected data correspond to BNS mergers in optimal configuration and with zero spins. Each point represents the mean value and the vertical bar the standard deviation for 4 to 6 simulations with different noise realizations. A dot located in the orange regions means that one of the two analyses is strongly preferred by the data. Bottom panel: zoom on the results for an injection with $\Lambda_1 = \Lambda_2 = 100$. The black points are added and correspond to the Bayesian analysis performed with "BNS without Spin with Λ_i fixed" and with "BBH without Spin" (see Table 7.2).

is more complex than the BBH model because it has two additional parameters. This is demonstrated by the red dots which are consistent with a zero Bayes factor when the Bayesian analysis for BNS is performed by setting $\Lambda_1 = \Lambda_2 = 0$ ("BNS with Λ_i fixed" model).

As shown in Figure 7.7, considering the PSD of the advanced detector configurations,

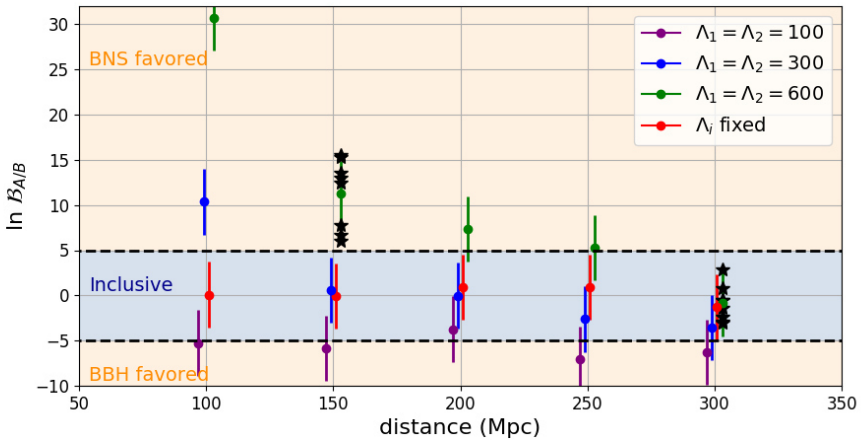

Figure 7.7 – Bayes factor in full space between BNS and BBH models as a function of the luminosity distance for different tidal deformabilities. The sampling parameters corresponding to the different models are given in Table 7.2 and the injected data are the same as in Figure 7.6. A point in the orange regions means that one of the two models is preferred, whereas a point in the blue region corresponds to an inconclusive discrimination of the best model. The red points are obtained for the same injected data as for the purple points ($\Lambda_1 = \Lambda_2 = 100$) but with the analysis called "BNS with Λ_i fixed" which sets the tidal deformabilities to zero. The variation of the results using different realizations of the noise is represented by the black stars, which were used to draw the vertical bars.

the Bayes factor does not distinguish between the BNS model and the BBH model when the source is at 300 Mpc even in the case where the tidal deformabilities are large ($\Lambda_1 = \Lambda_2 = 600$). A significant improvement is expected with Einstein Telescope [223]. To have an idea of this improvement, a BNS signal at 300 Mpc is injected in the Hanford detector with the PSD [224] of Einstein Telescope and in the Livingstone detector with the PSD of the advanced detector configuration. For a BNS signal with $\Lambda_1 = \Lambda_2 = 600$, the Bayes factor is about 90 and the BNS model is strongly favored compared to the BBH model. The distinction is even easier than with the previously considered signal which was injected at 100 Mpc (see Figure 7.7). For a BNS signal with $\Lambda_1 = \Lambda_2 = 100$, the Bayes factor is now well above the -5 limit while staying in the region labelled "Inclusive".

7.4 Conclusion

The nature of the compact 2.6 $M_\odot$ object detected in the GW190814 event is unknown: is it a neutron star, a black hole, a new type of compact object? Motivated by this event, we studied how a gravitational wave-form of a BBH merger can be distinguished from a BNS merger. Normally, the distinction is made by considering that there is a mass gap between black holes and neutron stars: a neutron star has a mass lower than 2.2 $M_\odot$ and a black hole higher than 5 $M_\odot$. The problem with the observed 2.6 $M_\odot$ object is that it does not fit into this classification. Moreover, if primordial black holes exist, they may have

masses similar to neutron stars. Thus, we reconsidered the distinction between a black hole and a neutron star by considering only the gravitational waveform without priors on the masses.

As a first step, we compared a wave-form from a BBH template, a BNS template and a BHNS template by using the match function defined in Eq. (7.2). In the case where the two objects are described by the same physical parameters: same spin, same mass, the match between the different gravitational wave-forms is close to 1. The parameter that allows us to distinguish them is the tidal deformability of the neutron star. In absence of tidal deformability, it will be impossible to have a difference. We have seen that even with a large tidal deformability, the observation of the gravitational wave of a merger at 400 Mpc will not identify a difference between the templates. For a highly asymmetric BHNS merger, the tidal deformability of the companion is not a distinguishing parameter with a merger.

During a detection, the parameters of a fusion are determined by a Bayesian analysis. Such an analysis must use the template corresponding to the nature of the compact objects. A selection criterion for the nature of the fusion is given by the Bayes factor. In the case where two models A and B are in competition: a BBH fusion for A and a BNS fusion for B for example, the quantity $\ln \mathcal{B}_{AB}$ determines the best model. If $\mathcal{B}_{AB} > 5$, model A is strongly favored compared to B and conversely if the ratio is less than -5. If the ratio is between these two values, the data can be explained by both models.We have therefore studied this ratio for data injected by considering a fusion with 1.44 $M_\odot$ for the chirp mass. This factor depends on the prior volume and penalizes the most complex systems with a larger number of parameters. For BBH injected data, the Bayes factors of the BBH models are always better compared to the others. In such a merger, the wave-form is very well reproduced by a BNS model with neutron stars having a tidal deformability equal to zero but because of the tidal deformability, the BNS model is more complex and therefore worse than the BBH model. For injected BNS data with $\Lambda_1 = \Lambda_2 = 600$, the Bayes factors of the BNS models are largely favored over BBH. On the other hand, when $\Lambda_1 = \Lambda_2 = 100$, we find that the BBH model is better than BNS when the data is made with BNS. A better fit does not mean a better Bayes factor given by the evidence. To get rid of this effect, it is possible to fix the tidal deformability of neutron stars at zero to have exactly the same prior volume. In this case, either the Bayes factor becomes zero and one cannot be sure of the nature of the compact object or it remains negative and lower than -5 and the nature of the compact object becomes known. A very conservative limit to avoid preferring BBH when a BNS signal is injected without redoing a Bayesian analysis and fixing the deformability would be to take a limit of 8 instead of 5. This limit of 8 has been conventionally introduced in [215].

The detection of a merger at a distance larger than 250 Mpc will not have a good enough signal to noise ratio to allow the determination of the nature of compact objects even if the merger is perfectly oriented for the Hanford detector. This limit can be improved if we consider a higher chirp mass for the merger but during a real detection, the noise is never ideal and the orientation of the merger not optimal. By considering Einstein Telescope, the comparison between two models is dramatically improved. This ability to discriminate between two models can be used to interpret experimental measurements of GWs and obtain incredible insights in General Relativity.

Conclusion

Despite the great successes of cosmology, the ΛCDM model assumes the existence of dark matter which is 5 times more abundant than baryonic matter and it also assumes the existence of dark energy which dominates the current evolution of the Universe. Gravitational impacts of dark matter are not questioned, but to solve the problem of this invisible matter, there are only two possibilities: change the theory of gravity or introduce a new particle (in the broad sense) to the Standard Model. Even if dark matter remains of unknown nature, its behavior can be imited by a scalar field dominated by a quadratic potential. We have therefore presented the fuzzy dark matter model which assumes a tiny mass of the order of 10^{-22} eV. Dark energy can also be described by a scalar field dominated by a constant potential which gives an energy density that does not evolve with the scale factor. The flatter the potential, the more the model will behave like a cosmological constant. On the other hand, the energy density of the scalar field may have been different in the past even if it constant today.

In Universe described by the Friedmann-Lemaître-Robertson-Walker metric, the energy density of a scalar field introduced by the Quintessence and Fuzzy dark matter models evolves as the power of the scale factor a: $\rho_\phi = (a_0/a)^n$. This power n is between 6 for a scalar field dominated by its kinetic energy and 0 if it is dominated by a constant potential. During the whole evolution of the Universe, this power n has potentially changed. If n is equal to 3, the energy density of the scalar field evolves as dark matter and if $n = 0$, it evolves as dark energy. To unify the two unknown components of the Universe by a single scalar field called dark fluid model, it is necessary to have a transition between $n = 3$ and $n = 0$. The minimal model which realizes this condition must have a potential composed of a constant V_0 and a mass term m. Thus, going back in time the energy density of such field evolves in $n = 0$, then $n = 3$, then $n = 0$, then $n = 6$. If V_0 and m are the two key ingredients of a dark fluid model which must dominate the evolution of the scalar field at low energy, the potential can be much more complex as long as the Taylor expansion in the weak field gives the minimal model. Indeed, such a model is very little constrained in the primordial Universe because its energy density is often negligible compared to the radiation density.

To reduce the number of scalar fields in cosmology, the dark fluid model mimicks the

behavior of dark matter and dark energy by a single scalar field. In cosmology, inflation is also described by a scalar field. Thus, we have introduced a model that unifies the dark fluid model with inflation. This model must govern both the evolution of the Universe in these very first seconds, but also the current evolution of the Universe. For this, it was necessary to introduce a non-minimal coupling between gravity and the scalar field: $\phi^2 R^2$. This term is only non negligible at the very beginning of the Universe when the curve of space-time is huge. Moreover, to have a viable model, the scalar field must break spontaneously before inflation, which gives a $\alpha^2 R^2$ term and thus the R^2-inflation introduced by Starobinsky. Without this symmetry breaking the attractor point of the theory would correspond to $\phi = 0$ and it would not have been possible to have the rapid acceleration of the expansion of the Universe. Thus, it is possible to unify inflation, dark matter and dark energy with a single scalar field.

To constrain the scalar fields in the early Universe, it is possible to study their impact on the abundance of different primordial elements produced during Big-Bang nucleosynthesis. Scalar field evolving generally in power of a will modify the expansion of the Universe via the Hubble factor and thus the formation of the first nuclei. Thus, we have constrained the density of a scalar field during Big-Bang nucleosynthesis. In the particular case where the field evolves as radiation, we found the limit of 3 extra species of neutrinos. We have seen that adding a scalar field is not a solution to the lithium problem even in the case where the scalar field decays into radiation. On the other hand, the upper bound on the energy density of a scalar field during BBN has been calculated.

In a second time, we considered primordial black holes as an alternative to dark matter. This idea came back to the forefront with the detection of gravitational waves. Indeed, a significant part of dark matter could be constituted by primordial black holes around one solar mass and thus potentially detectable by the LIGO/Virgo collaboration. For the moment, no compact object has been identified as a primordial black hole. We have studied the conditions necessary to identify the nature of compact objects during a detection. An important parameter is the signal-to-noise ratio because the higher it is, the better we can deduce the posterior distribution and thus the possibility to detect the effect of baryonic matter through the tidal deformability. To characterize the difference between two templates of gravitational wave-forms, the maximization on the coalescence phase and the coalescence time of the match filtering is a powerful tool. This is used to characterize the maximum difference between two wave-forms that should be used for online detection. We have studied how a gravitational wave signal can be used to determine the nature of the source. During a detection, it is the mass of the compact object which is taken into account to conclude on its nature. If the compact object has a mass greater than 5 $M_\odot$, then it is a black hole and if it is a mass less than 2.2 $M_\odot$, then it is a neutron star. If we do not use this criterion because of primordial black holes, we need to be able to distinguish between BBH, BNS and BHNS templates. Thus, we studied the Bayes factor that allows to compare two models and defined a conservative limit of 8 to have a strong evidence. For a BBH merge of 1.44 $M_\odot$ injected in realistic detector noise, BBH template will always be favored over a BNS template, but for distances of the order of 300 Mpc this distinction is inconclusive. When a BNS merge is injected into the noise, the distinction between BBH and BNS depends strongly on the tidal deformability of the objects. For

very low deformability, the distance between the source and the detectors must be less than 100 Mpc. For higher deformabilities, the distance that allows a distinction can go up to 200 Mpc. We expect a great improvement on these limits with Einstein Telescope.

The metric describing primordial black holes, is the Kerr-Newman metric which is the same as that of usual black holes. The only difference is that the mass of primordial black holes can be as small as the Planck mass and as large as the mass of super massive black holes. In a first step, we generalized the scaling relations of General Relativity used in numerical relativity. For a BBH merger of total mass M_T, the wave-forms are computed in the natural units which are: $c = 1$, and $G = 1$ $M_T = 1$. Thus, the mass of the primordial holes does not pose a problem for the theoretical calculation of the wave-forms, but unfortunately the frequency of the signal will be rescaled and will go out of the pass bound of the detectors. The physical limits of the rescaling will be the evaporation of the black hole by Hawking radiation and a too fast extension of the Universe compared to the merger time. On the other hand, some theories beyond General Relativity are not scale invariant and studying the rescaling of gravitational wave-forms could be a first clue on the limits of exotic black holes.

The gravitational wave-forms of a BBH merger are rather well known and are crucial to determine the merge parameters. On the other hand, because of the description of the matter for a neutron star, the BNS wave-forms are much more difficult to calculate. Moreover, the behavior of matter in such conditions is not known. In particular, are there phase transitions? Is the core of neutron stars made up of quark-gluon plasma? Thus, the study of neutron star mergers could help answering such questions. Using Whysky_THC, we have shown how to obtain a wave-form of a merge BNS for a tabulated equation of state with density, temperature and electron fraction as variables, so it is necessary to do this study in a systematic way for many equations of state generated by the Meta Model.

Part III

Appendix

A

List of abbreviations and acronyms

This appendix contains the list of symbols and abbreviations used in this manuscript.

BH	Black Hole
PBH	Primordial Black Hole
NS	Neutron Star
BBH	Binary Black Hole
BNS	Binary Neutron Star
BHNS	Black Hole - Neutron Star
DM	Dark Matter
FDM	Fuzzy Dark Matter
BBN	Big-Bang Nucleosynthesis
c	Sound speed
G	Newton's constant
$\hbar$	Planck's constant
$M_\odot$	Solar mass
$g_{\mu\nu}$	Metric with the convention $(-,+,+,+)$
a	Scale factor of the Universe
$a_0 = a(t_0) = 1$	Scale factor at the reference time t_0
a_{eq}	Scale factor at matter-radiation equality
H_0	Hubble's constant
ρ_b	Baryon energy density
ρ_m	Matter energy density
ρ_r	Energy density of all radiation
ρ_Λ	Dark matter energy density
ρ_ϕ	Scalar field energy density
$\rho^c = 3H^2/8\pi G$	Critical energy density
$\Omega_X = \rho_X/\rho^c$	Energy density fraction of the species X

Y_p	Primordial helium mass fraction
^2H	Deuterium
^3He	Helium-3
^7Li	Lithium-7
m_i	Mass of the ith object
$M_T = m_1 + m_2$	Total mass of a binary system
$\mathcal{M} = (m_1 m_2)^{3/5}/(m_1 + m_2)^{1/5}$	Chirp mass
$q = m_2/m_1$	Mass ratio
d	Luminosity distance in Mpc
ra	Right ascension in radians
dec	Declination in radians
ψ	Polarization in radians
χ_i	Aligned spin of the ith object
Λ_i	Tidal deformability of the ith object

B

Cosmological scalar fields and BBN

This appendix is a summary of our main results presented in Part I. This work has been realized for the 40th International Conference on High Energy Physics [23].

Contents

The nature of dark matter and of dark energy which constitute more than 95% of the energy in the Universe remains a great and unresolved question in cosmology. Cold dark matter can be made of an ultralight scalar field dominated by its mass term which interacts only gravitationally. The cosmological constant introduced to explain the recent acceleration of the Universe expansion can be easily replaced by a scalar field dominated by its potential. More generally, scalar fields are ubiquitous in cosmology: inflaton, dilatons, moduli, quintessence, fuzzy dark matter, dark fluid, etc. are some examples. One can wonder whether all these scalar fields are independent. The dark fluid model aims at unifying quintessence and fuzzy dark matter models with a unique scalar field. One step futher is to unify the dark fluid model with inflation. In the very early Universe such scalar fields are not strongly constrained by direct observations, but Big-Bang nucleosynthesis sets constraints on scalar field models which lead to a modification on the abundance of the elements. In this talk we will present a scalar field model unifying dark matter, dark energy and inflation, and study constraints from Big-Bang nucleosynthesis on primordial scalar fields.

B.1 Introduction

Scalar fields are ubiquitous in cosmology. Fuzzy dark matter model [6] has for example been introduced to replace cold dark matter with a scalar field dominated by its mass term, and such a scalar field behaves like collisionless matter. Quintessence models [41] on the other hand replace the cosmological constant with a scalar field. The energy density of these models evolves with time and may have played a role at earlier stages of the Universe. Inflation can also be described with a scalar field.

One possibility to reduce the number of different scalar fields involved in cosmology is to unify them. In the first section, we will present the dark fluid model [49, 52] which describes both dark energy and dark matter with a single scalar field. In the second section, we will go further by introducing a scalar field to rule them all, i.e. unifying inflation and dark fluid. In the final section, we will derive constraints on scalar field scenarios from Big-Bang nucleosynthesis, since the presence of scalar fields can affect the observed abundance of the elements.

B.2 Dark Fluid model

The dark fluid model aims at unifying dark energy and dark matter with a single scalar field. To reproduce a cold dark matter behaviour, the scalar field has to oscillate quickly around the minimum of its potential. Its value at the minimum needs to be nonzero in order to create an acceleration of the expansion, as explained by the cosmological constant in the ΛCDM model. The following system of equations gives the cosmological evolution for an isotropic and homogeneous Universe described by the Robertson and Walker metric and the Klein-Gordon equation which governs the scalar field evolution:

$$\begin{aligned} H^2 &= \frac{8\pi G}{3}\left(\rho_\phi + \rho_r + \rho_m\right) , \\ 2\dot{H} + 3H^2 &= -8\pi G\left(P_\phi + P_r + P_m\right) , \\ \ddot{\phi} + 3H\dot{\phi} &+ \frac{dU}{d\phi} = 0 . \end{aligned} \tag{B.1}$$

The radiation energy density ρ_r evolves according to a^{-4} and the baryonnic matter energy density ρ_m evolves according to a^{-3} where a is the scale factor. Both energy densities are drawn in Figure B.1 and are the same as in the ΛCDM model. To determine the density of the scalar field ρ_ϕ, one needs to define the potential U, but its shape is still an open question. The simplest potential can be defined with the two parameters V_0 and m:

$$U(\phi) = V_0 + \frac{1}{2}m^2\phi^2 . \tag{B.2}$$

The constant $V_0 = \Lambda c^4/8\pi G$ leads to a dark energy behaviour with Λ the cosmological constant, and the mass term m leads to a dark matter behaviour. The value of m is approximately equal to 10^{-22} eV, which corresponds to the mass of the fuzzy dark matter model. At galactic scale, the scalar field forms Bose-Einstein condensates, which may constitute galaxy-sized dark matter halos. For a typical halo of 10 kpc, the Compton wavelength $l = h/mc$ requires such a tiny mass m. With this value, one can reproduce

the flat spiral galaxy rotation curves [9] and avoid the cuspy halo and missing satellite problems [65].

The evolution of the energy density ρ_ϕ is also drawn in Figure B.1: when the scalar field evolution is dominated by its kinetic energy, the density decreases as a^{-6}. Later the potential is no longer negligible and one can observe a plateau. When the scalar field oscillates quickly around its minimum, the energy density decays as a^{-3}, and more recently the constant V_0 leads to an accelerated expansion of the Universe. There in the dark fluid model, a single scalar field can replace both dark matter and dark energy simultaneously.

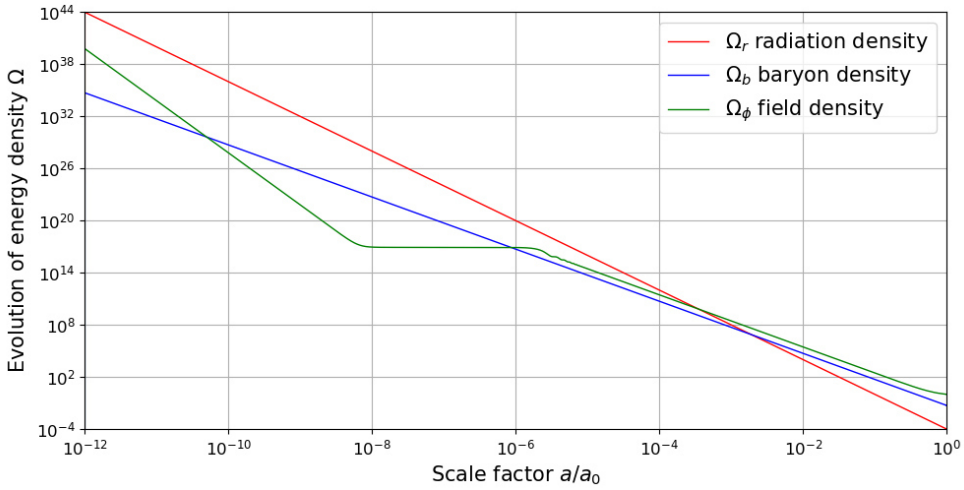

Figure B.1 – Evolution of the dark fluid scalar field density (green), radiation density (red) and baryon density (blue) fractions as functions of the scale factor.

B.3 Triple Unification

Several models of triple unification have already been studied in the literature, but these models do not explain dark matter as in the dark fluid model, i.e. with a scalar field with an ultralight mass term $m \sim 10^{-22}$ eV. In this section we present a more natural triple unification scenario by assuming a non-minimal coupling to the gravity $\phi^2 R^2$ and a symmetry breaking before inflation (see Ref. [16]). Considering a Z_2 symmetry for the scalar field and a quadratic coupling in R, the model is defined by the action:

$$\mathcal{S} = \int d^4x\sqrt{-g}\left[\frac{1}{2\tilde{\kappa}^2}\left(R + \alpha\phi^2 R + \beta\phi^2 R^2\right) - \frac{1}{2}g^{\mu\nu}\partial_\mu\phi\partial_\nu\phi - V(\phi)\right], \tag{B.3}$$

where $\tilde{\kappa}$ is a modified Einstein's constant and V the potential of the scalar field defined by:

$$V(\phi) = V_0 + \frac{m^2}{8v^2}\left(\phi^2 - v^2\right)^2. \tag{B.4}$$

For ϕ equal to zero, the potential has a local maximum, around which the theory is unstable. The two minima correspond to $\phi = \pm v$. When the scalar field goes to one of

these minima the Z_2 symmetry is spontaneously broken. By replacing ϕ by $\xi \pm v$ where ξ characterizes the variation of the scalar field around the minimum, the action (B.3) becomes:

$$\mathcal{S} = \int d^4x\sqrt{-g}\left[\frac{1}{2\kappa^2}\left(R + \frac{\beta v^2}{\alpha v^2 + 1/(1 \pm 2\xi/v + \xi^2/v^2)}R^2\right) - \frac{1}{2}g^{\mu\nu}\partial_\mu\xi\partial_\nu\xi - V(\xi)\right], \tag{B.5}$$

with:

$$\begin{aligned} \kappa &= \frac{\tilde{\kappa}}{\sqrt{1 + \alpha v^2(1 \pm 2\xi/v + \xi^2/v^2)}}, \\ V(\xi) &= V_0 + \frac{m^2}{2}\xi^2 \pm \frac{m^2}{2v}\xi^3 + \frac{m^2}{8v^2}\xi^4. \end{aligned} \tag{B.6}$$

In the $|\xi| \ll v$ limit, κ is constant and equal to the Einstein's constant. If one neglects the scalar field variation ξ, only the R and R^2 terms have an impact on the Universe evolution after the symmetry breaking. The R^2 term produces an inflationary period which will be similar to the one of Starobinsky inflation [28]:

$$\mathcal{S} = \int d^4x\sqrt{-g}\Big[\frac{1}{2\kappa^2}\left(R + \frac{\beta v^2}{(1 + \alpha v^2)M_P^2}R^2\right)\Big]. \tag{B.7}$$

As in the R^2-inflation model [74], the action (B.7) produces an inflationary period compatible with the observations and the constant $\beta v^2/(1 + \alpha v^2)$ can be fixed by the amplitude of the cosmic microwave mackground power spectrum to be 10^9 [16]. After inflation, the Unruh effect will produce the radiation energy density of the usual standard model and will also reheat the scalar field ξ.

The scalar field ξ which appears after symmetry breaking and characterizes the variation around the minimum will evolve as in the simplest dark fluid model when neglecting the higher order terms of the potential (B.6). It can therefore replace dark energy thanks to the V_0 constant term, and dark matter via the mass term. The ξ^3 and ξ^4 terms have negligible effects if $v > 7 \times 10^{26}$ eV. For example in galaxies, the density of dark matter gives an average value of 3×10^{20} eV for the scalar field ξ, so that

$$\begin{aligned} \frac{m^2\xi^3}{2v}\Big/\frac{m^2\xi^2}{2} &\simeq 5 \times 10^{-7}, \\ \frac{m^2\xi^4}{8v^2}\Big/\frac{m^2\xi^2}{2} &\simeq 5 \times 10^{-14}, \end{aligned} \tag{B.8}$$

and the higher order terms can be safety neglected. Therefore the action (B.3) unifies inflation, dark energy and dark matter by assuming a unique and single scalar field.

B.4 Big-Bang nucleosynthesis

Big-Bang nucleosynthesis is generally considered to occur during radiation domination, the total energy density is mainly composed of photons, electrons, positrons, baryons, neutrinos, antineutrinos and dark matter. For a temperature of about 1 MeV, the hydrogen nuclei can fuse into helium nuclei. The reactions which produced the primordial abundances

freeze out because of the Universe expansion. In the standard cosmological model, the observational measurements and the theoretical predictions obtained using the AlterBBN public code [84] are given in Table B.1. Helium-4, helium-3 and deuterium abundances are compatible with measurements, but there is a conflict with the lithium-7 abundance. Adding a stable scalar field to the total energy density or a decaying scalar field to radiation during Big-Bang nucleosynthesis does not solve the lithium problem. However, we will can find upper limits on the energy densities of such scalar fields in order to be compatible with helium-4, helium-3 and deuterium abundance observational measurements. There is no lower limit: without scalar field the standard model is retrieved.

elements	observational measurements	theoretical predictions
Y_p	0.245 ± 0.003	0.2472 ± 0.0006
$^2H/H$	$(2.569 \pm 0.027) \times 10^{-5}$	$(2.463 \pm 0.074) \times 10^{-5}$
$^3He/H$	$(1.1 \pm 0.2) \times 10^{-5}$	$(1.03 \pm 0.03) \times 10^{-5}$
$^7Li/H$	$(1.6 \pm 0.3) \times 10^{-10}$	$(5.4 \pm 0.7) \times 10^{-10}$

Table B.1 – Helium-4, helium-3, deuterium and lithium-7 abundances from observational measurements [85] and theorical predictions [84].

B.4.1 Constraints on stable scalar fields

We first consider the density of the scalar field to be a power law of the scale factor:

$$\rho_\phi = \rho_\phi^0(1\text{MeV}) \times a^{-n}\,, \tag{B.9}$$

which modifies the abundance of the elements via a modification of the Hubble rate, which is proportional to the total energy density. For example, as we can see in Figure B.1, the simplest dark fluid model evolves with $n = 6$ during Big-Bang nucleosynthesis. The χ^2 constraints at 95% C.L. give [17]:

$$\begin{aligned}
&\text{for } n = 6: \quad \rho_\phi\ (1\text{ MeV}) \ \leq 1.40\rho_\gamma\ (1\text{ MeV})\,,\\
&\text{for } n = 4: \quad \rho_\phi\ (1\text{ MeV}) \ \leq 0.11\rho_\gamma\ (1\text{ MeV})\,,\\
&\text{for } n = 3: \quad \rho_\phi\ (1\text{ MeV}) \ \leq 0.005\rho_\gamma\ (1\text{ MeV})\,,\\
&\text{for } n = 0: \quad \rho_\phi\ (1\text{ MeV}) \ \leq 2 \times 10^{-7}\rho_\gamma\ (1\text{ MeV})\ .
\end{aligned} \tag{B.10}$$

For $n = 4$, the limit can be reinterpreted as 3 extra species of neutrinos.

B.4.2 Constraints on decaying scalar fields

When the scalar field decays, it will no longer affect the Universe evolution because its density becomes negligible. If it decays after Big-Bang nucleosynthesis, the stable scalar field case is recovered. Therefore, one considers a scalar field which decays into radiation

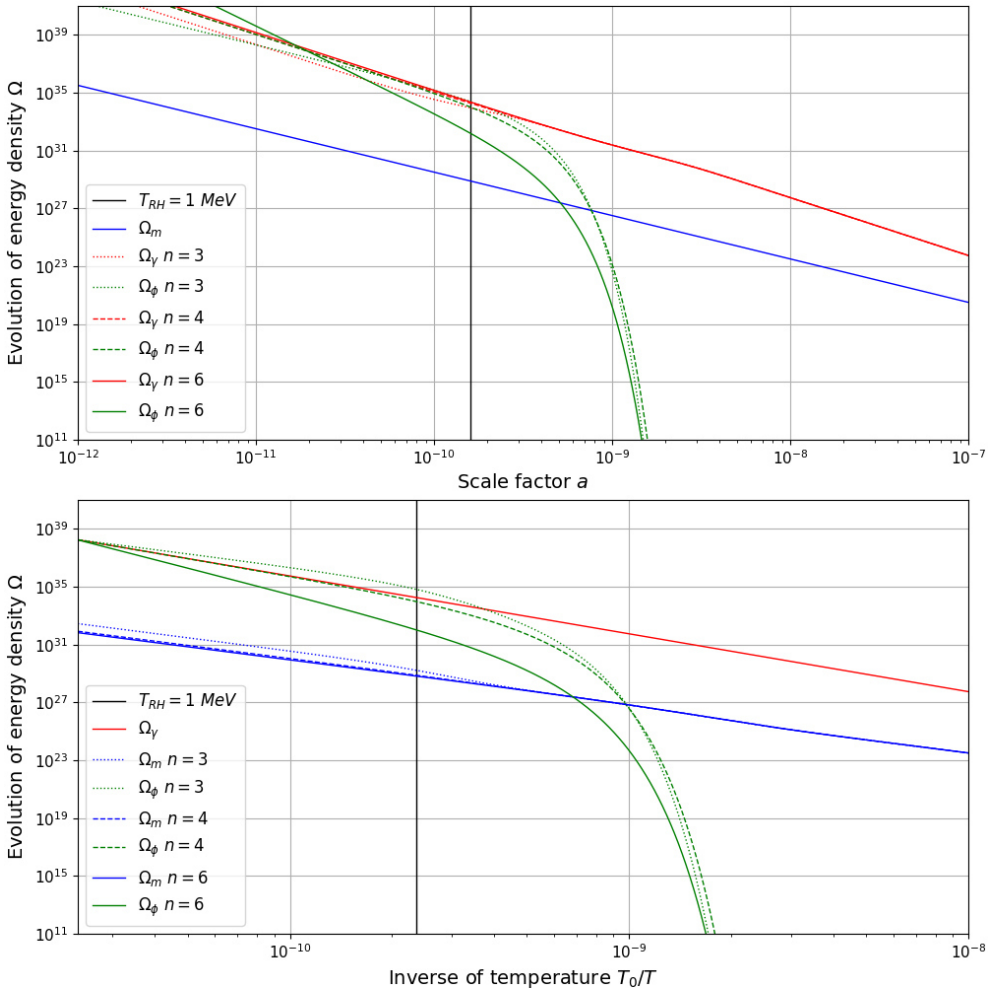

Figure B.2 – Evolution of scalar field density (green), radiation density (red) and matter density (blue) fractions as functions of the scale factor (top) and of the inverse of temperature (bottom) for different values of n. The temperature of reheating is equal to 1 MeV and is represented by the vertical black line.

during Big-Bang nucleosynthesis. The evolution of the scalar field density is given by the Klein-Gordon equation:

$$\frac{d\rho_\phi}{dt} = -nH\rho_\phi - \Gamma_\phi \rho_\phi \,, \tag{B.11}$$

in which there is an additional decaying constant $\Gamma_\phi = \sqrt{4\pi^3 g_{\text{eff}}\,(T_{RH})/45}\,T_{RH}^2/M_P$, where T_{RH} is the reheating temperature. Figure B.2 shows the evolution of the scalar field, which in absence of decay corresponds to $\rho_\phi = \rho_\phi^0 \times a^{-n}$. The initial value of the scalar field energy density is chosen at $T_i = 10$ MeV. This value has to be adjusted to recover the baryon-to-photon ratio inferred from the cosmic microwave background. Considering the evolution of the matter, radiation and scalar field densities, it is possible to make theoretical predictions

for Big-Bang nucleosynthesis. The χ^2 constraints at 95% C.L. give [17]:

$$\begin{aligned} &\text{for } n = 6: \quad \rho_\phi\ (10\ \text{MeV}) \ \leq 0.5\rho_\gamma\ (10\ \text{MeV})\,, \\ &\text{for } n = 4: \quad \rho_\phi\ (10\ \text{MeV}) \ \leq 0.1\rho_\gamma\ (10\ \text{MeV})\,, \\ &\text{for } n = 3: \quad \rho_\phi\ (10\ \text{MeV}) \ \leq 0.01 \left(\frac{T_{RH}}{1\ \text{MeV}}\right) \rho_\gamma\ (10\ \text{MeV})\ . \end{aligned} \tag{B.12}$$

For $n = 4$, this limit is equivalent to the stable scalar field because the scalar field evolves like radiation and decays into radiation.

B.5 Conclusion

To conclude, we have presented a model that unifies not only dark matter and dark energy but also inflation. Several triple unification models have already been studied so far, but we have presented here a model in which dark matter has a behaviour similar to fuzzy dark matter i.e. an ultralight matter. Furthermore we have derived the upper limit of energy densities from Big-Bang nucleosynthesis for generic stable and decaying scalar fields.

Bibliography

[1] M. Tegmark *et al.*, "The 3-D power spectrum of galaxies from the SDSS," *Astrophys. J.*, vol. 606, pp. 702–740, 2004.

[2] N. Aghanim *et al.*, "Planck 2018 results. VI. Cosmological parameters," *Astron. Astrophys.*, vol. 641, p. A6, 2020.

[3] J. D. Bekenstein, "Relativistic gravitation theory for the MOND paradigm," *Phys. Rev. D*, vol. 70, p. 083509, 2004. [Erratum: Phys.Rev.D 71, 069901 (2005)].

[4] E. Armengaud *et al.*, "Searching for low-mass dark matter particles with a massive Ge bolometer operated above-ground," *Phys. Rev. D*, vol. 99, no. 8, p. 082003, 2019.

[5] B. Carr and F. Kuhnel, "Primordial Black Holes as Dark Matter: Recent Developments," *Ann. Rev. Nucl. Part. Sci.*, vol. 70, pp. 355–394, 2020.

[6] W. Hu, R. Barkana, and A. Gruzinov, "Cold and fuzzy dark matter," *Phys. Rev. Lett.*, vol. 85, pp. 1158–1161, 2000.

[7] A. G. Riess *et al.*, "Type Ia supernova discoveries at z $>$ 1 from the Hubble Space Telescope: Evidence for past deceleration and constraints on dark energy evolution," *Astrophys. J.*, vol. 607, pp. 665–687, 2004.

[8] S. Tsujikawa, "Quintessence: A Review," *Class. Quant. Grav.*, vol. 30, p. 214003, 2013.

[9] A. Arbey, J. Lesgourgues, and P. Salati, "Galactic halos of fluid dark matter," *Phys. Rev.*, vol. D68, p. 023511, 2003.

[10] B. Abbott *et al.*, "Observation of Gravitational Waves from a Binary Black Hole Merger," *Phys. Rev. Lett.*, vol. 116, no. 6, p. 061102, 2016.

[11] J. A. R. Cembranos, A. L. Maroto, S. J. Núñez Jareño, and H. Villarrubia-Rojo, "Constraints on anharmonic corrections of Fuzzy Dark Matter," *JHEP*, vol. 08, p. 073, 2018.

[12] R. Abbott *et al.*, "GW190814: Gravitational Waves from the Coalescence of a 23 Solar Mass Black Hole with a 2.6 Solar Mass Compact Object," *Astrophys. J. Lett.*, vol. 896, no. 2, p. L44, 2020.

[13] S. Dodelson, *Modern Cosmology*. Amsterdam: Academic Press, 2003.

[14] E. W. Kolb and M. S. Turner, *The Early Universe*, vol. 69. 1990.

[15] J. A. Peacock, *Cosmological physics*. 1999.

[16] A. Arbey and J. F. Coupechoux, "Unifying dark matter, dark energy and inflation with a fuzzy dark fluid," *JCAP*, vol. 01, p. 033, 2021.

[17] A. Arbey and J. F. Coupechoux, "Cosmological scalar fields and Big-Bang nucleosynthesis," *JCAP*, vol. 1911, p. 038, 2019.

[18] F. Loffler *et al.*, "The Einstein Toolkit: A Community Computational Infrastructure for Relativistic Astrophysics," *Class. Quant. Grav.*, vol. 29, p. 115001, 2012.

[19] T. W. Baumgarte and S. L. Shapiro, *Numerical Relativity: Solving Einstein's Equations on the Computer*. Cambridge University Press, 2010.

[20] E. Gourgoulhon, "3+1 formalism and bases of numerical relativity," 3 2007.

[21] A. Arbey and J.-F. Coupechoux, "Black hole mergers, gravitational waves and scaling relations," 11 2019.

[22] J.-F. Coupechoux, A. Arbey, R. Chierici, H. Hansen, J. Margueron, and V. Sordini, "Discriminating same-mass Neutron Stars and Black Holes gravitational wave-forms," 06 2021.

[23] J. F. Coupechoux and A. Arbey, "Cosmological scalar fields and Big-Bang nucleosynthesis," *PoS*, vol. ICHEP2020, p. 589, 2021.

[24] W. Freedman *et al.*, "Final results from the Hubble Space Telescope key project to measure the Hubble constant," *Astrophys. J.*, vol. 553, pp. 47–72, 2001.

[25] E. Gourgoulhon, "Relativité générale." Lecture, Mar. 2014.

[26] D. Fixsen, E. Cheng, J. Gales, J. C. Mather, R. Shafer, and E. Wright, "The Cosmic Microwave Background spectrum from the full COBE FIRAS data set," *Astrophys. J.*, vol. 473, p. 576, 1996.

[27] Y. Akrami *et al.*, "Planck 2018 results. X. Constraints on inflation," 7 2018.

[28] A. A. Starobinsky, "A New Type of Isotropic Cosmological Models Without Singularity," *Adv. Ser. Astrophys. Cosmol.*, vol. 3, pp. 130–133, 1987.

[29] A. De Felice and S. Tsujikawa, "f(R) theories," *Living Rev. Rel.*, vol. 13, p. 3, 2010.

[30] D. Baumann, "Inflation," in *Theoretical Advanced Study Institute in Elementary Particle Physics: Physics of the Large and the Small*, 7 2009.

[31] P. Ade *et al.*, "Planck 2015 results. XX. Constraints on inflation," *Astron. Astrophys.*, vol. 594, p. A20, 2016.

[32] D. H. Lyth and A. Riotto, "Particle physics models of inflation and the cosmological density perturbation," *Phys. Rept.*, vol. 314, pp. 1–146, 1999.

[33] S. Burles, K. Nollett, and M. S. Turner, "Deuterium and big bang nucleosynthesis," *Nucl. Phys. A*, vol. 663, pp. 861c–864c, 2000.

[34] E. V. Linder and D. Huterer, "How many dark energy parameters?," *Phys. Rev.*, vol. D72, p. 043509, 2005.

[35] V. Pettorino, L. Amendola, and C. Wetterich, "How early is early dark energy?," *Phys. Rev.*, vol. D87, p. 083009, 2013.

[36] P. A. R. Ade *et al.*, "Planck 2015 results. XIV. Dark energy and modified gravity," *Astron. Astrophys.*, vol. 594, p. A14, 2016.

[37] A. Arbey, J. Lesgourgues, and P. Salati, "Quintessential haloes around galaxies," *Phys. Rev.*, vol. D64, p. 123528, 2001.

[38] A. Arbey, "The Unifying Dark Fluid Model," *AIP Conf. Proc.*, vol. 1241, pp. 700–707, 2010.

[39] G. Aad *et al.*, "Observation of a new particle in the search for the Standard Model Higgs boson with the ATLAS detector at the LHC," *Phys. Lett.*, vol. B716, pp. 1–29, 2012.

[40] S. Chatrchyan *et al.*, "Observation of a new boson at a mass of 125 GeV with the CMS experiment at the LHC," *Phys. Lett.*, vol. B716, pp. 30–61, 2012.

[41] I. Zlatev, L.-M. Wang, and P. J. Steinhardt, "Quintessence, cosmic coincidence, and the cosmological constant," *Phys. Rev. Lett.*, vol. 82, pp. 896–899, 1999.

[42] L. Amendola, "Coupled quintessence," *Phys. Rev.*, vol. D62, p. 043511, 2000.

[43] R. R. Caldwell, "A Phantom menace?," *Phys. Lett.*, vol. B545, pp. 23–29, 2002.

[44] T. Chiba, T. Okabe, and M. Yamaguchi, "Kinetically driven quintessence," *Phys. Rev.*, vol. D62, p. 023511, 2000.

[45] M. C. Bento, O. Bertolami, and A. A. Sen, "Generalized Chaplygin gas, accelerated expansion and dark energy matter unification," *Phys. Rev.*, vol. D66, p. 043507, 2002.

[46] S. Nojiri and S. D. Odintsov, "Unifying phantom inflation with late-time acceleration: Scalar phantom-non-phantom transition model and generalized holographic dark energy," *Gen. Rel. Grav.*, vol. 38, pp. 1285–1304, 2006.

[47] L. A. Boyle, R. R. Caldwell, and M. Kamionkowski, "Spintessence! New models for dark matter and dark energy," *Phys. Lett.*, vol. B545, pp. 17–22, 2002.

[48] V. Iršič, M. Viel, M. G. Haehnelt, J. S. Bolton, and G. D. Becker, "First constraints on fuzzy dark matter from Lyman-α forest data and hydrodynamical simulations," *Phys. Rev. Lett.*, vol. 119, no. 3, p. 031302, 2017.

[49] P. J. E. Peebles, "Fluid dark matter," *Astrophys. J.*, vol. 534, p. L127, 2000.

[50] N. Bilic, G. B. Tupper, and R. D. Viollier, "Unification of dark matter and dark energy: The Inhomogeneous Chaplygin gas," *Phys. Lett.*, vol. B535, pp. 17–21, 2002.

[51] A. Arbey, "Is it possible to consider dark energy and dark matter as a same and unique dark fluid?," 2005, astro-ph/0506732.

[52] A. Arbey, "Dark fluid: A Complex scalar field to unify dark energy and dark matter," *Phys. Rev.*, vol. D74, p. 043516, 2006.

[53] A. Arbey and F. Mahmoudi, "One-loop quantum corrections to cosmological scalar field potentials," *Phys. Rev.*, vol. D75, p. 063513, 2007.

[54] A. Arbey, "Cosmological constraints on unifying Dark Fluid models," *Open Astron. J.*, vol. 1, pp. 27–38, 2008.

[55] R. R. Caldwell and E. V. Linder, "The Limits of quintessence," *Phys. Rev. Lett.*, vol. 95, p. 141301, 2005.

[56] J. Magana, T. Matos, A. Suarez, and F. J. Sanchez-Salcedo, "Structure formation with scalar field dark matter: the field approach," *JCAP*, vol. 1210, p. 003, 2012.

[57] E. J. Copeland, A. R. Liddle, and D. Wands, "Exponential potentials and cosmological scaling solutions," *Phys. Rev.*, vol. D57, pp. 4686–4690, 1998.

[58] E. J. Copeland, M. Sami, and S. Tsujikawa, "Dynamics of dark energy," *Int. J. Mod. Phys.*, vol. D15, pp. 1753–1936, 2006.

[59] T. Barreiro, E. J. Copeland, and N. J. Nunes, "Quintessence arising from exponential potentials," *Phys. Rev.*, vol. D61, p. 127301, 2000.

[60] E. V. Linder, "Theory Challenges of the Accelerating Universe," *J. Phys.*, vol. A40, p. 6697, 2007.

[61] P. J. Steinhardt, L.-M. Wang, and I. Zlatev, "Cosmological tracking solutions," *Phys. Rev.*, vol. D59, p. 123504, 1999.

[62] J. A. Frieman, C. T. Hill, A. Stebbins, and I. Waga, "Cosmology with ultralight pseudo Nambu-Goldstone bosons," *Phys. Rev. Lett.*, vol. 75, pp. 2077–2080, 1995.

[63] J. A. R. Cembranos, A. L. Maroto, and S. J. Núñez Jareño, "Cosmological perturbations in coherent oscillating scalar field models," *JHEP*, vol. 03, p. 013, 2016.

[64] A. Arbey, J. Lesgourgues, and P. Salati, "Cosmological constraints on quintessential halos," *Phys. Rev.*, vol. D65, p. 083514, 2002.

[65] L. Hui, J. P. Ostriker, S. Tremaine, and E. Witten, "Ultralight scalars as cosmological dark matter," *Phys. Rev. D*, vol. 95, no. 4, p. 043541, 2017.

[66] A. Bernal and F. Siddhartha Guzman, "Scalar Field Dark Matter: Head-on interaction between two structures," *Phys. Rev. D*, vol. 74, p. 103002, 2006.

[67] D. Clowe, M. Bradac, A. H. Gonzalez, M. Markevitch, S. W. Randall, C. Jones, and D. Zaritsky, "A direct empirical proof of the existence of dark matter," *Astrophys. J. Lett.*, vol. 648, pp. L109–L113, 2006.

[68] A. D. Linde, "Inflationary theory versus ekpyrotic / cyclic scenario," in *Workshop on Conference on the Future of Theoretical Physics and Cosmology in Honor of Steven Hawking's 60th Birthday*, pp. 801–838, 5 2002.

[69] M. Bastero-Gil, R. Cerezo, and J. G. Rosa, "Inflaton dark matter from incomplete decay," *Phys. Rev. D*, vol. 93, no. 10, p. 103531, 2016.

[70] A. R. Liddle, C. Pahud, and L. Urena-Lopez, "Triple unification of inflation, dark matter, and dark energy using a single field," *Phys. Rev. D*, vol. 77, p. 121301, 2008.

[71] A. R. Liddle and L. A. Urena-Lopez, "Inflation, dark matter and dark energy in the string landscape," *Phys. Rev. Lett.*, vol. 97, p. 161301, 2006.

[72] J. De-Santiago and J. L. Cervantes-Cota, "Generalizing a Unified Model of Dark Matter, Dark Energy, and Inflation with Non Canonical Kinetic Term," *Phys. Rev. D*, vol. 83, p. 063502, 2011.

[73] T. P. Sotiriou and V. Faraoni, "f(R) Theories Of Gravity," *Rev. Mod. Phys.*, vol. 82, pp. 451–497, 2010.

[74] M. B. Mijic, M. S. Morris, and W.-M. Suen, "The R**2 Cosmology: Inflation Without a Phase Transition," *Phys. Rev. D*, vol. 34, p. 2934, 1986.

[75] V. Mukhanov and S. Winitzki, *Introduction to quantum effects in gravity*. Cambridge University Press, 6 2007.

[76] Y. Watanabe, "Rate of gravitational inflaton decay via gauge trace anomaly," *Phys. Rev. D*, vol. 83, p. 043511, 2011.

[77] D. Gorbunov and A. Panin, "Scalaron the mighty: producing dark matter and baryon asymmetry at reheating," *Phys. Lett. B*, vol. 700, pp. 157–162, 2011.

[78] D. Gorbunov and A. Tokareva, "R^2-inflation with conformal SM Higgs field," *JCAP*, vol. 12, p. 021, 2013.

[79] M. Doran and J. Jaeckel, "Loop corrections to scalar quintessence potentials," *Phys. Rev. D*, vol. 66, p. 043519, 2002.

[80] A. D. Linde, "Chaotic Inflation," *Phys. Lett. B*, vol. 129, pp. 177–181, 1983.

[81] F. L. Bezrukov and M. Shaposhnikov, "The Standard Model Higgs boson as the inflaton," *Phys. Lett.*, vol. B659, pp. 703–706, 2008.

[82] D. I. Kaiser, "Primordial spectral indices from generalized Einstein theories," *Phys. Rev. D*, vol. 52, pp. 4295–4306, 1995.

[83] A. Arbey, "AlterBBN: A program for calculating the BBN abundances of the elements in alternative cosmologies," *Comput. Phys. Commun.*, vol. 183, pp. 1822–1831, 2012.

[84] A. Arbey, J. Auffinger, K. P. Hickerson, and E. S. Jenssen, "AlterBBN v2: A public code for calculating Big-Bang nucleosynthesis constraints in alternative cosmologies," 2018.

[85] M. Tanabashi *et al.*, "Review of Particle Physics," *Phys. Rev.*, vol. D98, no. 3, p. 030001, 2018.

[86] F. Bezrukov, A. Magnin, M. Shaposhnikov, and S. Sibiryakov, "Higgs inflation: consistency and generalisations," *JHEP*, vol. 01, p. 016, 2011.

[87] B. de Carlos, J. A. Casas, F. Quevedo, and E. Roulet, "Model independent properties and cosmological implications of the dilaton and moduli sectors of 4-d strings," *Phys. Lett.*, vol. B318, pp. 447–456, 1993.

[88] M. Gasperini and G. Veneziano, "Dilaton production in string cosmology," *Phys. Rev.*, vol. D50, pp. 2519–2540, 1994.

[89] M. Dine, L. Randall, and S. D. Thomas, "Supersymmetry breaking in the early universe," *Phys. Rev. Lett.*, vol. 75, pp. 398–401, 1995.

[90] T. Banks, M. Berkooz, and P. J. Steinhardt, "The Cosmological moduli problem, supersymmetry breaking, and stability in postinflationary cosmology," *Phys. Rev.*, vol. D52, pp. 705–716, 1995.

[91] T. Moroi and T. Takahashi, "Effects of cosmological moduli fields on cosmic microwave background," *Phys. Lett.*, vol. B522, pp. 215–221, 2001. [Erratum: Phys. Lett.B539,303(2002)].

[92] S. Nakamura and M. Yamaguchi, "Gravitino production from heavy moduli decay and cosmological moduli problem revived," *Phys. Lett.*, vol. B638, pp. 389–395, 2006.

[93] G. B. Gelmini and P. Gondolo, "Neutralino with the right cold dark matter abundance in (almost) any supersymmetric model," *Phys. Rev.*, vol. D74, p. 023510, 2006.

[94] A. Arbey, J. Ellis, F. Mahmoudi, and G. Robbins, "Dark Matter Casts Light on the Early Universe," *JHEP*, vol. 10, p. 132, 2018.

[95] R. Haas, , *et al.*, "The einstein toolkit," Nov. 2020. To find out more, visit http://einsteintoolkit.org.

[96] D. Radice, L. Rezzolla, and F. Galeazzi, "High-Order Fully General-Relativistic Hydrodynamics: new Approaches and Tests," *Class. Quant. Grav.*, vol. 31, p. 075012, 2014.

[97] D. Radice, L. Rezzolla, and F. Galeazzi, "High-Order Numerical-Relativity Simulations of Binary Neutron Stars," *ASP Conf. Ser.*, vol. 498, pp. 121–126, 2015.

[98] K. Akiyama *et al.*, "First M87 Event Horizon Telescope Results. I. The Shadow of the Supermassive Black Hole," *Astrophys. J.*, vol. 875, no. 1, p. L1, 2019.

[99] B. Abbott *et al.*, "GWTC-1: A Gravitational-Wave Transient Catalog of Compact Binary Mergers Observed by LIGO and Virgo during the First and Second Observing Runs," *Phys. Rev. X*, vol. 9, no. 3, p. 031040, 2019.

[100] R. Abbott *et al.*, "GW190521: A Binary Black Hole Merger with a Total Mass of $150M_{\odot}$," *Phys. Rev. Lett.*, vol. 125, no. 10, p. 101102, 2020.

[101] S. W. HAWKING, "Black hole explosions?," *Nature*, vol. 248, 1974.

[102] R. Balbinot, A. Fabbri, S. Fagnocchi, and R. Parentani, "Hawking radiation from acoustic black holes, short distance and back-reaction effects," *Riv. Nuovo Cim.*, vol. 28, no. 3, pp. 1–55, 2005.

[103] F. Michel, J.-F. Coupechoux, and R. Parentani, "Phonon spectrum and correlations in a transonic flow of an atomic Bose gas," *Phys. Rev. D*, vol. 94, no. 8, p. 084027, 2016.

[104] J. Steinhauer, "Observation of quantum Hawking radiation and its entanglement in an analogue black hole," *Nature Phys.*, vol. 12, p. 959, 2016.

[105] B. Carr, K. Kohri, Y. Sendouda, and J. Yokoyama, "Constraints on Primordial Black Holes," 2 2020.

[106] S. Bird, I. Cholis, J. B. Muñoz, Y. Ali-Haïmoud, M. Kamionkowski, E. D. Kovetz, A. Raccanelli, and A. G. Riess, "Did LIGO detect dark matter?," *Phys. Rev. Lett.*, vol. 116, no. 20, p. 201301, 2016.

[107] M. Sasaki, T. Suyama, T. Tanaka, and S. Yokoyama, "Primordial Black Hole Scenario for the Gravitational-Wave Event GW150914," *Phys. Rev. Lett.*, vol. 117, no. 6, p. 061101, 2016. [Erratum: Phys.Rev.Lett. 121, 059901 (2018)].

[108] S. Clesse and J. García-Bellido, "The clustering of massive Primordial Black Holes as Dark Matter: measuring their mass distribution with Advanced LIGO," *Phys. Dark Univ.*, vol. 15, pp. 142–147, 2017.

[109] "Ligo scientific collaboration." `https://www.ligo.org/science/GW-Sources.php`.

[110] G. Cusin, C. Pitrou, and J.-P. Uzan, "Anisotropy of the astrophysical gravitational wave background: Analytic expression of the angular power spectrum and correlation with cosmological observations," *Phys. Rev. D*, vol. 96, no. 10, p. 103019, 2017.

[111] L. Blanchet, "Gravitational Radiation from Post-Newtonian Sources and Inspiralling Compact Binaries," *Living Rev. Rel.*, vol. 17, p. 2, 2014.

[112] M. Zilhão and F. Löffler, "An Introduction to the Einstein Toolkit," *Int. J. Mod. Phys. A*, vol. 28, p. 1340014, 2013.

[113] G. Darmois, *Les équations de la gravitation einsteinienne*. No. 25 in Mémorial des sciences mathématiques, Gauthier-Villars, 1927.

[114] A. Lichnerowicz, "L'intégration des équations de la gravitation relativiste et le problème des n corps," *J. Math. Pures Appl. (9)*, vol. 23, pp. 37–63, 1944.

[115] Y. Fourès-Bruhat, "Sur l'intégration des équations de la relativité générale," *J. Ration. Mech. Anal.*, vol. 5, pp. 951–966, 1956.

[116] R. L. Arnowitt, S. Deser, and C. W. Misner, "The Dynamics of general relativity," *Gen. Rel. Grav.*, vol. 40, pp. 1997–2027, 2008.

[117] T. Nakamura, K. Oohara, and Y. Kojima, "General Relativistic Collapse to Black Holes and Gravitational Waves from Black Holes," *Prog. Theor. Phys. Suppl.*, vol. 90, pp. 1–218, 1987.

[118] M. Shibata and T. Nakamura, "Evolution of three-dimensional gravitational waves: Harmonic slicing case," *Phys. Rev. D*, vol. 52, pp. 5428–5444, 1995.

[119] T. Goodale, G. Allen, G. Lanfermann, J. Massó, T. Radke, E. Seidel, and J. Shalf, "The Cactus framework and toolkit: Design and applications," in *Vector and Parallel Processing – VECPAR'2002, 5th International Conference, Lecture Notes in Computer Science*, (Berlin), Springer, 2003.

[120] J. D. Brown, P. Diener, O. Sarbach, E. Schnetter, and M. Tiglio, "Turduckening black holes: An Analytical and computational study," *Phys. Rev.*, vol. D79, p. 044023, 2009.

[121] "Kranc: Kranc assembles numerical code."

[122] "McLachlan, a public BSSN code."

[123] M. Ansorg, B. Brügmann, and W. Tichy, "A single-domain spectral method for black hole puncture data," *Phys. Rev. D*, vol. 70, p. 064011, 2004.

[124] J. Thornburg, "A Fast Apparent-Horizon Finder for 3-Dimensional Cartesian Grids in Numerical Relativity," *Class. Quantum Grav.*, vol. 21, pp. 743–766, 2004.

[125] B. Wardell, I. Hinder, and E. Bentivegna, "Simulation of GW150914 binary black hole merger using the Einstein Toolkit," Sept. 2016.

[126] D. Pollney, C. Reisswig, E. Schnetter, N. Dorband, and P. Diener, "High accuracy binary black hole simulations with an extended wave zone," *Phys. Rev.*, vol. D83, p. 044045, 2011.

[127] E. Schnetter, S. H. Hawley, and I. Hawke, "Evolutions in 3-D numerical relativity using fixed mesh refinement," *Class. Quant. Grav.*, vol. 21, pp. 1465–1488, 2004.

[128] O. Dreyer, B. Krishnan, D. Shoemaker, and E. Schnetter, "Introduction to isolated horizons in numerical relativity," *Phys. Rev.*, vol. D67, p. 024018, 2003.

[129] T. Goodale, G. Allen, G. Lanfermann, J. Massó, T. Radke, E. Seidel, and J. Shalf, "The Cactus framework and toolkit: Design and applications," in *Vector and Parallel Processing – VECPAR'2002, 5th International Conference, Lecture Notes in Computer Science*, (Berlin), Springer, 2003.

[130] S. Husa, I. Hinder, and C. Lechner, "Kranc: a Mathematica application to generate numerical codes for tensorial evolution equations," *Comput. Phys. Commun.*, vol. 174, pp. 983–1004, 2006.

[131] M. Thomas and E. Schnetter, "Simulation factory: Taming application configuration and workflow on high-end resources," in *Grid Computing (GRID), 2010 11th IEEE/ACM International Conference on*, pp. 369 –378, oct. 2010.

[132] S. Husa, S. Khan, M. Hannam, M. Pürrer, F. Ohme, X. Jiménez Forteza, and A. Bohé, "Frequency-domain gravitational waves from nonprecessing black-hole binaries. I. New numerical waveforms and anatomy of the signal," *Phys. Rev. D*, vol. 93, no. 4, p. 044006, 2016.

[133] S. Khan, S. Husa, M. Hannam, F. Ohme, M. Pürrer, X. Jiménez Forteza, and A. Bohé, "Frequency-domain gravitational waves from nonprecessing black-hole binaries. II. A phenomenological model for the advanced detector era," *Phys. Rev. D*, vol. 93, no. 4, p. 044007, 2016.

[134] S. Khan, K. Chatziioannou, M. Hannam, and F. Ohme, "Phenomenological model for the gravitational-wave signal from precessing binary black holes with two-spin effects," *Phys. Rev. D*, vol. 100, no. 2, p. 024059, 2019.

[135] B. P. Abbott *et al.*, "Properties of the binary neutron star merger GW170817," *Phys. Rev. X*, vol. 9, no. 1, p. 011001, 2019.

[136] E. Gourgoulhon, P. Grandclement, K. Taniguchi, J.-A. Marck, and S. Bonazzola, "Quasiequilibrium sequences of synchronized and irrotational binary neutron stars in general relativity. I. Method and tests," *Phys. Rev. D*, vol. 63, p. 064029, 2001.

[137] F. Weber, "Strangeness in neutron stars," *J. Phys. G*, vol. 27, pp. 465–474, 2001.

[138] J. M. Lattimer and F. D. Swesty, "A Generalized equation of state for hot, dense matter," *Nucl. Phys. A*, vol. 535, pp. 331–376, 1991.

[139] M. Hempel, T. Fischer, J. Schaffner-Bielich, and M. Liebendorfer, "New Equations of State in Simulations of Core-Collapse Supernovae," *Astrophys. J.*, vol. 748, p. 70, 2012.

[140] E. Gourgoulhon, "An Introduction to the theory of rotating relativistic stars," in *CompStar 2010: School and Workshop on Computational Tools for Compact Star Astrophysics*, 3 2010.

[141] L. J. Papenfort, S. D. Tootle, P. Grandclément, E. R. Most, and L. Rezzolla, "New public code for initial data of unequal-mass, spinning compact-object binaries," *Phys. Rev. D*, vol. 104, no. 2, p. 024057, 2021.

[142] J. Margueron, R. Hoffmann Casali, and F. Gulminelli, "Equation of state for dense nucleonic matter from metamodeling. I. Foundational aspects," *Phys. Rev. C*, vol. 97, no. 2, p. 025805, 2018.

[143] L. Baiotti, I. Hawke, P. J. Montero, F. Loffler, L. Rezzolla, N. Stergioulas, J. A. Font, and E. Seidel, "Three-dimensional relativistic simulations of rotating neutron star collapse to a Kerr black hole," *Phys. Rev. D*, vol. 71, p. 024035, 2005.

[144] D. Radice and L. Rezzolla, "THC: a new high-order finite-difference high-resolution shock-capturing code for special-relativistic hydrodynamics," *Astron. Astrophys.*, vol. 547, p. A26, 2012.

[145] D. Alic, C. Bona-Casas, C. Bona, L. Rezzolla, and C. Palenzuela, "Conformal and covariant formulation of the Z4 system with constraint-violation damping," *Phys. Rev. D*, vol. 85, p. 064040, 2012.

[146] D. Radice, F. Galeazzi, J. Lippuner, L. F. Roberts, C. D. Ott, and L. Rezzolla, "Dynamical Mass Ejection from Binary Neutron Star Mergers," *Mon. Not. Roy. Astron. Soc.*, vol. 460, no. 3, pp. 3255–3271, 2016.

[147] D. Radice, A. Perego, K. Hotokezaka, S. A. Fromm, S. Bernuzzi, and L. F. Roberts, "Binary Neutron Star Mergers: Mass Ejection, Electromagnetic Counterparts and Nucleosynthesis," *Astrophys. J.*, vol. 869, no. 2, p. 130, 2018.

[148] B. J. Carr, K. Kohri, Y. Sendouda, and J. Yokoyama, "New cosmological constraints on primordial black holes," *Phys. Rev.*, vol. D81, p. 104019, 2010.

[149] B. Carr, F. Kuhnel, and M. Sandstad, "Primordial Black Holes as Dark Matter," *Phys. Rev.*, vol. D94, no. 8, p. 083504, 2016.

[150] P. Amaro-Seoane *et al.*, "eLISA/NGO: Astrophysics and cosmology in the gravitational-wave millihertz regime," *GW Notes*, vol. 6, pp. 4–110, 2013.

[151] R. P. Kerr, "Gravitational field of a spinning mass as an example of algebraically special metrics," *Phys. Rev. Lett.*, vol. 11, pp. 237–238, 1963.

[152] R. H. Boyer and R. W. Lindquist, "Maximal analytic extension of the Kerr metric," *J. Math. Phys.*, vol. 8, p. 265, 1967.

[153] E. Sorkin and T. Piran, "Formation and evaporation of charged black holes," *Phys. Rev.*, vol. D63, p. 124024, 2001.

[154] E. T. Newman, R. Couch, K. Chinnapared, A. Exton, A. Prakash, and R. Torrence, "Metric of a Rotating, Charged Mass," *J. Math. Phys.*, vol. 6, pp. 918–919, 1965.

[155] S. W. Hawking, "Particle Creation by Black Holes," *Commun. Math. Phys.*, vol. 43, pp. 199–220, 1975.

[156] B. Giacomazzo, J. G. Baker, M. C. Miller, C. S. Reynolds, and J. R. van Meter, "General Relativistic Simulations of Magnetized Plasmas around Merging Supermassive Black Holes," *Astrophys. J.*, vol. 752, p. L15, 2012.

[157] B. J. Kelly, J. G. Baker, Z. B. Etienne, B. Giacomazzo, and J. Schnittman, "Prompt Electromagnetic Transients from Binary Black Hole Mergers," *Phys. Rev.*, vol. D96, no. 12, p. 123003, 2017.

[158] D. N. Page, "Particle Emission Rates from a Black Hole: Massless Particles from an Uncharged, Nonrotating Hole," *Phys. Rev.*, vol. D13, pp. 198–206, 1976.

[159] A. Arbey and J. Auffinger, "BlackHawk: A public code for calculating the Hawking evaporation spectra of any black hole distribution," *Eur. Phys. J.*, vol. C79, no. 8, p. 693, 2019.

[160] A. Arbey, J. Auffinger, and J. Silk, "Any extremal black holes are primordial," 2019.

[161] A. Arbey, J. Auffinger, and J. Silk, "Constraining primordial black hole masses with the isotropic gamma ray background," 2019.

[162] G. C. McVittie, "The mass-particle in an expanding universe," *Mon. Not. Roy. Astron. Soc.*, vol. 93, pp. 325–339, 1933.

[163] M. Morris and K. Thorne, "Wormholes in space-time and their use for interstellar travel: A tool for teaching general relativity," *Am. J. Phys.*, vol. 56, pp. 395–412, 1988.

[164] J. P. Lemos, F. S. Lobo, and S. Quinet de Oliveira, "Morris-Thorne wormholes with a cosmological constant," *Phys. Rev. D*, vol. 68, p. 064004, 2003.

[165] L. Modesto, "Semiclassical loop quantum black hole," *Int. J. Theor. Phys.*, vol. 49, pp. 1649–1683, 2010.

[166] H. A. Buchdahl, "Non-linear Lagrangians and cosmological theory," *Mon. Not. Roy. Astron. Soc.*, vol. 150, p. 1, 1970.

[167] R. Jackiw and S. Pi, "Chern-Simons modification of general relativity," *Phys. Rev. D*, vol. 68, p. 104012, 2003.

[168] S. Deser and B. Tekin, "Shortcuts to high symmetry solutions in gravitational theories," *Class. Quant. Grav.*, vol. 20, pp. 4877–4884, 2003.

[169] R. C. Myers and M. Perry, "Black Holes in Higher Dimensional Space-Times," *Annals Phys.*, vol. 172, p. 304, 1986.

[170] R. Emparan and H. S. Reall, "Black Holes in Higher Dimensions," *Living Rev. Rel.*, vol. 11, p. 6, 2008.

[171] D. Lovelock, "The Einstein tensor and its generalizations," *J. Math. Phys.*, vol. 12, pp. 498–501, 1971.

[172] D. G. Boulware and S. Deser, "String Generated Gravity Models," *Phys. Rev. Lett.*, vol. 55, p. 2656, 1985.

[173] S. Deser and A. Ryzhov, "Curvature invariants of static spherically symmetric geometries," *Class. Quant. Grav.*, vol. 22, pp. 3315–3324, 2005.

[174] C. Garraffo and G. Giribet, "The Lovelock Black Holes," *Mod. Phys. Lett. A*, vol. 23, pp. 1801–1818, 2008.

[175] W. Israel, "Event horizons in static vacuum space-times," *Phys. Rev.*, vol. 164, pp. 1776–1779, 1967.

[176] W. Israel, "Event horizons in static electrovac space-times," *Commun. Math. Phys.*, vol. 8, pp. 245–260, 1968.

[177] B. Carter, "Axisymmetric Black Hole Has Only Two Degrees of Freedom," *Phys. Rev. Lett.*, vol. 26, pp. 331–333, 1971.

[178] T. P. Sotiriou and S.-Y. Zhou, "Black hole hair in generalized scalar-tensor gravity: An explicit example," *Phys. Rev. D*, vol. 90, p. 124063, 2014.

[179] G. Antoniou, A. Bakopoulos, and P. Kanti, "Black-Hole Solutions with Scalar Hair in Einstein-Scalar-Gauss-Bonnet Theories," *Phys. Rev. D*, vol. 97, no. 8, p. 084037, 2018.

[180] G. Antoniou, A. Bakopoulos, and P. Kanti, "Evasion of No-Hair Theorems and Novel Black-Hole Solutions in Gauss-Bonnet Theories," *Phys. Rev. Lett.*, vol. 120, no. 13, p. 131102, 2018.

[181] P. Horava, "Membranes at Quantum Criticality," *JHEP*, vol. 03, p. 020, 2009.

[182] P. Horava, "Spectral Dimension of the Universe in Quantum Gravity at a Lifshitz Point," *Phys. Rev. Lett.*, vol. 102, p. 161301, 2009.

[183] A. Kehagias and K. Sfetsos, "The Black hole and FRW geometries of non-relativistic gravity," *Phys. Lett. B*, vol. 678, pp. 123–126, 2009.

[184] M.-i. Park, "The Black Hole and Cosmological Solutions in IR modified Horava Gravity," *JHEP*, vol. 09, p. 123, 2009.

[185] E. Schnetter *et al.*, "Cactus Framework: Black Holes to Gamma Ray Bursts," 2007.

[186] F. Pretorius, "Evolution of binary black hole spacetimes," *Phys. Rev. Lett.*, vol. 95, p. 121101, 2005.

[187] J. Centrella *et al.*, "Black-hole binaries, gravitational waves, and numerical relativity," *Rev. Mod. Phys.*, vol. 82, p. 3069, 2010.

[188] H. Kreiss and J. Oliger, "Methods for the Approximate Solution of Time Dependent Problems," *Global Atmospheric Research Programme*, vol. 10, 1973.

[189] N. Yunes and F. Pretorius, "Fundamental Theoretical Bias in Gravitational Wave Astrophysics and the Parameterized Post-Einsteinian Framework," *Phys. Rev. D*, vol. 80, p. 122003, 2009.

[190] B. Abbott *et al.*, "Binary Black Hole Mergers in the first Advanced LIGO Observing Run," *Phys. Rev. X*, vol. 6, no. 4, p. 041015, 2016. [Erratum: Phys.Rev.X 8, 039903 (2018)].

[191] B. P. Abbott *et al.*, "GW151226: Observation of Gravitational Waves from a 22-Solar-Mass Binary Black Hole Coalescence," *Phys. Rev. Lett.*, vol. 116, no. 24, p. 241103, 2016.

[192] N. Yunes, K. Yagi, and F. Pretorius, "Theoretical Physics Implications of the Binary Black-Hole Mergers GW150914 and GW151226," *Phys. Rev. D*, vol. 94, no. 8, p. 084002, 2016.

[193] Z. Carson and K. Yagi, "Probing Einstein-dilaton Gauss-Bonnet Gravity with the inspiral and ringdown of gravitational waves," *Phys. Rev. D*, vol. 101, no. 10, p. 104030, 2020.

[194] T. Jacobson, "Primordial black hole evolution in tensor scalar cosmology," *Phys. Rev. Lett.*, vol. 83, pp. 2699–2702, 1999.

[195] R. Abbott *et al.*, "GWTC-2: Compact Binary Coalescences Observed by LIGO and Virgo During the First Half of the Third Observing Run," 10 2020.

[196] L. Rezzolla, E. R. Most, and L. R. Weih, "Using gravitational-wave observations and quasi-universal relations to constrain the maximum mass of neutron stars," *The Astrophysical Journal*, vol. 852, p. L25, jan 2018.

[197] B. P. Abbott *et al.*, "Model comparison from LIGO–Virgo data on GW170817's binary components and consequences for the merger remnant," *Class. Quant. Grav.*, vol. 37, no. 4, p. 045006, 2020.

[198] O. Pejcha and T. A. Thompson, "The Landscape of the Neutrino Mechanism of Core-Collapse Supernovae: Neutron Star and Black Hole Mass Functions, Explosion Energies and Nickel Yields," *Astrophys. J.*, vol. 801, no. 2, p. 90, 2015.

[199] C. T. Byrnes, M. Hindmarsh, S. Young, and M. R. S. Hawkins, "Primordial black holes with an accurate QCD equation of state," *JCAP*, vol. 08, p. 041, 2018.

[200] B. Abbott *et al.*, "GW190425: Observation of a Compact Binary Coalescence with Total Mass $\sim 3.4 M_{\odot}$," *Astrophys. J. Lett.*, vol. 892, no. 1, p. L3, 2020.

[201] E. E. Flanagan and T. Hinderer, "Constraining neutron star tidal Love numbers with gravitational wave detectors," *Phys. Rev. D*, vol. 77, p. 021502, 2008.

[202] T. Hinderer, "Tidal Love numbers of neutron stars," *Astrophys. J.*, vol. 677, pp. 1216–1220, 2008.

[203] T. Hinderer, "ERRATUM: "TIDAL LOVE NUMBERS OF NEUTRON STARS" (2008, ApJ, 677, 1216)," *The Astrophysical Journal*, vol. 697, pp. 964–964, may 2009.

[204] A. Le Tiec and M. Casals, "Spinning Black Holes Fall in Love," *Phys. Rev. Lett.*, vol. 126, no. 13, p. 131102, 2021.

[205] L. Lindblom, B. J. Owen, and D. A. Brown, "Model Waveform Accuracy Standards for Gravitational Wave Data Analysis," *Phys. Rev. D*, vol. 78, p. 124020, 2008.

[206] C. Cutler and E. E. Flanagan, "Gravitational waves from merging compact binaries: How accurately can one extract the binary's parameters from the inspiral wave form?," *Phys. Rev. D*, vol. 49, pp. 2658–2697, 1994.

[207] A. Nitz *et al.*, "gwastro/pycbc: 1.18.0 release of pycbc," Feb. 2021.

[208] S. Babak, R. Balasubramanian, D. Churches, T. Cokelaer, and B. S. Sathyaprakash, "A Template bank to search for gravitational waves from inspiralling compact binaries. I. Physical models," *Class. Quant. Grav.*, vol. 23, pp. 5477–5504, 2006.

[209] E. Baird, S. Fairhurst, M. Hannam, and P. Murphy, "Degeneracy between mass and spin in black-hole-binary waveforms," *Phys. Rev. D*, vol. 87, no. 2, p. 024035, 2013.

[210] T. Dietrich, S. Bernuzzi, and W. Tichy, "Closed-form tidal approximants for binary neutron star gravitational waveforms constructed from high-resolution numerical relativity simulations," *Phys. Rev. D*, vol. 96, no. 12, p. 121501, 2017.

[211] T. Dietrich *et al.*, "Matter imprints in waveform models for neutron star binaries: Tidal and self-spin effects," *Phys. Rev. D*, vol. 99, no. 2, p. 024029, 2019.

[212] T. Dietrich, A. Samajdar, S. Khan, N. K. Johnson-McDaniel, R. Dudi, and W. Tichy, "Improving the NRTidal model for binary neutron star systems," *Phys. Rev. D*, vol. 100, no. 4, p. 044003, 2019.

[213] S. Khan, F. Ohme, K. Chatziioannou, and M. Hannam, "Including higher order multipoles in gravitational-wave models for precessing binary black holes," *Phys. Rev. D*, vol. 101, no. 2, p. 024056, 2020.

[214] J. E. Thompson, E. Fauchon-Jones, S. Khan, E. Nitoglia, F. Pannarale, T. Dietrich, and M. Hannam, "Modeling the gravitational wave signature of neutron star black hole coalescences," *Phys. Rev. D*, vol. 101, no. 12, p. 124059, 2020.

[215] E. Thrane and C. Talbot, "An introduction to Bayesian inference in gravitational-wave astronomy: parameter estimation, model selection, and hierarchical models," *Publ. Astron. Soc. Austral.*, vol. 36, p. e010, 2019.

[216] J. H., *Theory of Probability*. USA: Oxford University Press, 1961.

[217] D. J. C. MacKay, *Information Theory, Inference and Learning Algorithms*. USA: Cambridge University Press, 2002.

[218] G. Ashton *et al.*, "BILBY: A user-friendly Bayesian inference library for gravitational-wave astronomy," *Astrophys. J. Suppl.*, vol. 241, no. 2, p. 27, 2019.

[219] I. Romero-Shaw *et al.*, "Bayesian inference for compact binary coalescences with BILBY: Validation and application to the first LIGO–Virgo gravitational-wave transient catalogue," 6 2020.

[220] R. J. E. Smith, G. Ashton, A. Vajpeyi, and C. Talbot, "Massively parallel Bayesian inference for transient gravitational-wave astronomy," *Mon. Not. Roy. Astron. Soc.*, vol. 498, no. 3, pp. 4492–4502, 2020.

[221] J. Skilling, "Nested sampling for general Bayesian computation," *Bayesian Analysis*, vol. 1, no. 4, pp. 833–859, 2006.

[222] B. P. Abbott *et al.*, "A guide to LIGO–Virgo detector noise and extraction of transient gravitational-wave signals," *Class. Quant. Grav.*, vol. 37, no. 5, p. 055002, 2020.

[223] S. Kroker and R. Nawrodt, "The Einstein telescope," *IEEE Instrum. Measur. Mag.*, vol. 18, no. 3, pp. 4–8, 2015.

[224] S. Hild, S. Chelkowski, and A. Freise, "Pushing towards the ET sensitivity using 'conventional' technology," 10 2008.